

博士論文

**Design and development of polyaniline-based multifunctional
structural composite materials**

(ポリアニリン系多機能構造用複合材料の設計と開発)

ダース スカンタ

(Das Sukanta)



東京大学
THE UNIVERSITY OF TOKYO

© Copyright 2020 by Sukanta Das

This thesis dedicated to my son, Master Sriyansh...

Abstract

Multifunctional high-performance, lightweight structural composites are the requirement for aircraft structures to protect them from electromagnetic interference and lightning strike. However, the conventional composite structures have poor performance against these severe threats, which is of concern for the safety of aircraft. Hence, in this research, the novel conductive polymer system has been used to design and develop a high-performance multifunctional lightweight structural composite. This work explores the multi-functionality of structural composite based on novel conductive polymer system, (i.e., polyaniline (PANI), dodecylbenzene sulfonic acid (DBSA), and divinylbenzene (DVB)) using suitable fabrication process.

Emeraldine base form of PANI was doped with DBSA and dispersed in the cross-linking polymer, DVB, to prepare the novel structural conductive polymer system. The developed PANI-based polymer composite is investigated and designed for the multi-functional applications, such as, strain sensing, electromagnetic interference (EMI) shielding, and lightning strike protection, which are the three main pillar of this thesis. A comprehensive study was performed to investigate strain sensing ability of the material, by evaluating following parameters, like (i) sensitivity (ii) working range (iii) hysteresis error, (iv) creep error (v) strain rate change effect (vi) reliability and (vii) thermal stability. It was concluded that the material was able to exhibit a linear relationship between the applied strain and the resistance due to piezoresistive behavior. Different studies also confirmed the reversibility, recoverability and reliability of the sensing performance. Moreover, its application, both as impregnated glass fiber reinforced conductive polymer composites and the conductive layer on glass fiber reinforced polymer composites, were verified. The results show the promising opportunities to use these composite materials as a structural self-sensing strain sensor.

For electromagnetic interference shielding investigation (i) shielding effectiveness (SE), (ii) shielding mechanism, (iii) shield thickness effect, (iv) conductivity effect, (v) permeability and permittivity effects on shielding mechanism are studied for X-band (8.2 – 12.4 GHz) frequency. It is summarized from both theoretical and experimental results that the shielding mechanism of the conductive layer dominated by absorption followed by reflection loss. Both complex permeability and permittivity of the material were estimated using the NRW algorithm. It is found the SE by absorption is almost constant for all thickness; however, its magnitude changes with thickness and conductivity value. This is because the electromagnetic

attenuation constant is almost independent of frequency. The tunability of the electrical conductivity of polyaniline composite can be used to design EMI shielding performance according to the requirement. The highest EMI shielding up to ~ 20 dB in X-band with a conductivity value of 95 S/m and thickness of 1.0 mm is reported in this work. Furthermore, the bonded conductive layer on GFRP and CFRP composites showed maximum EMI SE of ~ 17.5 dB and ~ 45 dB with a shield thickness and conductivity of 1 mm and ~ 90 S/m, respectively.

For lightning strike protection, the optimized thickness of the novel conductive polymer system layer was studied. Both CFRP and GFRP composites with the bonded conductive layer were tested with a peak current of - 40 kA. However, GFRP composites are further subjected to - 60 kA, and - 100 kA of peak current. High-speed cameras and ultrasonic tests were used for damage analysis for both FRPs and the conductive layer. It can be summarized from results that a minimum conductive layer thickness of 0.4 mm with 50 S/m of conductivity may be able to protect the composites from the lightning current of -40 kA, with a residual strength of 90%.

This doctoral thesis includes the design and development of polyaniline-based multifunctional structural composite material for aircraft application and demonstrating at least its three functionalities (i) strain sensing (ii) electromagnetic interference shielding, (iii) lightning strike protection. The presented research opens up new opportunities and provides a foundation to further improve the performance and functionalities of the composites without changing their material constitutions. A thin layer of a polyaniline-based conductive layer on composites could improve efficiency by protecting from the EMI noise, lightning strike and also could act as a structural strain sensor.

Acknowledgment

Three years back, when I move out of India, I was curious, anxious, and worried about the new country, culture, and, of course, the academic system. Japan, one of those few developed countries, which having uniqueness in everywhere, from food to educational policy. I feel lucky that I experienced lots of unique things in the last three years. It is pretty amazing to recall all those fantastic people who directly or indirectly helped me, shaped me, inspire me to follow my passion. I never thought of that; one day, my passion will push me off to write a thesis to fulfill the requirement of the Ph.D. degree in Aeronautics and Astronautics at UTokyo. The first acknowledgment is to both Japan International Cooperation Agency (JICA) and UTokyo for sponsoring and granting the Ph.D. admission, respectively. My supervisor, Professor (Associate) Tomohiro Yokozeki, an inspiration, kind and supportive person I ever come across. Thank you for accepting me as a Ph.D. student and for giving me a platform to explore and learn the research activity. Special thanks to Mrs. Miki Matsuo for her all administrative supports both in JICA and UTokyo. Dr. Vipin Kumar, my mentor, cum well-wisher. Thank you for all your early alarms and for helping me with an initial boost. I would like to thank Professor Takahira Aoki for all his valuable feedback during the review meetings. I am thankful to all lab members for their support throughout the course. Special thanks to our small and pro-active PANI group, Dr. Santwana, Sanshiro, Vince, and An. Thank you all for all your supports, feedbacks, and discussion. My extended gratitude to Dr. Sanjay R. Dhakate and Dr. Sushant Sarma from NPL, Delhi, for their support to conduct the EMI Shielding tests, Professor (Associate) Mira Mitra for her help to do vibration testing at IIT Kharagpur. Dr. Akshin, a long night partner at the office, thank for all your support and positive waves during the ups and down phase.

My family, my beloved maa, and bapi for your unconditional love and long video calls. Thank you for being my side when I spend long nights at the office. My brother and sister, thank you for your supports. Last but not least, my loveable wife, Tina, and beautiful angel, my little Krish. In the last few years, you both sacrifices a lot. However, thank you for your love and affection and for helping me to finish my work. Thank you once again, all of you.

Contents

List of Figures.....	x
List of Tables	xiv
Nomenclature.....	xv
Chapter 1	1
<i>Introduction</i>	<i>1</i>
1.1 <i>Motivation</i>	<i>1</i>
1.2 <i>Objective of the Thesis.....</i>	<i>3</i>
1.3 <i>Background.....</i>	<i>4</i>
1.3.1 Composite Materials.....	4
1.3.2 Multifunctional Composites	5
1.3.3 Conductive Nanofillers Polymers.....	6
1.3.4 Intrinsic Conductive Polymers	6
1.3.5 Novel Polyaniline-based Conductive Polymer System.....	7
1.3.5.1 Polyaniline.....	7
1.3.5.2 Dodecylbenzene-Sulfonic Acid	8
1.3.5.3 Divinylbenzene.....	8
1.3.5.4 PANI-DBSA-DVB (PDD) System.....	9
1.3.6 Electrical Resistance Measurement Techniques.....	10
1.3.6.1 Two-wire Methods.....	10
1.3.6.2 Four-wire Methods	11
1.3.7 Literature Review.....	11
1.4 <i>Overview of Thesis</i>	<i>15</i>
Chapter 2	16
<i>Structural Strain Sensor</i>	<i>16</i>
2.1 <i>Introduction</i>	<i>16</i>
2.2 <i>Sample Preparation</i>	<i>17</i>
2.2.1 PDD System.....	17
2.2.2 Glass Fiber Reinforced Conductive Polymer (GFRCP) Composites	18
2.2.3 PDD Conductive Layer on GFRP Composites	18

2.3	<i>Characterization</i>	19
2.4	<i>Results and Discussion</i>	21
2.4.1	PDD system	21
2.4.2	Glass Fiber Reinforced Conductive Polymer (GFRCP) Composites	32
2.4.3	PDD Conductive Layer on GFRP Composites	42
2.5	<i>Summary</i>	45
Chapter 3	47
	<i>Electromagnetic Interference Shielding</i>	47
3.1	<i>Introduction</i>	47
3.2	<i>EMI Shielding Theory</i>	48
3.2.1	EMI Shielding Mechanisms	48
3.2.2	Shielding Effectiveness	49
3.3	<i>Sample Preparation</i>	51
3.3.1	Preparation of Conductive Layer	51
3.4	<i>Characterizations</i>	51
3.5	<i>Results and Discussions</i>	52
3.5.1	Effect of Shielding Components.....	52
3.5.2	Effect of Multiple-Reflections and Skin Depth.....	55
3.5.3	Effect of Permittivity, Permeability, and Dielectric Loss.....	56
3.5.4	Experimental vs. Theoretical Results	57
3.5.5	Composites with Conductive Layer.....	60
3.6	Design Analysis	61
3.7	<i>Summary</i>	61
Chapter 4	63
	<i>Lightning Strike Protection</i>	63
4.1	<i>Introduction</i>	63
4.1.1	Background of LSP	63
4.1.1.1	LSP Principal	63
4.1.1.2	LSP Regulation and Standards.....	64
4.2	<i>Sample Preparation</i>	65
4.2.1	CFRP Composites with PDD layer	65
4.2.2	GFRP Composites with PDD layer	66
4.3	<i>Experimental</i>	66

4.3.1	Simulated Lightning Current Test	66
4.3.2	Residual Strength Test	69
4.4	<i>Result and Discussion</i>	69
4.4.1	CFRP Composites with PDD layers.....	69
4.4.1.1	Lightning Damage Assessment with Visual Inspections.....	69
4.4.1.2	Lightning Damage Assessment with Ultrasonic Test	72
4.4.1.3	Qualitative Damage Analysis Using Image Processing	73
4.4.1.4	Damage Analysis with Microscope	73
4.4.1.5	Residual Strength Analysis	74
4.5	<i>GFRP Composites with PDD layers</i>	75
4.5.1.1	Lightning Strike Mechanism for Insulating GFRP Structures.....	75
4.5.1.2	Lightning Damage Assessment with Visual Inspect	75
4.5.1.3	Lightning Damage Assessment with Ultrasonic Test	78
4.5.1.4	Damage Analysis with Microscope	79
4.6	<i>Design Analysis</i>	80
4.7	<i>Summary</i>	81
Chapter 5	82
<i>Conclusion</i>	82
5.1	<i>Impact</i>	83
5.1.1	Aircraft	83
5.1.2	Electric Car	83
5.1.3	Wind Turbine	83
5.2	<i>Future Scope</i>	84
Reference	85
Appendix A: MATLAB Code for NRW algorithm	97

List of Figures

FIGURE 1: KLM BOEING 777-300 BEING STRUCK BY LIGHTNING, FILMED BY RALPH VALKENIER OF KLM APRON SERVICES. [7]	2
FIGURE 2: LIGHTNING DAMAGES OF THE AIRCRAFT COMPONENTS. LEFT TO RIGHT: BOND JUMPER, ANTENNA, AND RUDDER. [8]	2
FIGURE 3: SHM IMPACT DAMAGE DETECTION SYSTEM SENSOR NETWORK INSTALLED IN THE A350 XWB CFRP COMPOSITE PANEL. [9]	2
FIGURE 4: ADVANCED CFRP COMPOSITES USED IN BOEING 787 DREAMLINER.[12]	4
FIGURE 5: TWO PRINCIPAL TYPES OF LAMINAE. [10].....	5
FIGURE 6: COMMON NANOFILLER CONDUCTIVE POLYMER SYSTEM.	6
FIGURE 7: CHEMICAL STRUCTURE OF PANI.....	7
FIGURE 8: SCHEMATIC DIAGRAM OF THE PANI CONDUCTIVE MECHANISM.	8
FIGURE 9 : CHEMICAL STRUCTURE OF DODECYLBENZENESULFONIC ACID.....	8
FIGURE 10: CHEMICAL STRUCTURE OF DIVINYLBENZENE	9
FIGURE 11: FABRICATION PROCESS OF POLYANILINE BASED NOVEL POLYANILINE-BASED CONDUCTIVE POLYMER SYSTEM.....	10
FIGURE 12: SPECIMEN CONFIGURATION FOR TWO-PROBE RESISTANCE MEASUREMENT TECHNIQUE.....	10
FIGURE 13: SPECIMEN CONFIGURATION FOR FOUR-PROBE RESISTANCE MEASUREMENT TECHNIQUE.....	11
FIGURE 14: DOG-BONE SAMPLES AND THEIR DIMENSIONS MADE WITH THE PDD SYSTEM.	18
FIGURE 15: RECTANGULAR GFRCP COMPOSITE COUPON WITH ATTACHED STRAIN GAUGE AND ELECTRODES.	18
FIGURE 16: GFRP COMPOSITE WITH PDD LAYER ON IT.	19
FIGURE 17: EXPERIMENT SETUP OF THE IN-SITU RESISTANCE CHANGE MONITORING TEST.	20
FIGURE 18: RELATIVE RESISTANCE CHANGE PLOTTED AGAINST THE APPLIED STRAIN OF THE MULTIFUNCTIONAL PANI-BASED THERMOSET POLYMER. A LINEAR FIT LINE IS USED TO ESTIMATE THE GAUGE FACTOR OF THE SENSOR.	23
FIGURE 19:RESISTANCE SENSITIVITY $\Delta R/R_0$ RESPONSE AT DIFFERENT ELEONGATION LEVELS [HIGH STRAIN] PLOTTED FOR TIME. THE LINEAR BEHAVIOR OF THE RESISTANCE SENSITIVITY RESPONSE CHANGES TO NONLINEARITY AS ELONGATION LEVEL INCREASES AFTER 0.4 MM ELONGATION. FINALLY, THE SAMPLE FAILED AT 1MM ELONGATION.	24
FIGURE 20:RESISTANCE SENSITIVITY $\Delta R/R_0$ RESPONSE AT DIFFERENT ELONGATION LEVELS [LOW STRAIN] PLOTTED FOR TIME. THE LINEAR BEHAVIOR OF THE RESISTANCE SENSITIVITY RESPONSE CHANGES TO NONLINEARITY AS ELONGATION LEVEL DECREASES TO 0.03 MM ELONGATION.	24
FIGURE 21: SENSOR RESPONSE WHEN STRAIN INCREASES AND DECREASES STEPWISE AFTER EACH CYCLE. (A) THE SENSOR WAS LOADED FROM 50 N TO 200 N (B) LOAD WAS DECREASED FROM 200 N TO 50 N	25
FIGURE 22: RESPONSE OF THE SENSOR HELD AT 0.2 % STRAIN FOR 120 SECONDS. THE STRAIN RATE IS 1 MM/MIN, AND THE CREEP ERROR CALCULATED IS 0.007%.	26
FIGURE 23: RESPONSE OF THE SENSOR WHEN IT HOLDS FOR 120 SEC AT A GIVEN STRAIN, AND THE STRAIN RATE IS 0.1 MM/MIN.	26
FIGURE 24: SENSOR RESPONSE AT DIFFERENT STRAIN RATES (1, 0.7, 0.4, 0.1 MM/MIN).	27
FIGURE 25: HYSTERESIS EFFECTS OF THE SENSOR WITHIN THE WORKING RANGE, I.E., 0.22% STRAIN AND LOADED AT A STRAIN RATE OF 1 MM/MIN.	27

FIGURE 26: HYSTERESIS EFFECTS OF THE SENSOR WITHIN THE WORKING RANGE, I.E., 0.22% STRAIN AND LOADED AT A STRAIN RATE OF 0.1 MM/MIN.	28
FIGURE 27: HYSTERESIS EFFECTS OF THE SENSOR OUTSIDE THE WORKING RANGE, I.E., 0.42% STRAIN AND LOADED AT A STRAIN RATE OF 1 MM/MIN.	28
FIGURE 28: HYSTERESIS EFFECTS OF THE SENSOR OUTSIDE THE WORKING RANGE, I.E., 0.42% STRAIN AND LOADED AT A STRAIN RATE OF 0.1 MM/MIN.	29
FIGURE 29: TEMPERATURE DEPENDENCE OF THE DC ELECTRICAL CONDUCTIVITY BETWEEN 18 AND 70 °C.	30
FIGURE 30: CYCLIC LOAD STABILITY TEST RESULTS OF THE SENSOR SUBJECTED TO 500 CYCLES AT A FREQUENCY OF 1 HZ UP TO A STRAIN VALUE OF 0.22 %. THE ABOVE PLOT REPRESENTS THE FIRST AND LAST TEN CYCLES OF THE TEST.	31
FIGURE 31: CYCLIC LOAD STABILITY TEST RESULTS OF THE SENSOR SUBJECTED TO 500 CYCLES AT A FREQUENCY OF 1 HZ UP TO A STRAIN VALUE OF 0.22%.	31
FIGURE 32: RESPONSE OF NORMALIZED RESISTANCE CHANGE TO STRAIN UNDER MONOTONIC TENSILE TEST.....	33
FIGURE 33: STRAIN MONITORING OF GFRCP COMPOSITE UNDER CONSTANT AMPLITUDE CYCLIC TENSILE LOADING. (A) NRC, STRAIN VS TIME FOR 0.07 % STRAIN, (B) NRC, STRAIN VS TIME FOR 0.13 % STRAIN, (C) NRC, STRAIN VS TIME FOR 0.19 % STRAIN, (D) NRC, STRAIN VS TIME FOR 0.25 % STRAIN.	35
FIGURE 34: THE CREEP RESPONSE CURVE OF GFRCP COMPOSITE AT ROOM TEMPERATURE, WHICH INCLUDES THE STRAIN AND NORMALIZED RESISTANCE CHANGE.....	36
FIGURE 35: NORMALIZED ELECTRICAL RESISTANCE CHANGE AND TEMPERATURE WITH TIME PLOTTED WHEN SPECIMENS WERE HEATED AT A RATE OF 10 °C /MIN FORM 30 °C TO 70 °C AND COOLED BACK TO ITS INITIAL TEMPERATURE.	37
FIGURE 36: NORMALIZED RESISTANCE CHANGE W.R.T. TEMPERATURE CHANGE PLOTTED TO EVALUATE THE TEMPERATURE COEFFICIENT OF RESISTANCE OF GFRCP COMPOSITE.....	38
FIGURE 37: STRAIN VERSUS NRC OF GFRCP COMPOSITE UNDER CONSTANT AMPLITUDE (0.13 % STRAIN) CYCLIC TENSILE LOADING. A SINGLE CYCLE REPRESENTS TO EVALUATE THE HYSTERESIS (%).	39
FIGURE 38: STRESS, STRAIN, AND NRC MONITORING OF GFRCP COMPOSITE UNDER CONSTANT AMPLITUDE (0.13 % STRAIN) CYCLIC TENSILE LOADING.	40
FIGURE 39: STRESS, STRAIN, AND NORMALIZED RESISTANCE CHANGE RESPONSE OF THE GFRCP COMPOSITE UNDER INCREMENTAL AMPLITUDE CYCLIC TENSILE LOADING. THE LOAD RANGES FROM 200 N TO 1000 N INCREMENTED BY 200 N AFTER EACH CYCLE.....	41
FIGURE 40: STRESS, STRAIN, AND NORMALIZED RESISTANCE CHANGE RESPONSE OF THE GFRCP COMPOSITE UNDER DECREMENTAL AMPLITUDE CYCLIC TENSILE LOADING. THE LOAD RANGES FROM 1000 N TO 200 N DECREMENTED BY 200 N AFTER EACH CYCLE.....	41
FIGURE 41: COMPARISON PLOT TO ANALYZE THE RESIDUAL RESISTANCE BOTH IN INCREMENTAL AND DECREMENTAL AMPLITUDE CYCLIC TENSILE LOADING.	42
FIGURE 42: PIEZORESISTIVE RESPONSE OF THE SENSOR WITHIN THE WORKING RANGE UNDER MONOTONIC TENSILE LOADING. A LINEAR FIT LINE USED TO ESTIMATE THE GAUGE FACTOR OF THE SENSOR, I.E., 0.81.	43
FIGURE 43: INCREASING STRAIN STUDY: PDD LAYER ON GFRP COMPOSITE SUBJECTED TO LOAD SWEEP FROM 0 TO 1000 N BY INCREMENTS OF 200N. (A) STRESS (B) STRAIN (C) RESISTANCE SENSITIVITY	43

FIGURE 44: DECREASING STRAIN STUDY: PDD LAYER ON GFRP COMPOSITE SUBJECTED TO LOAD SWEEP FROM 1000 N BY INCREMENTS OF 200N. (A) STRESS (B) STRAIN (C) RESISTANCE SENSITIVITY	44
FIGURE 45: PDD SENSOR RESPONSE UNDER CREEP/STRESS RELAXATION STUDY. THE SPECIMEN WAS ELONGATED TO 0.1 % STRAIN AT A RATE OF 1 MM/MIN THEN HOLD 120 SEC. THIS STUDY WAS DONE FOR THREE CYCLES.	45
FIGURE 46: SINGLE CYCLE REPRESENTATION OF CREEP/RELAXATION STUDY.	45
FIGURE 47: SCHEMATIC REPRESENT DIFFERENT SHIELDING MECHANISMS.	49
FIGURE 48: STEPS INVOLVED TO IMPLEMENT A CONDUCTIVE LAYER ON FRPs	51
FIGURE 49: TOTAL EMI ($SE_{Total\ dB} = SER + SEA$) SHIELDING OF DIFFERENT THICKNESS POLYANILINE BASED CONDUCTIVE LAYER IN THE FREQUENCY RANGE 8.2–12.4 GHz (X-BAND).	53
FIGURE 50: EMI SHIELDING BY ABSORPTION (SEA) OF DIFFERENT THICKNESS POLYANILINE BASED CONDUCTIVE LAYER IN THE FREQUENCY RANGE 8.2–12.4 GHz (X-BAND).	54
FIGURE 51: EMI SHIELDING BY ABSORPTION (SER) OF DIFFERENT THICKNESS POLYANILINE BASED CONDUCTIVE LAYER IN THE FREQUENCY RANGE 8.2–12.4 GHz (X-BAND).	54
FIGURE 52: VARIATION IN SKIN DEPTH FOR DIFFERENT THICKNESS OF POLYANILINE BASED CONDUCTIVE LAYER IN THE FREQUENCY RANGE 8.2–12.4 GHz (X-BAND).	56
FIGURE 53: COMPLEX PERMEABILITY ($\mu = \mu' + j\mu''$) AND PERMITTIVITY ($\epsilon = \epsilon' + j\epsilon''$) OF DIFFERENT THICKNESS OF POLYANILINE BASED CONDUCTIVE LAYER IN THE FREQUENCY RANGE 8.2–12.4 GHz (X-BAND). VARIATION OF OVER FREQUENCY CHANGE (A) REAL PART OF PERMEABILITY (B) (A) IMAGINARY PART OF PERMEABILITY (A) REAL PART OF PERMITTIVITY (B) (A) IMAGINARY PART OF PERMITTIVITY.....	57
FIGURE 54: COLE-COLE PLOT (IMAGINARY VS. REAL PART OF COMPLEX PERMITTIVITY) OF DIFFERENT THICKNESS OF POLYANILINE BASED CONDUCTIVE LAYER IN THE FREQUENCY RANGE 8.2–12.4 GHz (X-BAND).	58
FIGURE 55: EXPERIMENTAL AND THEORETICAL EMI SE COMPARISON FOR 1 MM, 0.8 MM, AND 0.6 MM THICK SAMPLES, CONSIDERING DC CONDUCTIVITY.....	59
FIGURE 56: EXPERIMENTAL AND THEORETICAL EMI SE COMPARISON FOR 1 MM, 0.8 MM, AND 0.6 MM THICK SAMPLES, CONSIDERING FREQUENCY-DEPENDENT CONDUCTIVITY.	59
FIGURE 57: TOTAL EMI SHIELDING OF GFRP COMPOSITE WITH DIFFERENT THICKNESS OF POLYANILINE BASED CONDUCTIVE LAYER IN THE FREQUENCY RANGE 8.2–12.4 GHz (X-BAND).	60
FIGURE 58: TOTAL EMI SHIELDING OF CFRP COMPOSITE WITH DIFFERENT THICKNESS OF POLYANILINE BASED CONDUCTIVE LAYER IN THE FREQUENCY RANGE 8.2–12.4 GHz (X-BAND).	61
FIGURE 59: LIGHTNING WAVEFORM DEFINED BY SAE ARP-5412B [118]	64
FIGURE 60: DIFFERENT LIGHTNING ZONES OF AN AIRCRAFT [116]	65
FIGURE 61: SIMULATED LIGHTNING STRIKE TEST SETUP.	67
FIGURE 62: CLOSER VIEW OF SAMPLE WITH FIXTURE WITH DISCHARGE PLOVE.	67
FIGURE 63: DETAILS OF THE LIGHTNING CURRENT WAVE FORM FOR CFRP COMPOSITES.	68
FIGURE 64: DETAILS OF THE LIGHTNING CURRENT WAVE FORM FOR GFRP COMPOSITES.....	68
FIGURE 65: TOP VIEW PHOTOGRAPHS OF LIGHTNING DAMAGES IN CFRP COMPOSITES WITH PDD LAYER (A) 0.24 MM THICKNESS (B) 0.41 MM THICKNESS	70

FIGURE 66: DIFFERENT FAILURE DAMAGES LIKE CARBON FIBER (CF) BRAKEAGE, RESIN EVAPORATION IN CFRP COMPOSITE WITH 0.24MM THICK PDD LAYER.	70
FIGURE 67: COMPARISON OF CURRENT FLOW PROGRESS IN CFRP COMPOSITES WITH PDD LAYER (A) 0.41 MM THICKNESS [1 ST ROW] (B) 0.24 MM THICKNESS [2 ND ROW] AT DIFFERENT TIME STEPS RECORDED BY HIGH SPEED CAMERA.	71
FIGURE 68: FAILURE MECHANISM ANALYSIS OF 0.24 MM THICK PDD LAYER ON CFRP COMPOSITE.	71
FIGURE 69: FAILURE MECHANISM ANALYSIS OF 0.41 MM THICK PDD LAYER ON CFRP COMPOSITE.	72
FIGURE 70: ULTRASONIC RESULTS TO ASSES INSIDE DAMAGES OF CFRP COMPOSITES WITH (A) 0.24 MM AND (B) 0.41 MM THICK PDD LAYER.	72
FIGURE 71: QUALITATIVE DAMAGE EVALUATION OF CFRP COMPOSITES WITH (A) 0.24 MM AND (B) 0.41 MM THICK PDD LAYER. .	73
FIGURE 72 : CROSS SECTION OBSERVATION OF CFRP COMPOSITES UNDER OPTICAL MICROSCOPE, (A) AT THE LIGHTNING POINT, (B) 3 CM FAR AWAY FROM THE LIGHTNING POINT, (C) BEFORE LIGHTNING TEST.	74
FIGURE 73: LIGHTNING TESTED GFRP SAMPLES WITH PDD LAYER (A) THICKNESS OF 0.6 MM AND -40KA PEAK CURRENT, (B) THICKNESS OF 0.4 MM AND -40KA PEAK CURRENT, (C) THICKNESS OF 0.6 MM AND -60KA PEAK CURRENT, (D) THICKNESS OF 0.4 MM AND -100KA PEAK CURRENT.	77

List of Tables

TABLE 1: POLYMER-BASED CONDUCTIVE COMPOSITES: MECHANICAL AND PIEZORESISTIVE PROPERTIES.....	22
TABLE 2: ELECTRICAL AND MECHANICAL PROPERTIES OF THE GFRCP COMPOSITES.	34
TABLE 3: MEASURED TEMPERATURE COEFFICIENT OF RESISTANCE	38
TABLE 4: PARAMETERS OF THE IN-SITU MONITORING OF GFRCP COMPOSITE.....	39
TABLE 5: EMI SE COMPARISON SUMMARY WITH VARIOUS MATERIALS.....	55
TABLE 6: COMPARISON BETWEEN EMI SE RESULTS WITH EXPERIMENTAL AND THEORETICALLY CALCULATION FOR 1 MM THICK SAMPLE MADE OF PANI-DBSA-DVB CONDUCTIVE RESIN.	58
TABLE 7: SUMMARY OF APPLIED SIMULATED LIGHTNING CURRENTS ON CFRP COMPOSITES.....	66
TABLE 8: SUMMARY OF APPLIED SIMULATED LIGHTNING CURRENTS ON GFRP COMPOSITES.	66
TABLE 9: SUMMARY OF RESIDUAL MECHANICAL STRENGTH ANALYSIS	74

Nomenclature

FRPs	Fiber Reinforced Polymers
CFRP	Carbon Fiber Reinforced Polymer
GFRP	Glass Fiber Reinforced Polymer
EMI	Electromagnetic Interference
LSP	Lightning Strike Protection
PANI	Polyaniline
EB	Emeraldine Base
DBSA	Dodecylbenzenesulfonic Acid
DVB	Divinylbenzene
CF	Carbon Fiber
CNF	Carbon Nanofiber
CNT	Carbon Nanotube
MWCNT	Multiwall Carbon Nanotube
PDD	PANI-DBSA-DVB
NRC	Normalized Resistance Change
GF	Gauge Factor
GFRCP	Glass Fiber Reinforced Conductive Polymer
SE	Shielding Effectiveness

Chapter 1

Introduction

1.1 Motivation

In-service damage and failure of metallic structures are comparatively well established. Typically, it arises because of impurities and or flaws present in metals and propagation under loading. In contrast, composites are heterogeneous. Their failure mechanisms not only complicated but also not clearly understood yet. The failure studies not only help to predict the composite structures' life span but also helps to improve its properties. Weight of the structure is the primary factor that all engineer aims to reduce without compromising its other properties like strength. Since last decades, carbon fiber reinforced polymer (CFRP) composites are introducing as a primary aircraft structural material [1]. Along with CFRP composites, glass fiber reinforced polymer (GFRP) composites not only getting popularity in the aerospace industry but also other sectors like wind turbines, automobile, civil structures, because of its high specific strength, corrosion resistance, fatigue strength and strength to cost ratio [2–4]. Even though these materials getting popularity in various industries, but also facing challenges and limitations. One of the limitations is that these are poor in electrical conductivity. As a result, these structures facing threats like electromagnetic interference (EMI), lightning strike damages (refer Figure 2), etc., which are of concern for the safety of aircraft and other structures [5]. This, in turn, requires additional EMI shielding, expensive damage repairing caused by the lightning strike, which leads to increased operational costs. There has been a vaster need for multifunctional structural composites that not only act as an EMI shield for the avionic equipment such as flight recorders, navigation units, flight-control systems, and radios [6] but also can protect from lightning strike (LS) damages, etc. In addition to the above two severe threats, composite structures are associated with health monitoring due to its heterogeneous nature. Additional monitoring setup networks (refer Figure 3) not only increase the overall weight of the structures but also sometimes degrade its mechanical properties when embedded with the structures. It is equally important to improve the composite properties to act as a self-sensing structural.

Inspired by the above mention challenges and its concern on aircraft safety, current research focused on the design and development of advanced multifunctional materials. The motivation is to investigate and develop multifunctional, structural materials, and suitable fabrication process. The ability to actively perform multifunctionality of a composite can significantly reduce the overall weight and cost of the composite structures without losing its other properties and enables us to create multifunctional composites materials.



Figure 1: KLM Boeing 777-300 being struck by lightning, filmed by Ralph Valkenier of KLM Apron Services. [7]

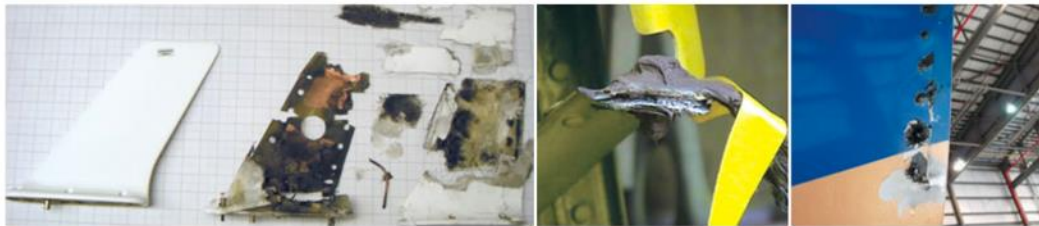


Figure 2: Lightning damages of the aircraft components. Left to right: bond jumper, antenna, and rudder. [8]

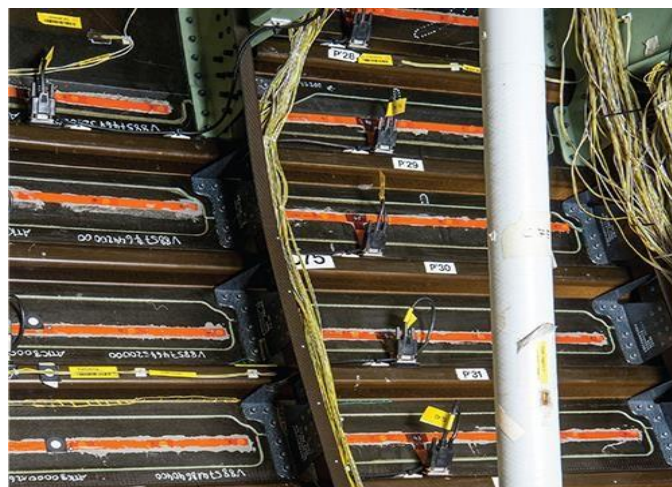


Figure 3: SHM impact damage detection system sensor network installed in the A350 XWB CFRP composite panel. [9]

1.2 Objective of the Thesis

The objective of this thesis is to improve the electrical properties of the composites by introducing novel conductive polymer system and different fabrication processes to achieve new multifunctional behavior. Explore different functions like strain sensing, EMI shielding, and LS protection and suitable fabrication process to create composites with tunability conductivity and of its useful properties, behavior, and attributes.

More specifically, the objectives of the thesis are to address the following points

- Understand the piezoresistivity response of the novel polyaniline (PANI) based conductive thermosetting polymer system to utilize it in the strain sensing application.
- Characterize the novel polyaniline based conductive thermosetting polymer system as a strain sensor, including sensitivity, reliability, reversibility, thermal stability, and evaluate its working range.
- Fabricate self-sensing structural strain sensor using characterized novel polyaniline based conductive polymer system and reverify its strain sensing properties.
- Understand the different EMI shielding mechanisms of the novel polyaniline based conductive polymer system and its effects on the EMI SE.
- Estimate the dielectric properties and their influence on EMI SE.
- Understand the influence of the shield thickness and conductivity to the EMI SE.
- Understand the lightning strike protection (LSP) mechanism of polyaniline based conductive layer on CFRP and GFRP composites and optimize the LSP layer thickness.

1.3 Background

1.3.1 Composite Materials

The term composite materials define the development of a new useful material blending with two and more materials on a macroscopic scale. Examples from ancient times, both plywood, Medieval swords, and armor, were made of different layers of materials; from the recent era, fiber-reinforced resin matrix composites. These composite materials further classify as [10]

- Fibrous composites (fibers in matrix)
- Laminated composites (layers of materials)
- Particulate composites (particles in matrix)
- Hybrid composites (combination of above three)

Since the 1950s, Boeing introduced the use of E-glass laminated composite for their secondary structural parts like flooring, cargo liners, air ducts, and various other cabin parts in B707. The development of the aerospace industry is focused on the performance improvement of the commercial and defense aircraft by improving the performance of the structural materials. Composites one of the promising materials for current and future aerospace components (refer Figure 4) [11]. Laminated CFRP composites are mostly used for the aerospace industry. This type of composite consists of different layers of fiber-reinforced polymer laminae, which gives more freedom to design the laminate according to the applied load. Figure 5 represents the two-principal type of laminae; however, the current study adopted lamina with woven fibers.

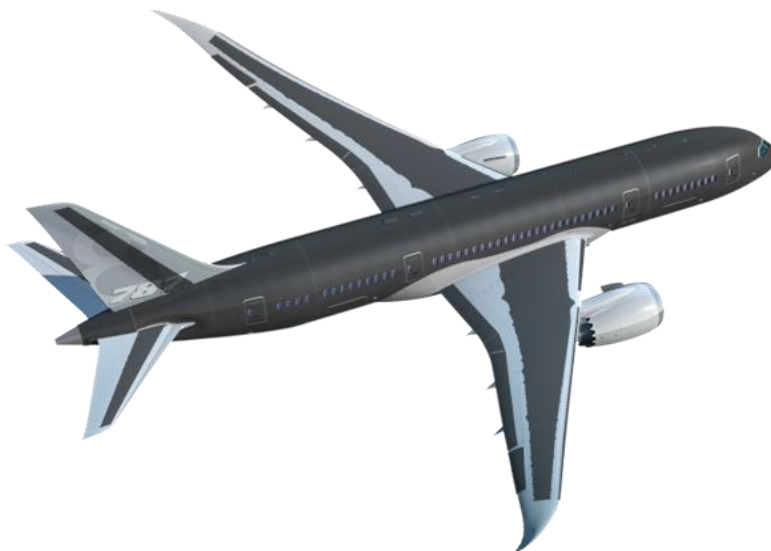


Figure 4: Advanced CFRP composites used in Boeing 787 Dreamliner.[12]

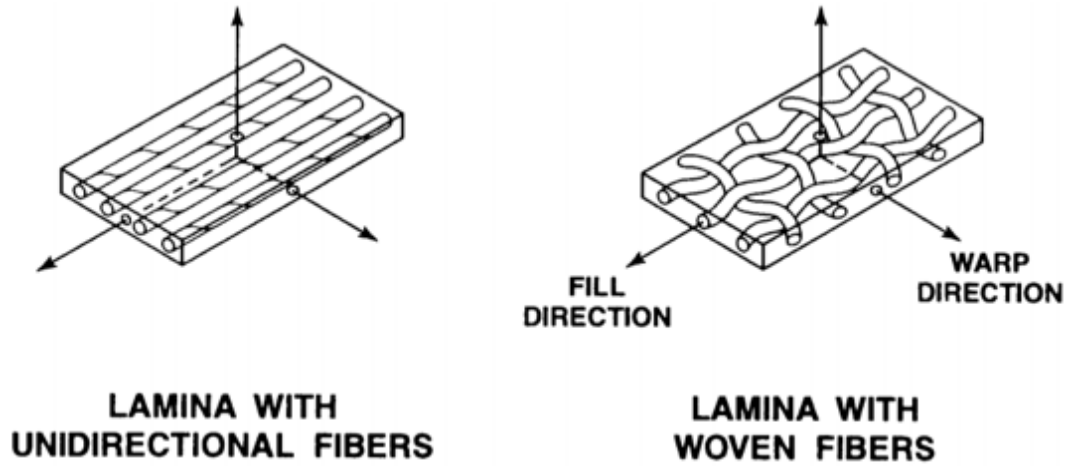


Figure 5: Two principal types of laminae. [10]

1.3.2 Multifunctional Composites

Multifunctional structural composites are the materials that qualified both structural and non-structural functions without attached or embedded [13]. The non-structural functions could be wider range starting from sensing (strain, stress, damage, temperature etc.) based on piezoelectricity and thermoelectricity, EMI shielding to protect the electronics devices and shield the EM wave at sources based on EM radiation absorption and reflection, LSP to protect the structure from direct and indirect lighting strike damages on the structures based on conductive network, deicing and anti-icing based on Joule effect and actuation based on converse piezoelectric effect [13]. CFRP composites are electrically conductive as compare to GFRP composites. However, in CFRP composites, carbon fibers are provided the conductivity of the composites, due to insulating nature of the matrix material. Consequently, the conductivity of CFRP composites is depending on the fiber alignment, degree of fiber – fiber contact, degree of delamination and degree of fiber damages. As a result of these dependency, CFRP composites are sensitive to strain, damages and temperature in the composite. This is the principal of resistance-based sensing application of the CFRP composites. The conductivity of the CFRP composites also allow to reflect and absorbed the EM radiation to act as an EMI shielding. Moreover, conductivity of CFRP composites allow to serve as a heating element in resistive heating or Joule heating, which is relevant to deicing and anti-icing. To the contrary, GFRP composites are insulating nature, how adding conductive nanofillers like carbon nanotubes, carbon nanofiller, carbon black and graphene in insulating matrix can improve the electrical conductivity and can get similar functionality like CFRP composites.

Electrical resistance-based strain sensor was first reported by Schulte and Baron in 1989. In the last two decades, various researcher uses this principal and developed multifunctional composite sensors, mostly focus on CNTs and nanofillers based composites.

1.3.3 Conductive Nanofillers Polymers

Other than ICPs, different nanofillers also mixed with insulating polymers to devolve a conductive polymer system. The common nanofillers used to develop conductive composites are carbon nanotubes (CNTs), graphene, and metal fillers (refer to Figure 6). To produce conductive polymers, these nanofillers mixed with insulating polymers. However, when nanofillers are mix with insulating polymers, they experience issues like agglomeration in the system, which is very common in CNTs. The percolation limit for the metal fillers is too high, which makes those conductive polymers heavy. Graphene having stacking issues, they tend to accumulate one after another in the polymer matrix. Over that, their conductivity network more complicated.

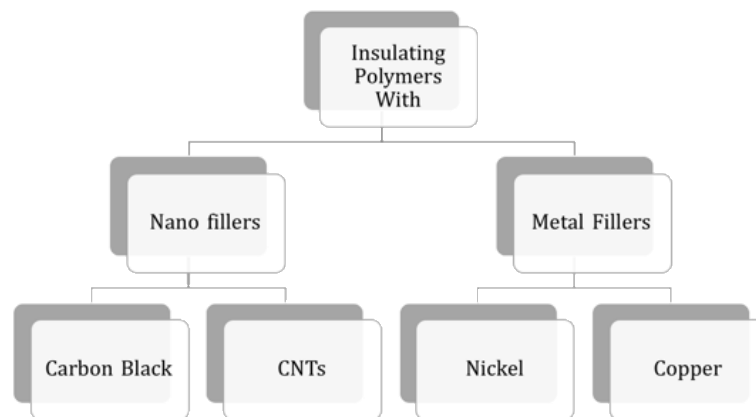


Figure 6: Common nanofiller conductive polymer system.

1.3.4 Intrinsic Conductive Polymers

Intrinsically conducting polymers (ICPs) are commonly known as synthetic “metals” as they have similar properties (electrical, magnetic, and optical) typical of metals and semiconductors. Since the discovery of the ICPs in 1970, may researcher working on these materials for various engineering application staring from polymer light emitting diodes (LEDs), corrosion resistance, electromagnetic shielding, sensor technology, molecular electronics, supercapacitors, and electrochromic devices [14]. The intrinsic conductivity arise from the conjugation single and double bonds of their carbon backbone [15]. Commonly used organic conductive polymers are poly(acetylene)s, poly(pyrrole)s, poly(thiophene)s, poly(aniline)s,

poly (3,4-ethylene dioxythiophene), and poly (phenyl vinylene). Among the different ICPs, PANI has been used because of its ease of synthesis, stability, the possibility to control the size, and formation of hybrid structure [16].

1.3.5 Novel Polyaniline-based Conductive Polymer System

1.3.5.1 Polyaniline

PANI commercially available in its three-oxidation forms, i.e. (i) leuco-emeraldine (LE) fully reduced state; (ii) per-nigraniline (PG) fully oxidized state; and (iii) emeraldine consists of both, also cited as emeraldine base (EB). Out of these three forms, the emeraldine base is very stable and can be doped with imine nitrogen protonated by an acid. PANI is having a wide range of electrical conductivity from 10^{-13} to 10 S/cm [16].

The conductive mechanism of the PANI system (refer Figure 7) can be express form Figure 8. PANI also having conjugated single and double bonds along the polymer chain. Both single and double bonds include a localized sigma-bond, which forms a strong chemical bond. Additionally, each double bond also contains a localized π -bond, which is weaker. This conjugated π -bond form delocalized electrons cloud, which allows electrons to flow along the polymer chain [17]. For the graphical presentation of the mechanism, refer to Figure 8. However, this condition does not satisfy the conductivity of the PANI, unless an intrinsic charge-carriers is developed. Once the charge carriers are generated, the bandgap is reduced, and the PANI system becomes conductive [18]. The charge-carriers are delivered externally, which commonly known as doping. In this research, the EB form of PANI was used.

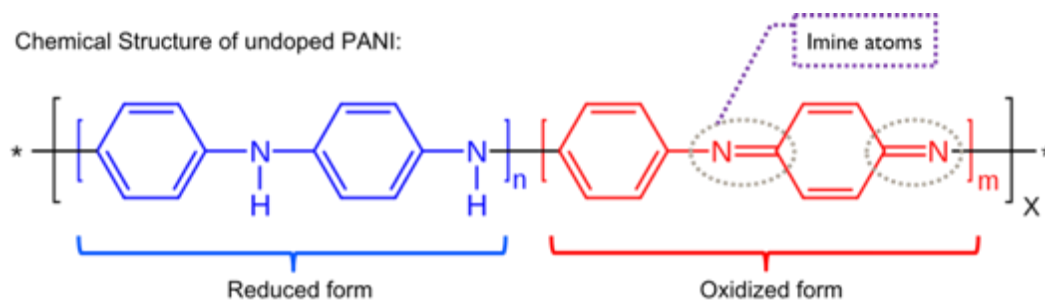


Figure 7: Chemical structure of PANI.

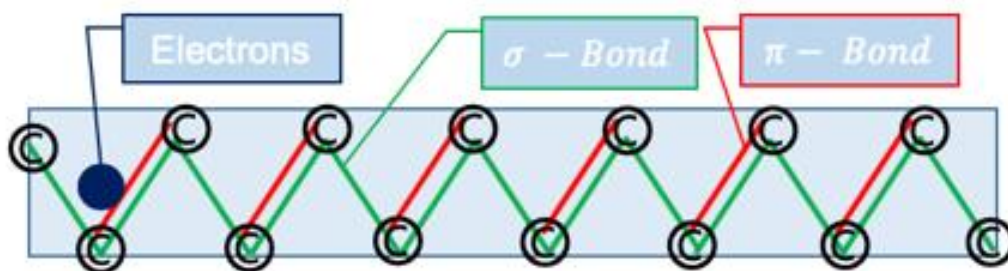


Figure 8: Schematic diagram of the PANI conductive mechanism.

1.3.5.2 Dodecylbenzene-Sulfonic Acid

Figure 9 shows the chemical structure of dodecylbenzene-sulfonic acid (DBSA). The DBSA commonly function both as surfactant and dopant due to bulky molecule with a polar head and a non-polar chain. In this study, DBSA used as a dopant for PANI. Several researches reported DBSA as a dopant for PANI [19–22]. For instant, Eduardo L. Subtil et al., investigation on the use of PANI and reduced graphene oxide as conductive dopants, along with camphor-sulfonic acid and dodecylbenzene sulfonic acid (DBSA) for PANI preparation and reported higher conductivity was obtained for PANI-DBSA ($4.5 \pm 0.3 \mu\text{S}\cdot\text{cm}^{-1}$). Similarly, Kumar et al., extensively worked on PANI-DBSA for their novel conductive matrix development [23–25].

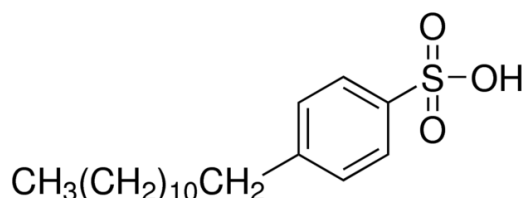


Figure 9 : Chemical structure of dodecylbenzenesulfonic acid

1.3.5.3 Divinylbenzene

Divinylbenzene (DVB) in the monomer 2 places unsaturated. It is generally used as cross linking polymer to improve the mechanical property of the polymer. There are several advantages of the DVB, like fast curing, high mechanical properties, however proper dissolve of PAN-DBSA mixture is a manufacturing challenge. Kumar et al., optimized the PANI – DBSA mixture for proper dispersion it in the DVB matrix [23–25]. However, further modification done it this research based on the application.

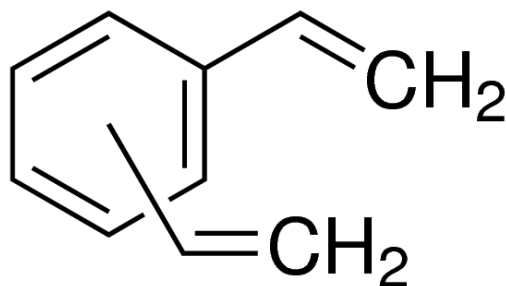


Figure 10: Chemical structure of divinylbenzene

1.3.5.4 PANI-DBSA-DVB (PDD) System

The novel conductive polymer (refer as PDD system throughout the thesis) consists of an EB form of PANI, DBSA, and DVB, these were purchased from Regulux Co. Ltd, Kanto Chemical Co. Inc. and Sigma-Aldrich Co., respectively. To prepare the novel polyaniline-based conductive polymer system, firstly, the PANI-EB powder was mixed with the DBSA using a centrifugal mixing machine (2000 rpm for 30 secs clockwise and counterclockwise, four sets). The mixture was made in a weight ratio of 1:2. This weight ratio was selected considering the ideal molar ratio for emeraldine salt (2:1) and the processability of the mixture [26].

Further, the PANI-DBSA mixture was kept in the oven at 60 °C for 6~8 hours. This intermittent thermal treatment is termed as thermal semi-doping [26]. Secondly, the semi-doped complex (PANI-DBSA) was mixed with the DVB manually in a weight ratio of 1:1. For homogeneous mixing, PANI-DBSA and DVB mixture were mixed in the centrifugal mixer. The BYK-054 solution was then used for degassing the mixture. Finally, the homogenous mixture of PANI-DBSA and DVB further used according to requirements and cured in the hot-press machine. The curing profile of the samples plays a vital role in achieving the desired range of conductivity and mechanical strength of the specimens. The temperature and the pressure were optimized to achieve the maximum strength and conductivity in the range of 0.1 – 1.0 S/cm. The fabrication process schematic diagram is shown in Figure 11. The novel polyaniline-based conductive polymer system will be considered as “PDD system” in this thesis.



Figure 11: Fabrication process of polyaniline based novel polyaniline-based conductive polymer system.

1.3.6 Electrical Resistance Measurement Techniques

1.3.6.1 Two-wire Methods

Figure 12 represent the sample configuration for two-wire resistance measurement technique. To measure the resistance of the specimen under test, digital multimeters are used. In these multimeters, device measure the voltage drop at the two electrode terminals for a known current supply. In case of two-wire resistance measurement technique, both voltages drop and current measurement is done at the same electrodes. Consequently, the lead resistance added to the measure and misleader the measured resistance. This error become significant when low resistive materials are measured. It is not recommended to measure the materials which is less than 100Ω .

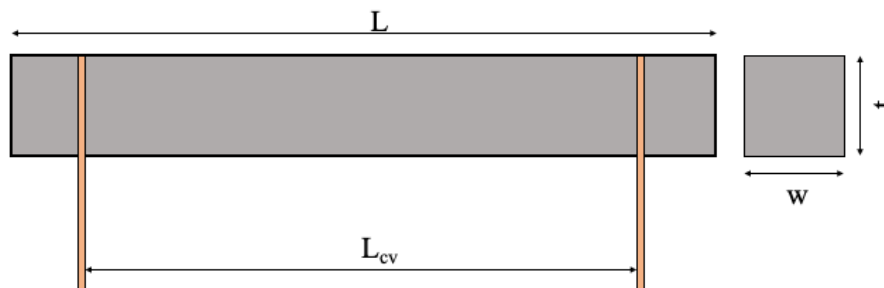


Figure 12: Specimen configuration for two-probe resistance measurement technique

1.3.6.2 Four-wire Methods

Figure 13 represent the samples configuration for four-wire resistance measurement technique. Due to limitation of the two-wire resistance measurement, four-wire resistance measurement technique developed. In this technique, four equally separated ports/electrodes are used to measure the voltage and supply the current. Two extreme (outer) ports/electrodes used to supply the current to the specimens. Whereas, closest (inner) posts/electrodes were used to measure the voltage drop. A high resistive voltmeter used to reduce the current flow through it.

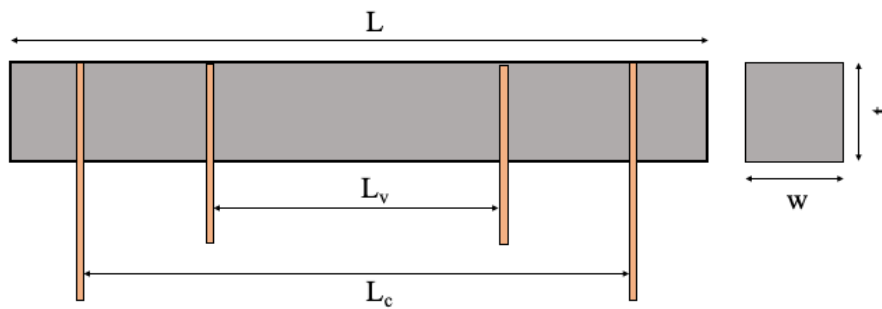


Figure 13: Specimen configuration for four-probe resistance measurement technique

1.3.7 Literature Review

The piezoresistivity is the phenomenon in which the electrical resistivity changes with strain. This phenomenon is very useful and helps to measure strain, from resistivity change under strain. The sensitivity of these sensor measured the parameter call, gage factor, which is defined as the fractional change in resistance per unit strain. In the past decades, polymer composites are also filled with carbon nanomaterials (CNMs), e.g. carbon nanotubes (CNTs), graphene, carbon nanofibers and carbon blacks (CB) to improve the sensitivity of the strain sensors under different loading conditions [27]. In all cases, electric resistance changes with the change in mechanical strain are correlated for strain sensing and damage.

S. Lu et al. worked on graphene platelets (Gn/Ps)/epoxy as a sensor and later fabricate it as coating surface on the GFRP composite. They are able to capture the linearity and recorded the sensitivity as 9. Different loading condition also confirmed the stability and repeatability [28]. X. Cao et al. studied on multi-walled carbon nanotubes (MWCNT)/epoxy conductive composite's strain sensing behavior. They conclude their work by saying that resistance sensitivity $\left(\frac{\Delta R}{R}\right)$ linearly increase and then decrease non-linearly. The mechanism of the linear zone and non-linear were expressed as decrease of nanotube contact points and the reorientation and alignment of nanotube respectively [29]. G. Georgousis et al., two individual

works, first work was on PVDF/MWCNTs composite with different filler content. Work summarized that, the different composition can be used for the different strain level [30]. In the latest work, styrene-Butadiene Rubber reinforced with two different fillers, i.e. CB and CNTs. The work highlighted that, electrical resistance changes highly depend on different nanofiller's geometry and dispersion when material subjected to different loading condition. Also highlighted that, the network between nanoparticles is destroyed during loading and reformed on unloading [31]. Similar to above works, other researches also worked on CNMs and reported the good agreement of electrical resistance change and tensile strain, like X. Wang et al. worked on buckypaper [32], H. Yazdani et al., on CB in PVC composite [33] and so on. But, in the other hand PANI based sensors studies are limited to gas sensor [34][35], electrochemical sensor [17][36] and author did find out any potential work on strain sensor. For EMI shielding, researched tried to developed new materials introducing different conductive nano-fillers. For an instant, Bora et al. reported that vinyl butyral-PANI-Ni-fly ash cenosphere (thickness $259\ \mu\text{m}$) and Poly (vinyl butyral) polyaniline ($268\ \mu\text{m}$) film able to perform SE up to $\sim 23\ \text{dB}$ and $\sim 13\ \text{dB}$ respectively in the X-band frequency. The also highlighted that the absorption is the primary mechanism for both the materials [37]. Gopakumar et al. demonstrated that flexible conductive cellulose nano-papers, made of continuous coating of PANI over the cellulose nanofibers during in situ polymerization. These composite nano-papers exhibited average SE of $\sim 23\ \text{dB}$ at $8.2\ \text{GHz}$ with $1\ \text{mm}$ paper thickness. Similar to Bora et al., this study also concludes that absorption is the predominating mechanism for the EMI shielding [38].

Further, Zhang et al. showed the improvement of SE by adding few-layered $\text{Ti}_3\text{C}_2\text{T}_x$ with co-doped PANI using dodecylbenzene sulfonic acid (DBSA) and hydrochloric acid (HCl) [39]. They reported the improved SE values up to $\sim 36\ \text{dB}$ with high conductivity of $24.4\ \text{S/cm}$. In most of the cases, PANI has been successfully introduced as a flexible EMI shielding film. However, few reported it as a structural shielding material [40,41].

There is a need for advanced multifunctional structural composite materials not only in the aerospace industry but also in other fields like immersing electric cars, civil structure, and wind turbines. A single material that not only acts as structural materials but also supports other functions like, protect from the lightning strike, shield from EMI noise, strain sensing, etc. The objective of the present work is to study the EMI shielding property of the PANI-based structural conductive thermoset resin in X-band ($8.2 \sim 12.4\ \text{GHz}$). Also, it's implementation on FRPs as a conductive layer to developed a self-shieling structural material. The material is

easy to prepare, economically feasible, and easy to apply. The conductive layer consists of dodecylbenzene sulfonic acid (DBSA)-doped PANI dispersed in a thermosetting polymer divinylbenzene (DVB). The minimum weight of the overall structures of aerospace is one of the critical requirements; keep it that in mind, the current research able to maintain the density of the PANI-based conductive layer as low as to 1.5 g/cm^3 . The average conductivity range of layer is around 50 -100 S/m.

Similarly, for LSP several approaches have been initiated to improve the electrical conductivity of the insulating matrix materials. The carbon materials such as carbon fibers, carbon nanotube (CNT), CNT paper (buckypaper) films, graphene and graphite were used in conventional insulating matrix materials to improve the mechanical, electrical and thermal properties of composites [42–48]. For instant, Hirano et al [42] worked on graphite/epoxy composite laminate to do damage assessment under lightning strike. Different damage evaluation techniques were used to quantify the damages both qualitative and quantitatively. It can be summarized from the damage evaluation results that the mode can be categorized into fiber damage, resin deterioration, and internal delamination. It is also noticed that orthotropic electrical properties of the lamina governed the lightning damage progression, and the impulse waveform. However, this study didn't notice the damage effects based on specimen size and thickness variation. Gou et al. were also developed a conductive paper layer with the help of carbon nanofibers and nickel nano stands [44]. A peak current amplitude of 100 kA to simulate the lightning strike. It is found that even at high surface conductivity ($\sim 34100 \text{ S/m}$), the sample is failed to simulated strike. They reported with these high surface conductivity samples were damaged by 30 ~ 40 % of its thickness on an area of $\sim 45 \text{ cm}^2$ [44]. Further, Chakravarthi et al. also developed bismaleimide–carbon fiber composites filled with nickel-coated single-walled carbon nanotubes. According to MIL-STD 1757A (Zone 2A lightning strike) standard, they were conducted simulated lightning to qualify the material. However, they found, the carbon fiber pull-out for composites is 5.17 cm^2 , which is almost 85 % reduction compared to without conductive fillers [43]. In recent years, Rajesh et al. reported the damage response of CFRP coated with two types of coatings. Hybrid coatings consisted of silver nanoparticles dispersed in conducting polymer PEDOT: PSS, and silver-coated carbon-nanofiber transferred onto an epoxy surfacing film. For metallic coatings, continuous coatings of silver, and a composite of 10 % copper in the tin were considered [46]. With $\sim 38 \text{ kA}$ peak current lightning test, the specimen with Cu/Sn coating (0.38 mm thick with 0.12 ohm-m resistivity) able to retain the damage up to top surface level (damage area $\sim 14 \text{ cm}^2$), all other coating failed to do

that. In most of the above cases, researches were tried to modify the composite constitution by adding conductive filler to improve the conductivity and to qualify the corresponding materials for LSP, and able to showcase some extend improvements compares to conventional CFRP composites. However, modification of composites' constitution involved various difficulties for commercial application, like upgradation of the fabrication process and equipment, which involved additional capital investments. In the other hand, conductive layer on composites can minimize several aspects, including capital investment, overall cost and weight. So, further development needed to improve the composites without changing its constitutions.

Intrinsic conductive polymers, specially PANI, are also studied for high conductive composite development [5,49–51]. Kumar et al. studied both PANI-based composites and a conductive layer on CFRP composites. In both cases, these materials able to retain more than 90 % of its residual strength under a peak current of 40 kA and 100 kA, respectively [49,50]. 'Weight', one of the primary factors of aircraft design. Keep that in mind; it is also essential to optimize the conductive layer to qualify as a lightning strike protect materials. In this study, a polyaniline-based conductive thermosetting layer was studied with different thickness and peak current load to optimize the thickness of the layer for LSP application.

The objective of this study is to optimize the thickness of the PANI-based conductive layer for LSP. To achieve the objective, a simulated lightning current magnitude of 40 kA was strike on CFRP composites with two different thicknesses of the PANI-based conductive layer. To assist the direct damages on the CFRP composites, visual inspection, high-speed video data, ultrasound test results, microscopic images, and residual strength data were used. The assessment from the test results was discussed and recommended optimum PANI-based conductive layer thickness for LSP application. Further extension of the current research, similar techniques were used and implemented on GFRP composites. Two different thickness was chosen for the study however, peak current was extended to -100 kA.

1.4 Overview of Thesis

The investigated studies reported in the thesis will focus on the above mentioned three scopes of the application. This thesis represents the design and fabrication of a novel polyaniline-based strain sensor and uses it as an example of self-sensing structural strain sensors. Further, it also discusses its other function as a shield for EMI radiation and LSP. The focus of the work is on the application of the phenomenon concerning the design and fabrication process of multifunctional structural material for aircraft; therefore, we refrain from scientific analysis at molecular or material science level. Studies are restricted to observation and application in major composite industries.

Chapter 2 will discuss the design and development of a polyaniline-based structural strain sensor. Discussed the choice of crucial design parameters, particularly concerning the working range of the sensor, reliability, and stability. Also, examine the different fabrication processes and verified the performance for real-world applications. Then move to discuss other functions of the material in the subsequent chapters.

Chapter 3 talk about another functionality of the material, i.e., electromagnetic shielding. Different mechanisms like reflection, absorption, and multiple-reflection were thoroughly investigated for the material, and their effects on overall SE are also discussed in this chapter. A comparison between theoretical and experimental results of overall SE also discusses addressing the impact of multiple-reflections. Finally, different dielectric properties are estimated from S-parameters with the help of the NRW algorithm to understand the shielding mechanisms.

Chapter 4 discussed about the LSP system for aircraft and highlighted the key achievements of the material in this regard. The importance of the PDD layer optimization for LSP system has been discussed. Two different materials i.e. CFRP and GFRP composites with PDD layer has been studied and discuss their failure mechanisms under different simulated peak lightning currents.

A conclusion summary was made in

Chapter 5 based on the previous discussion and results and lays down the foundation for further work in this area.

Chapter 2

Structural Strain Sensor

2.1 Introduction

The fiber-reinforced polymer (FRP) composite structures often experience different loading conditions during their functionality, and the mechanical performances severely degrade when micro damages occur [28]. Therefore, it is essential to monitor these structures during its functionality. Different types of sensors are widely used for monitoring the deformation and damage in FRP composite structures. However, the researcher is focused on developing advanced sensing structural strain sensor composites to eliminate additional sensing systems. The common or most studied in this regard is that adding various conductive nano-fillers in the insulated polymers [52]. The homogeneous dispersion of these conductive nano-fillers into the insulating polymer is the main challenge for future research [53]. An alternative way to develop conductive polymer composite is to replace conductive nano-fillers with intrinsically conducting polymers like polyacetylene, polypyrrole, polyindole, and polyaniline [5,54,55]. Since the discovery of the conducting polymers by Shirakawa et al., there has been extensive research is going on to find their applications in various fields. Owing to several advantages like high stability, low cost, easy processability, and controllable conductivity, PANI is the most extensively studied conducting polymer among its counterparts [56]. In recent years, Kumar et al. have developed the PANI-based structural high electrically conductive thermoset polymer and used it to fabricate high conductive CF/PANI composites [5,23,26,57,58]. In the past few decades, PANI conductive composites have been studied for various applications like supercapacitor [59–61], energy storage [62–64], corrosion resistance coating [65,66], gas sensor [67–69], flexible strain sensor [70] and many others [71–73]. PANI has been extensively studied as a flexible strain sensor. Among them, P. Costa et al. reported several works on PANI-based thermoplastic piezoresistive sensors [74–76]. In their recent work, they said doped PANI mixed with elastomer styrene-ethylene/butylene-styrene (SEBS) for large strain sensing applications. A high conductivity (1 S/m) has been reported with a gauge factor of 1.5 -2.4 for the deformation up to 10 %. They showed that these excellent properties and the sensor's responses are suitable for stretchable force and deformations [74].

Further, it will be more innovative if a mechanically stiffened strain sensor is developed that can be conveniently used as a structural composite. As per the extensive literature survey conducted, there have been no reports yet on the PANI-based structural strain sensor. This research focusses on a structural strain sensor fabricated using PANI based polymer system. In this section, a novel conductive thermoset polymer, i.e., PDD system consisting of polyaniline, dodecylbenzene-sulfonic acid, and divinylbenzene, has been demonstrated as a strain sensor under different static loading conditions. The four-probe electrical conductivity measurement method was adopted to measure the change in electrical resistance of the material for the applied static load. A comprehensive study was conducted to characterize the sensor by estimating the working range of the sensor considering the hysteresis effect, creep behavior, and long cyclic load effect. A strain rate change effect and thermal stability study were also conducted to characterize the sensor. Moreover, the gauge factor was calculated, and its stability over the working range was studied. The results show that the sensor is suitable for low strain measurements in a range of 0.025 ~ 0.3 % strain. However, it can also be used for damage detection at the higher strain level. These responses are significant to qualify the PDD polymer system as a multifunctional material. Further, for the demonstration purpose, both impregnated and layer-based fabrication process was adopted to fabricate a novel polyaniline based self-sensing structural strain sensor. These demonstrations tests were confirmed the strain sensing parameters.

2.2 Sample Preparation

For strain sensing characterization, initially, a pure PDD system was characterized followed by glass fiber reinforced conductive polymer (GFRCP) composites and PDD layer on GFRP composites. For all cases, the PDD resin system was prepared, as described in section 1.3.5.4.

2.2.1 PDD System

For pure PDD resin samples preparation, dog bone specimens were prepared with the help of aluminum mold. The liquid PDD system then pours into the mold and cure on a hot press. The curing profile of the samples plays a vital role in achieving the desired range of conductivity and mechanical strength. The temperature and the pressure were optimized to achieve the maximum strength and conductivity in the range of 0.1 – 0.4 S/cm. A curing profile of 165 °C under 3 MPa pressure was used to cure the samples in the hot-press. The specimen's schematic diagram is shown in Figure 14.

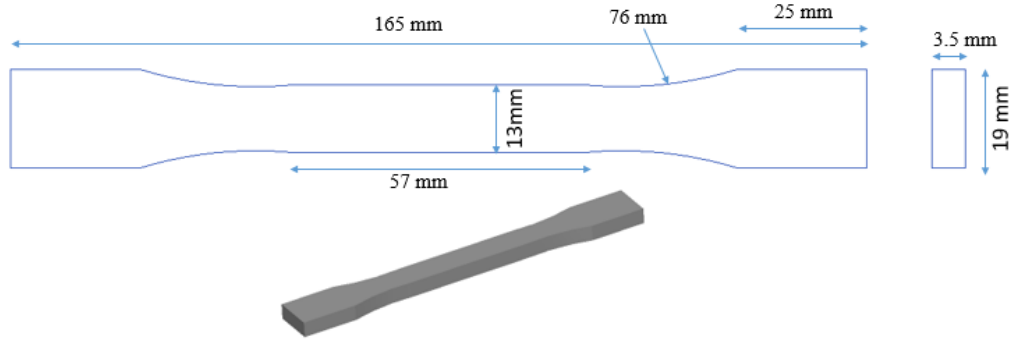


Figure 14: Dog-bone samples and their dimensions made with the PDD system.

2.2.2 Glass Fiber Reinforced Conductive Polymer (GFRCP) Composites

The conductive PDD system was further used to fabricate the GFRCP composites. Every eight plies (200 x 200 mm) of plain-woven E-glass fiber fabrics (625GSM, SAERTEX GmbH & Co. KG) were impregnated with PDD conductive resin and stacked one after another in loading direction $[0/90]_8$. Then the stacking was further cured in hot press. The curing temperature was increased from 23 °C to 165 °C at a rate of 10 °C/min. A pressure (3 MPa) was applied once the hot press reaches 110 °C. Once temperature reaches preset curing temperature value, the hot press was cooled down rapidly using water flow. This cooling profile was optimized for high conductivity and mechanical strength. The cured GFRCP composite was later cut into rectangular coupons (180×18 mm). The average thickness of the panel was 1.7 mm. The geometry of the composite coupons is shown in Figure 15.

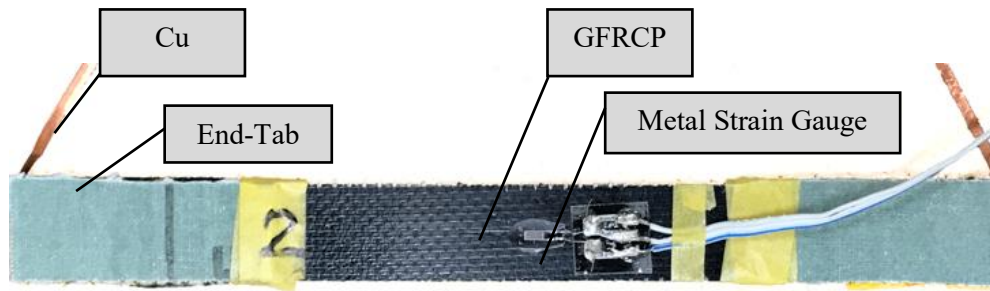


Figure 15: Rectangular GFRCP composite coupon with attached strain gauge and electrodes.

2.2.3 PDD Conductive Layer on GFRP Composites

To fabricate the PDD conductive layer on GFRP composites specimens. Initially, GFRP composites were fabricated separately with the help of a vacuum-assisted resin transfer molding (VaRTM) technique. The GFRP composite panel was made of ten plies (200 x 100 mm). The cured composite panel was later cut into rectangular coupons (200 × 12 mm). The

average thickness of the GFRP panel was 1.96 mm. The geometry of the composite coupons is shown in Figure 16. The sandpaper was used for surface preparation before the attached PDD layer on top of the composite coupons. A polymer-based adhesive was used to attached the PDD conductive layer on composites.

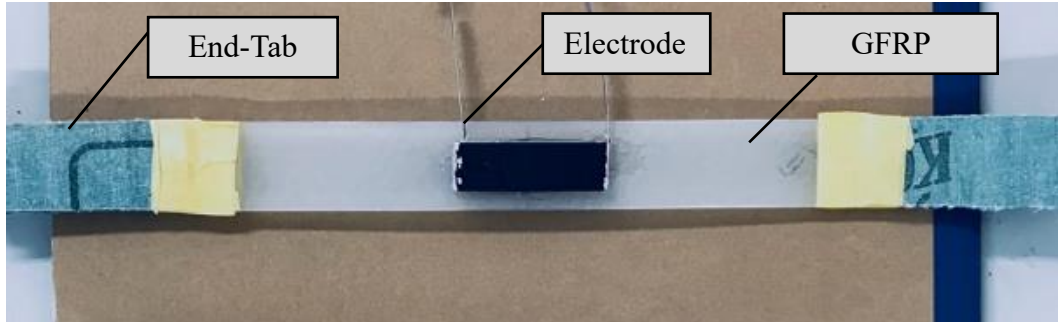


Figure 16: GFRP composite with PDD layer on it.

For all samples, the sandpapers were used for gripping the specimens into the tensile test fixtures. To measure the specimen's exact strain and resistance change under loading, conventional metal strain gauges, purchased from TML and electrodes were attached in each specimen. Electrodes were prepared from the copper tape and attached to the samples with dotite (D-500) silver paste. For the silver paste curing and proper bonding between the electrodes and the samples, they were kept in the oven for 45 mins at a temperature of 60 °C. To ensure the electrodes were stress-free during loading, they were mounted at free edges (i.e., behind the gripping area) of the specimens.

2.3 Characterization

To characterize the sensor, several loading – unloading cyclic strain measurements were performed. For all measurements, samples' electrical conductivity was maintained in a range of 0.1 S/cm to 0.4 S/cm. To obtain the results, a simultaneous measurement was done using strain tester (TML DRA - 101C), universal testing machine (Instron-5582), and the digital multimeter (Keithley 2110). The electrical resistance measurements were performed with four probes technique to eliminate contact resistance. The mechanical tests were carried out in a displacement control mode. A complete setup of the experiments is shown in Figure 17.

For this study, the following plan was designed to characterize the sensor. Each set of measurements was done using three sets of virgin samples [76,77].

- **Monotonic Tensile Load:** Samples were loaded monotonously until failure at a constant strain rate of 1 mm/min. This experiment helps to construct the sensor's

characteristic curve (Normalized Resistance vs. Strain) under monotonic tensile loading.

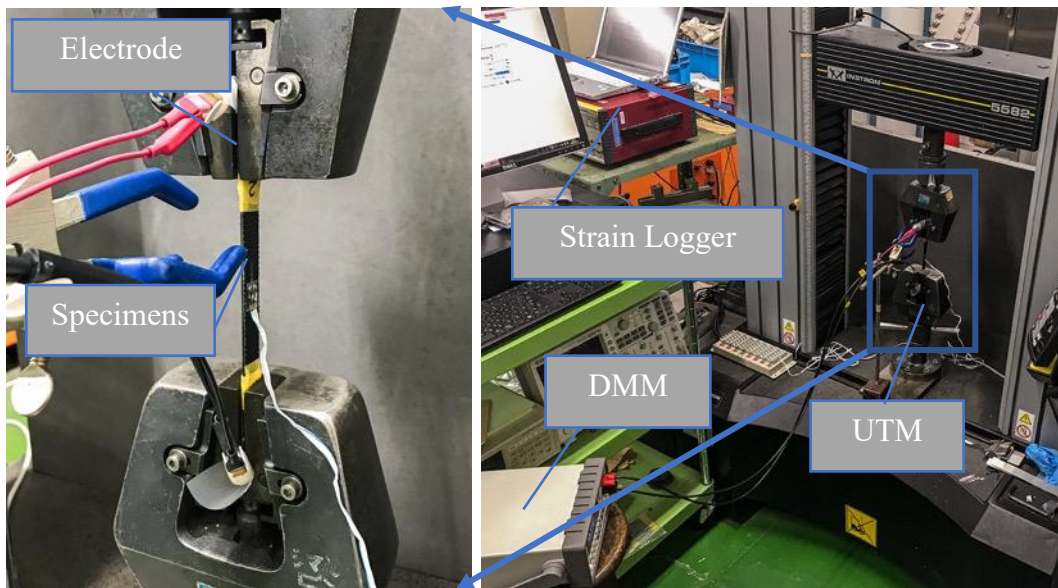


Figure 17: Experiment setup of the in-situ resistance change monitoring test.

- **Varied Strain Study:** This step includes the resistance measurement by varying the elongation till 1 mm in the intervals of 0.1 mm starting from 0 mm. Further, the strain interval was lowered to 0.01 as well to verify the low strain effectiveness of the sensor. The strain was varied in the following set: 0.1, 0.2, 0.4, 0.6, 0.8 and 1mm elongation. Then further in the lower strain region, it was studied for; 0.07, 0.05, 0.03, and 0.01 mm. Each step has three cycles of measurement. With these experiments, some insights like linearity, (determine the working range), repeatability, and the stability of the sensor were confirmed
- **Increasing - Decreasing Load Level:** The measurement of resistance starts with a high load level and decreases stepwise and then increases stepwise. This measurement study was done to determine how the characteristic curve changes with the maximum load applied.
- **Load - Hold – Unload:** Two sets of holding tests were conducted with the working range of the sensor to verify the relaxation behavior. The measurements were done in two different strain rates of 1 mm/min and 0.1 mm/min.
- **Varying Strain Rate:** Four different strain rates between 0.1 mm/min and 1 mm/min (0.1, 0.4, 0.7 and 1 mm/min) were used for the measurements. This measurement gives information about the influence of the strain rate on the sensor characteristics.

- **Thermal Stability:** The thermal stability of the sensor is an essential characteristic of the structural strain sensor. To study the thermal stability, the sensor was heated from the room temperature to an elevated temperature of 70 °C and then cooled down to the room temperature again. This study characterized the electrical conductivity of the sensor with a change in temperature.
- **Cyclic Stability:** The sensor was loaded cyclically for 500 cycles. This study confirmed whether there is a change in the characteristics of the sensor under cyclic loading. The Load range is maintained within the working range of the sensor.

2.4 Results and Discussion

2.4.1 PDD system

2.4.1.1 Monotonic Tensile Test

One of the crucial factors to characterize the sensor is to evaluate the sensitivity of the sensor, which is the gauge factor (GF). In other words, sensitivity helps users to determine how the sensor would respond to the minimum input of a physical parameter. In this study, the normalized resistance change $\left(\frac{\Delta R}{R_0}\right)$ is the output response signal of the sensor when strain is applied, where “ ΔR ” is defined as the resistance change under continuous strain and “ R_0 ” is the resistance without strain. The strain sensing ability is based on piezoresistive principal, which says that the material changes its electrical resistance when it is deformed, and can be used as a sensor element to measure the deformation.

$$\varepsilon_x(1 + 2\mu) + \frac{\partial \rho}{\rho} = \frac{\partial R}{R} \quad (1)$$

The above equation represents the relation between normalized resistance change $\left(\frac{\partial R}{R}\right)$ to an applied strain (ε_x). Which combinedly include the geometric effects $(1 + 2\mu)$ and material properties $\left(\frac{\partial \rho}{\rho}\right)$. This equation was developed for homogeneous conductive material, and didn't include the different conductive network effects of conductive materials, like tunneling effects, available conductive network under strain, so on. However, this equation helps to understand the contribution of geometric effect and material properties change under strain and also to estimate the sensitivity of the current sensor.

Under monotonic tensile loading, the material shows linear agreements between normalized resistance change and strain change. Figure 18 shows that the strain reached 0.63 % before failing, and it can be noted that the sensor can show linearity until failure. A linear fit line

estimates the GF for the mentioned range, and the value is approximately 0.9. This value mostly depends on conductivity of the materials, dispersion of the doped-PANI in to the DVB system, doping level of PANI and crystallization of PANI chain inside the PDD resin system. Even though, this value is lower compared to the carbon nanomaterials (CNMs) filled conductive composites [28], but significant enough to demonstrate the ability of PANI composite as a multifunctional structural strain sensor. This low value of GF compared to CNM filled composites can be explained by two factors. In the case of CNM filled composites, both geometry and percolation networks change to play a significant role of high GF, however, in the case of PANI composite, only geometry change occurs [77]. Even though the GF of the PANI composite is low, it is independent of the effects of percolation networks as in the conductive fillers. As a result, the PANI composite's resistance change under strain follows a more straightforward mechanism than CNM filled composites. It has also been reported in our previous work that PANI-based composite shows a metal like AC electrical conductivity up to a very high-frequency range [78]. Table 1 represents the PANI-based strain sensor's sensibility of different materials. Even though the currents sensor's (DBSA-DVB/16.75 PANI) gauge factor lower than other materials, but the material properties show that it can be used as a structural sensor, reinforced with or without fibers.

Table 1: Polymer-based conductive composites: Mechanical and piezoresistive properties.

Materials	Maximum Strain %	Sensitivity (GF)	References
SBR/ 20 %CB	-	2.9	[31]
SBR/ 7.5 %CNT	-	6.1	[31]
SEBS/ 30 %PANI	10	1.5-2.4	[74]
SBS/ 30 %PANI	60	1	[75]
DBSA-DVB/ 16.7 %PANI	1	0.9	Present work

Further, to find the contribution of geometric effect and material property effect on the sensor under stain, and found that a negative material property effect reduces the GF value by 50 %, considering the poisson's ratio of 0.36 and electrical conductivity 23 S/m. The material property involved the bulk conductivity of the material. The total conductivity of a conducting polymer depends on both the ability to transport charge carriers along the polymer backbone and the ability of carriers to hop between polymer chains through inter polymer conduction (ref. Figure 18). From the resistivity at a particular point equation ($\sigma = \frac{1}{\rho} = \frac{J}{E}$; E is the magnitude of the electric field, J is the magnitude of the current density), it can be understood that for a constant electric field, conductivity increase with current density. In case of PANI chain, electrons jump

from the valence band to the conduction band, due to external strain energy and, as a result, electrons density increases. However, inter PANI chain also increase under tension. So, the resultant of these two effects represent the material property effects on the specimen's GF.

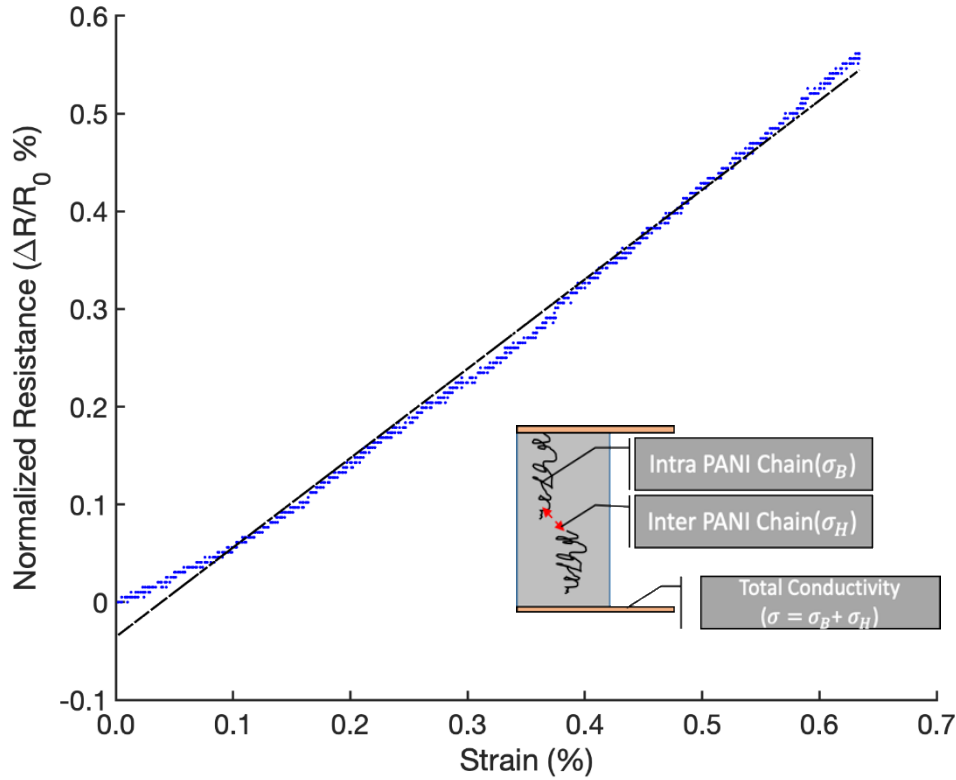


Figure 18: Relative resistance change plotted against the applied strain of the multifunctional PANI-based thermoset polymer. A linear fit line is used to estimate the gauge factor of the sensor.

2.4.1.2 Varied Strain Study

Different ranges have been studied to confirm the synchronicity, reversibility, and stability of the sensor. In the following study, it is called as low strain, when the strain level is below 0.1 mm elongation and high strain when it is more than 0.1 mm elongation. In both cases, samples are strained cyclically to study the linearity, stability, and reversibility of the working range. Figure 19 represents the resistance change of the sensor under different strained levels. The sensor maintained the linearity up to 0.4 mm of elongation, and later it starts showing nonlinearity. Moreover, it becomes severely nonlinear before failing. A similar study was conducted at a low strain range to check the sensitivity of the sensor. Figure 20, shows that the sensor can perform its function even at a low elongation of 0.03 mm. After each cycle, the sensor can regain its initial resistance, which therefore confirms the stability of the sensor. Further, it traces back the same path in loading and unloading conditions, thereby confirming

the reversibility of the sensor. Hence, the sensor can maintain the linearity, stability, reversibility from 0.03 mm to the 0.4 mm of elongation.

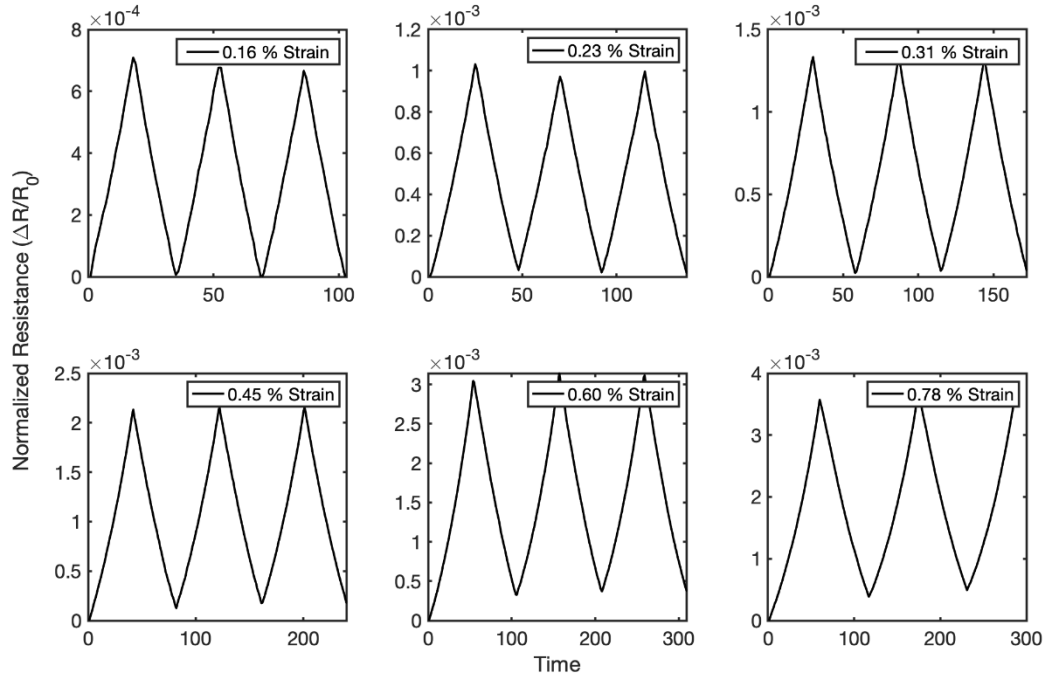


Figure 19: Resistance sensitivity ($\frac{\Delta R}{R_0}$) response at different elongation levels [high strain] plotted for time. The linear behavior of the resistance sensitivity response changes to nonlinearity as elongation level increases after 0.4 mm elongation. Finally, the sample failed at 1mm elongation.

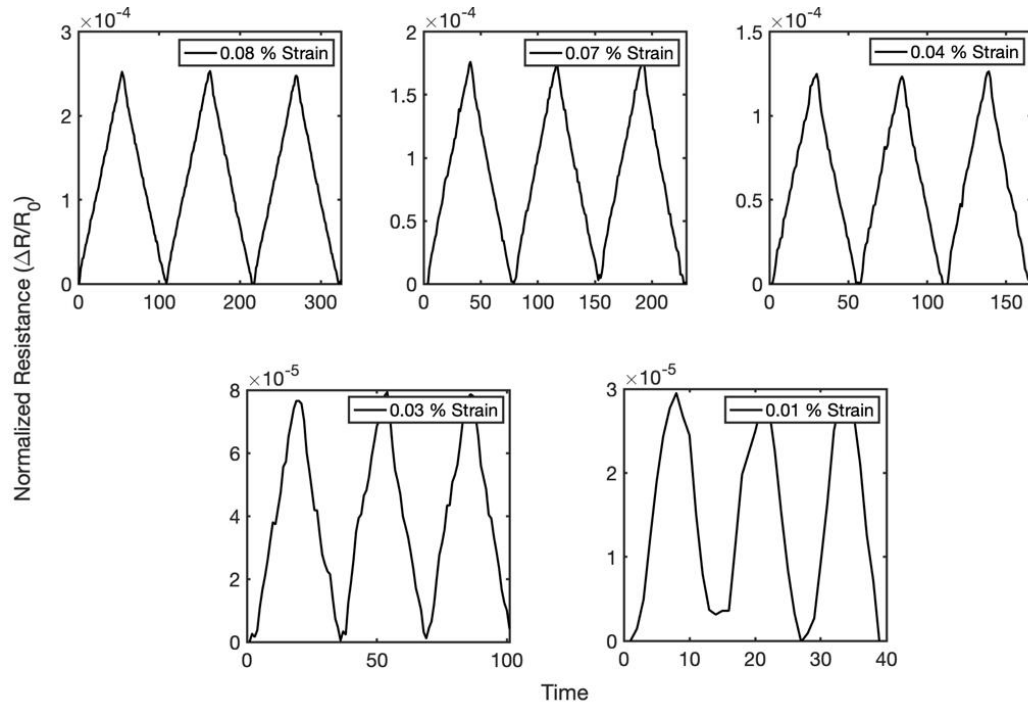


Figure 20: Resistance sensitivity ($\frac{\Delta R}{R_0}$) response at different elongation levels [low strain] plotted for time. The linear behavior of the resistance sensitivity response changes to nonlinearity as elongation level decreases to 0.03 mm elongation.

2.4.1.3 Increasing - Decreasing Load Level

In this study, two sets of tests were conducted where the load is gradually increased and decreased. In Figure 21 (a), the sensor was first stretched up to 50 N, after that load was steadily increased stepwise with a magnitude of 50 N for four steps (i.e., 50 N, 100 N, 150 N, 200 N). Whereas in Figure 21 (b), the strain was applied reversibly (i.e., 200 N, 150 N, 100 N, 50 N). From the figure, it can be summarized that in both cases, the characteristic sensor slope remains the same. However, in case of increasing applied load (Figure 21 (a)), the sensor was not able to reach its initial resistance after unloading. A small amount of residual resistance is visible after each unloading. This phenomenon was not noticed when the sensor was first stretched to its maximum working range, and then the load was gradually decreased. Therefore, the sensor needs to be stretched to its full working range before application to eliminate the residual resistance effect [77].

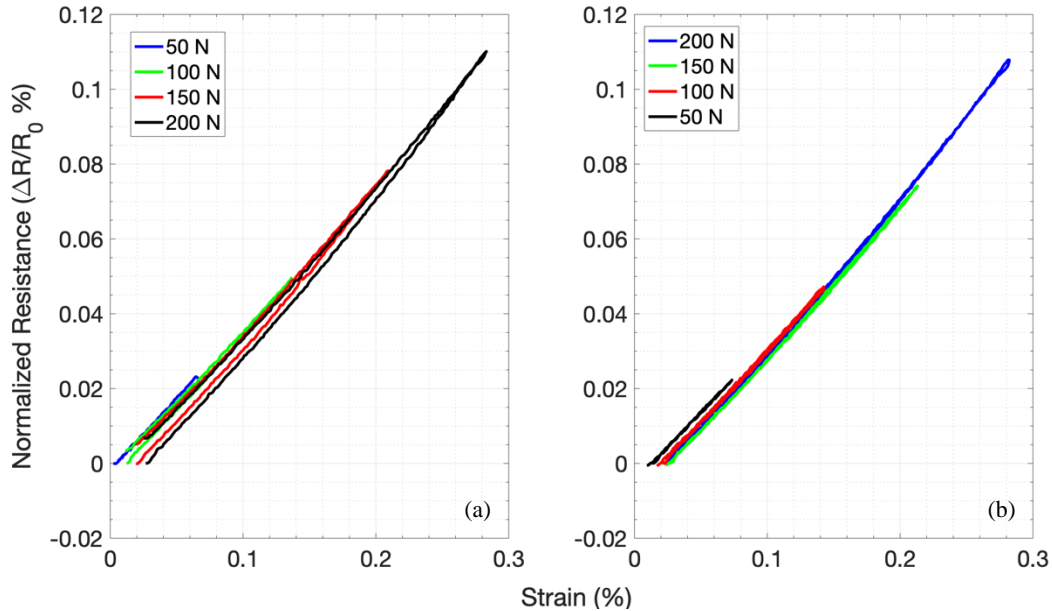


Figure 21: Sensor response when strain increases and decreases stepwise after each cycle. (a) The sensor was loaded from 50 N to 200 N (b) load was decreased from 200 N to 50 N

2.4.1.4 Load - Hold – Unload

Under the load - hold – unload study, samples were loaded cyclically between 0 to 120 N (0.2 % of strain) at two different strain rates of 1 mm/min and 0.1 mm/min. The holding times at the minimum and the maximum strain was 2 minutes. Figure 22 and Figure 23 show the resistance versus time plots of the first cycle at a different strain rate of 1 mm/min and 0.1 mm/min, respectively. The creep of the sensor is remarkably low for both the strain rates. The creep error calculated from the plot is 15.6 % for 1 mm/min and is almost zero for the strain rate of 0.1 mm/min.

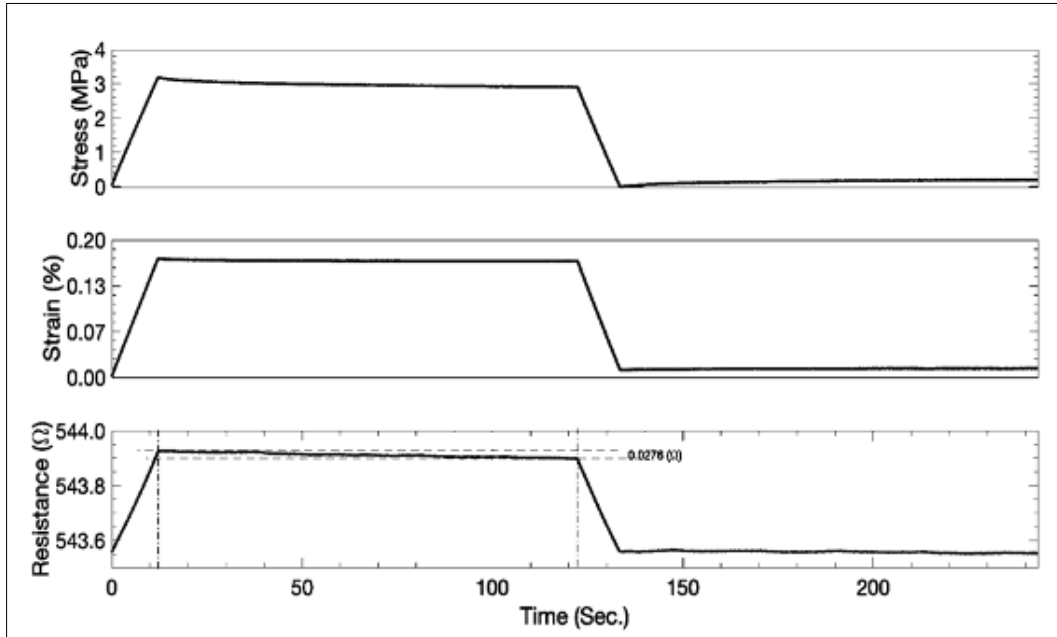


Figure 22: Response of the sensor held at 0.2 % strain for 120 seconds. The strain rate is 1 mm/min, and the creep error calculated is 0.007%.

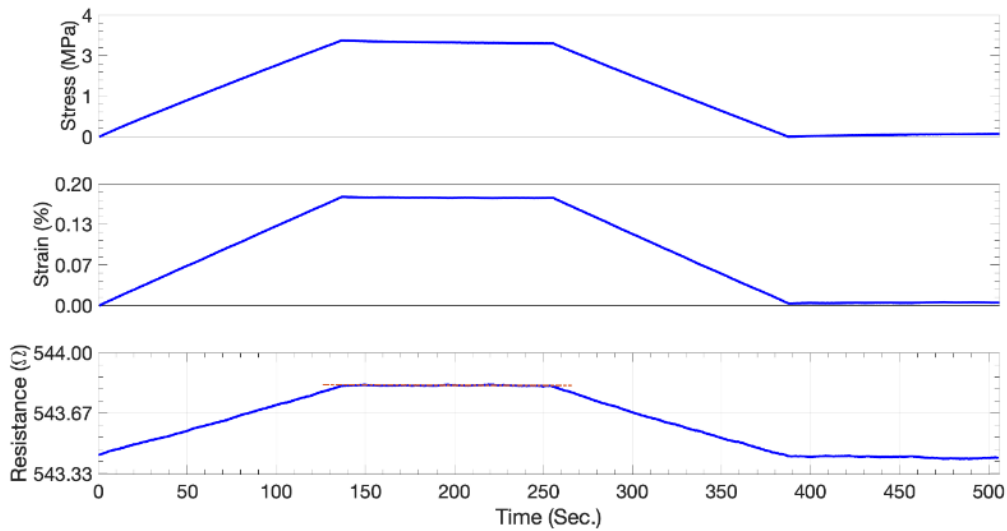


Figure 23: Response of the sensor when it holds for 120 sec at a given strain, and the strain rate is 0.1 mm/min.

2.4.1.5 Varying Strain Rate

The response of the sensor at different strain rates is shown in Figure 24. The strain rate was increased from 0.1 mm/min to 1 mm/min (0.1, 0.4, 0.7 and 1 mm/min). There are no significant changes in the response of the sensor. However, at the lowest strain rate (0.1 mm/min), the sensor exhibits residual resistance after each cycle.

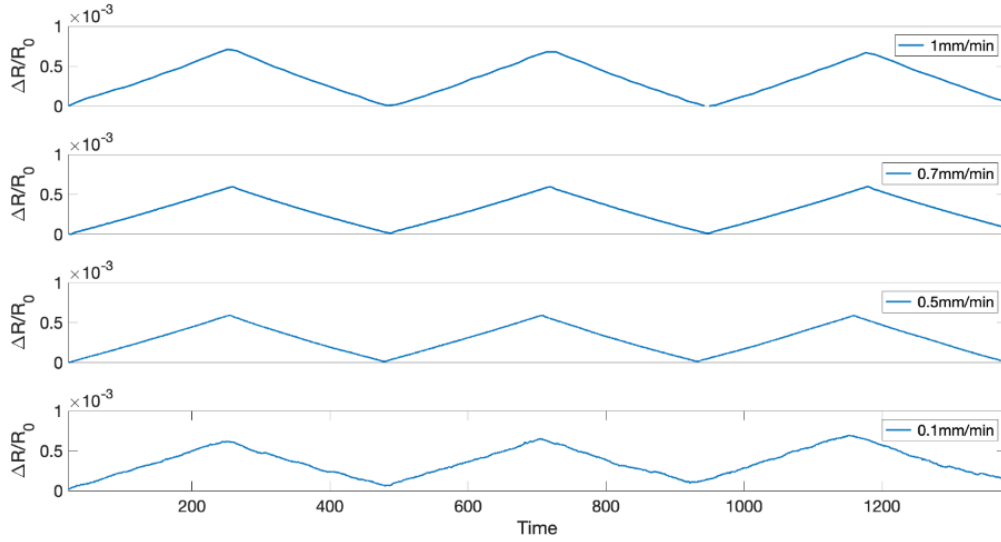


Figure 24: Sensor response at different strain rates (1, 0.7, 0.4, 0.1 mm/min).

In this section, the effect of the hysteresis on the sensor's response was studied within and outside of the working range. A system with hysteresis is defined as a system whose output does not only depend on the current input but also the history of the input [77]. Figure 25 and Figure 26 represent the hysteresis effects of the sensor within the working range, i.e., 0.2% strain at two different strain rates (1 mm/min and 0.1 mm/min), respectively. It was estimated that the maximum hysteresis error is $\pm 0.0045\%$ (0.009 %) in a strain of 0.2 %. Whereas Figure 27 and Figure 28 represent the hysteresis effects of the response outside the working range. A strain of approx. 0.4 % was applied at two different strain rates of 1 mm/min and 0.1 mm/min, respectively. It is found that the maximum hysteresis error was increased to 0.035 %, i.e., almost ten times. Hence, the defined working range will give relatively accurate results

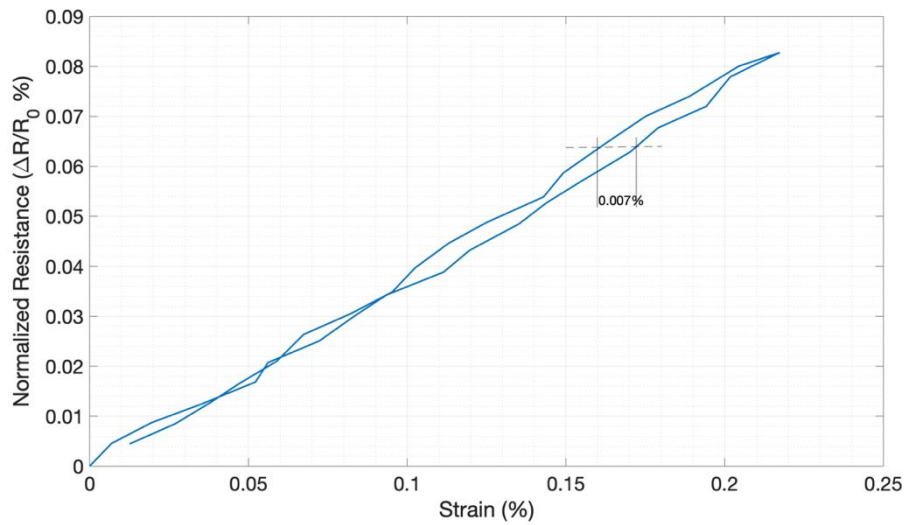


Figure 25: Hysteresis effects of the sensor within the working range, i.e., 0.22% strain and loaded at a strain rate of 1 mm/min.

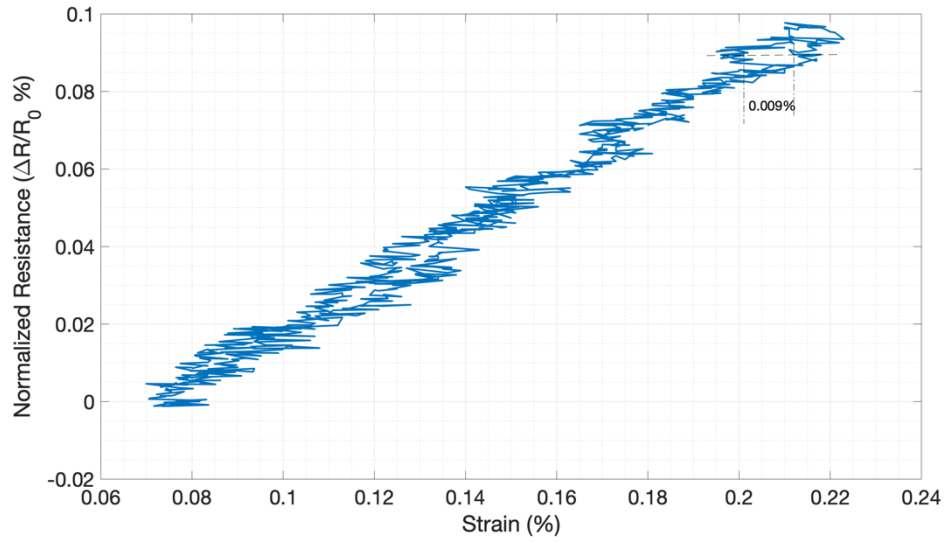


Figure 26: Hysteresis effects of the sensor within the working range, i.e., 0.22% strain and loaded at a strain rate of 0.1 mm/min.

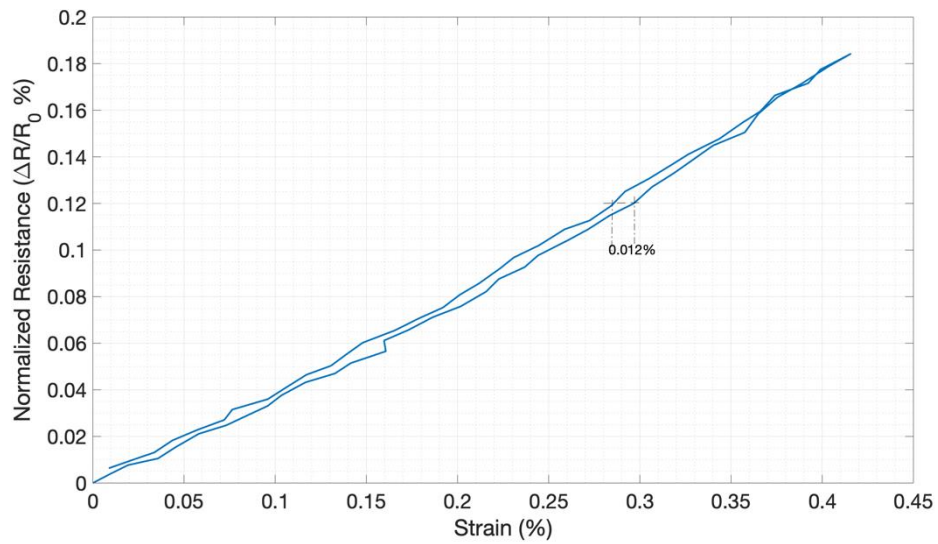


Figure 27: Hysteresis effects of the sensor outside the working range, i.e., 0.42% strain and loaded at a strain rate of 1 mm/min.

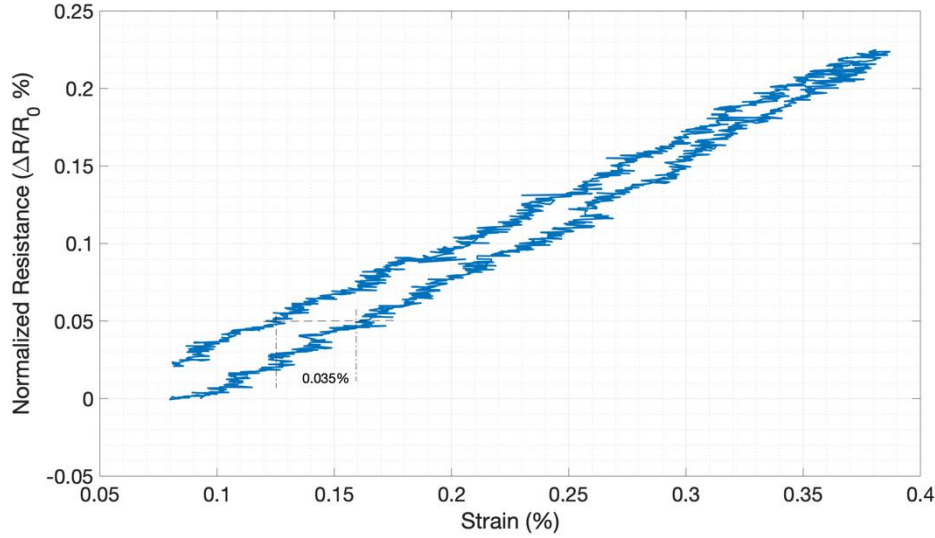


Figure 28: Hysteresis effects of the sensor outside the working range, i.e., 0.42% strain and loaded at a strain rate of 0.1 mm/min.

2.4.1.6 Thermal Stability

To evaluate the thermal stability of the sensor, it was heated from the room temperature (18°C) to 70 °C at a heating rate of 10 °C/min and then cooled down to room temperature again. The response of the sensor under thermal loading is shown in Figure 29. This trend of the conductivity change can be compared with the work of L. Horta-Romaris et al. [76]. It is found that conductivity improved with the increase in temperature similarly to their PANI-DBSA based material. It is reported in the literature that the thermal stability of the electrical conductivity strongly depends on the moisture contained, the chemical nature of the dopants, and the crystal structure [33]. However, large size organic dopants such as DBSA are not easily removed from the polymer matrix below 250 °C. Therefore, the dopant evaporation and degradation are not the main reason for the conductivity change. It is also reported that there is not any change in PANI and DBSA characteristics bonds after thermal treatment, from the FTIR study [33].

In the present study, the sensor was heated up to 70 °C, and the response can be explained by the mobility of the electrons within the studied temperature range. The rise in temperature increases the mobility of electrons in the PANI chain and vice versa. Even though there is a small rise in the conductivity with increase in temperature, the resistance recovers (after cooling) property of the sensor makes it suitable for strain sensing application. A hysteresis was noticed in the Figure 29. However, a possible reason which can be influence is the test setup. The thermocouples were attached at the top and the bottom surface of the specimens, which is also the source of heating and cooling, i.e. heating and cooling was done through top

and bottom surfaces of the specimens. The heating rate was 8 C/min heating rate while the the cooling rate was 26 C/min and 3C/min for 70 C ~ 40 C and 40 C ~ 19 C respectively. It is important to highlight that, even though the surface temperature decrease from 70C to 43 C in less than a minute but the internal heat in the specimen remain constant and decrease gradually after 43C. As a result, the bulk normalized resistance initially didn't effects initial temperature drop (approximately 20 C), then gradually follow the linear increase path with decrease in temperature.

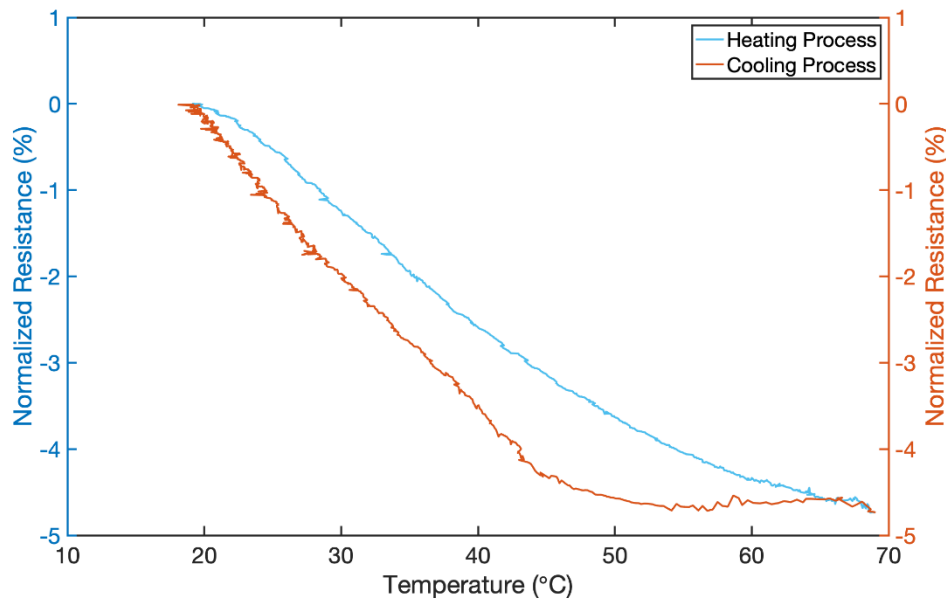


Figure 29: Temperature dependence of the DC electrical conductivity between 18 and 70 °C.

2.4.1.7 Cyclic Stability

To evaluate and compare the reliability of the sensor, long-term cyclic loading was studied. Five hundred cycles of tension loading and unloading up to 120 N (0.22 % strain at a cyclic frequency of 0.1 Hz) were studied, which confirmed the reliability, repeatability, and stability of the sensor properties at a long-run. Figure 30 and Figure 31 represent the ten cycles (first and last) and complete response of 500 cycles, respectively. It has been noticed that there is a small baseline shift of the resistance sensitivity change response of the sensor at the initial cycles then saturated. This small baseline shift could be because of the elastic property of the DVB. That is the rearrange of the DVB polymer chain in the loading direction helps to improve the PANI network and the conductivity of PDD system. Similar behavior also can notice in case of creep test. The rise in temperature during the cyclic load could be another possible reason. It has also been observed that the initial resistance of the sensor (completely unloaded) was almost recovered after finishing 500 cycles.

Further analysis indicated that the average sensor sensitivities of the first and last ten cycles are almost the same. These results show a high level of synchronization and stability of the sensor under long cyclic (500 cycles) loading. A similar response of flexible thermoplastic-based PANI composite under cyclic loading was reported [74,75,79]; however, the current research is based on a thermoset-based structural sensor.

In any case, it can be concluded that the developed PANI/DBSA/DVB composites showed excellent properties for structural strain sensing applications at low strain measurement. The characterized responses are similar to the composites based on the thermosetting and thermoplastic polymer with conductive fillers, including PANI. Highlighting that, electrically conductive PANI composite is highly suitable for the development of structural strain sensors.

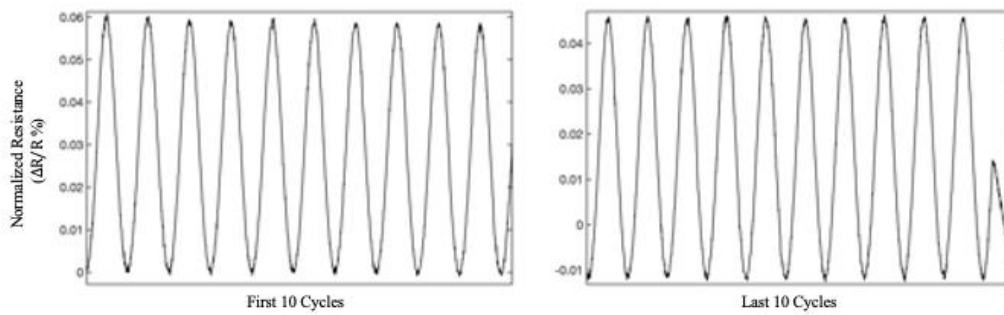


Figure 30: Cyclic load stability test results of the sensor subjected to 500 cycles at a frequency of 1 Hz up to a strain value of 0.22 %. The above plot represents the first and last ten cycles of the test.

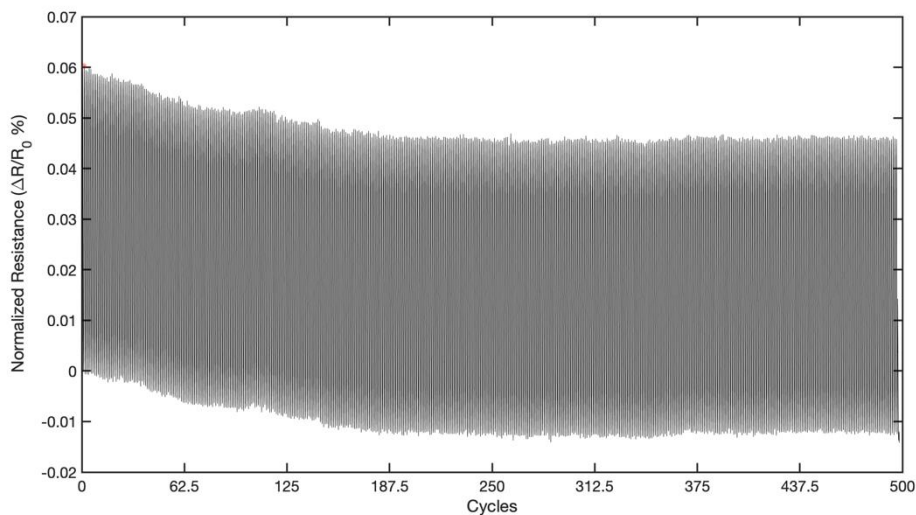


Figure 31: Cyclic load stability test results of the sensor subjected to 500 cycles at a frequency of 1 Hz up to a strain value of 0.22%.

2.4.2 Glass Fiber Reinforced Conductive Polymer (GFRCP) Composites

Once the resin was characterized for a strain sensor, a similar study was conducted for both glass fiber reinforced conductive (PDD system) polymer composites and PDD layer on GFRP composites. Every characterization parameter was discussed below.

2.4.2.1 Sensitivity

The first investigation was whether the PANI-based conductive glass fiber composites could show similar piezoresistive effects as other piezoresistive materials do. The basic principle of the piezoresistive material is that it changes its' electrical resistance when it is deformed. Three separate effects that contribute to the electrical resistance change in the piezoresistive materials, i.e., the applied strain change the length of the materials, also change the cross-section of the materials, and the resistivity of the materials, which consider as constant in our study [80]. Simultaneous measurement of GFRCP composites' resistance, strain, and stress change during monotonic loading at a rate of 1 mm/min was recorded. It was found that the normalized resistance change (NRC), i.e. $\left(\Delta R/R_0\right)$ of the GFRCP composite increases linearly with an increase of tensile strain. This phenomenon can be correlated to empirically as described in **Eq. (1)** [81],

$$\varepsilon = \frac{1}{GF} \frac{\Delta R}{R_0} + \varepsilon_0 \quad (2)$$

Where R_0 , the reference resistance before applied load; $\Delta R = R - R_0$ is the resistance change due to load and ε_0 refers to the initial strain for the piezoresistivity effect. Gauge factor (GF) is the strain sensitivity factor of the sensor.

The GF value of 1.5 was estimated with linear regression analysis from Figure 32. The linearity of the stain versus NRC curve maintains up to 0.2 % strain with an NRC value of 0.5. Once material cross this first linear zone, an apparent rise in GF's slope observed. This slop change can be attributed to the micro-damage propagation, which raises the overall volumetric resistance of materials. This second slop can be a further study for damage detection. It is also observed that GF value has been improved compared to the pure conductive matrix material, i.e., 0.9 [82]. The possible reason could be micro-damage initiation and piezoresistive effects. Under the applied load, the piezoresistive material's band structure gets affected, and as a result, it changes its resistivity [80].

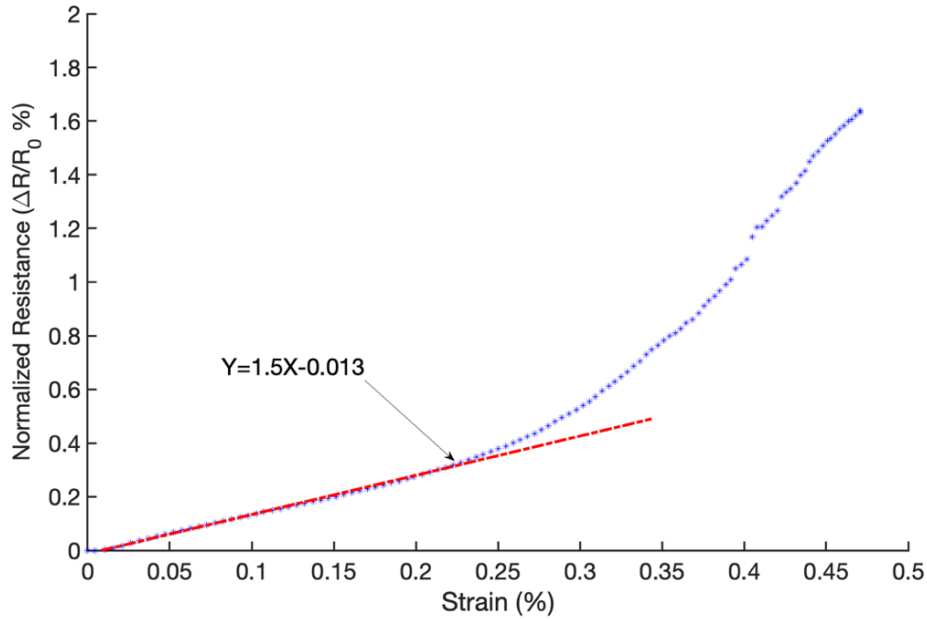


Figure 32: Response of normalized resistance change to strain under monotonic tensile test.

On the other hand, the behavior of woven fabric GFRCP under quasi-static tensile loading also influence the rise in GF value. The micro-cracks initiation near waving points, matrix-fiber debonding, and matrix cracking in transverse yarns reduce the available conductive networks [83]. As a result, the overall resistance change increase in the specimen. Even though the GF value is close to convention metal foil strain gauge, however, the foil strain gauge can only measure strain at a particular location and direction. Whereas, self-sensing GFRCP composite represents the global volumetric resistance change due to the geometrical changes and can be used in all directions. Compared with nanofillers technology, their resistance change occurred not only because of the stress-dependent resistivity of the nano-fillers but also because of conductive networks, interspace, and contact area of the fillers.

A similar result of GF 1.3 has been reported by Shang-lin et al. [81]. In their work, multiwalled carbon nanotube (MWNT) was used to make conductive glass fiber composite to measure the strain and damages. The possible resistance change mechanism was reported that the stress-dependency of the nanotube structure, which affects the nanotube network geometry, interspace, contact area, and density. Whereas, current research can report improved and stable gauge factor. It is also important to note that both PANI-based and nano-filler based composite have their advantages and limitations. The PANI-based GFRCP composite is having a prime advantage that it not only can act as a self-sensing structure, but also its' high conductivity and mechanical properties can be utilized in other functionality, like LSP [50], and EMI shielding

[84,85]. Table 2 represents both the mechanical and electrical properties of this structural material.

Table 2: Electrical and Mechanical Properties of the GFRCP composites.

Properties	<i>Stiffness</i> (GPa)	<i>Passion</i> <i>Ratio</i> (μ)	<i>Electrical Conductivity</i> (S/cm)
GFRCP Composites	11.4	0.08	0.11

2.4.2.2 Working Range

Figure 33 shows the implementation of three repeating tensile loading trails of the specimens that led to piezoresistive characteristics. A linear and synchronized increase and decrease of the electrical resistance arise from loading and unloading of the load. Numerous studies have been carried out to characterize the piezoresistive effect of conductive FRP composites mixed with different nano-fillers [28,86–88]. For instance, wang et al. [88], studied the basalt fiber reinforced polymer laminates fabricated with carbon nanofibers (CNFs/BFRP) and reported similar responses under constant amplitude cyclic loading within the elastic region. However, they reported the small nonlinear behavior had been noticed at the beginning and the end of each loading cycle. It implies that those self-sensing structures are not sensible for low strain, whereas current research data confirmed the sensibility even at low strain.

An increasing strain level study was carried out to estimate the working range of the self-sensing GFRCP composite. Two parameters were considered to estimate the working range; first, NRC has to be approximately zero after releasing the load, and second, only a linear response zone will be considered during loading. These assumptions confirmed that there is no damage to the sensor during its functionality. For this study, specimens were loaded from 0.07 % strain for three consequence cycles at 1 mm/min. After each step, the strain level was increased by 0.06 % until apparent nonlinear and permanent resistance change occurred.

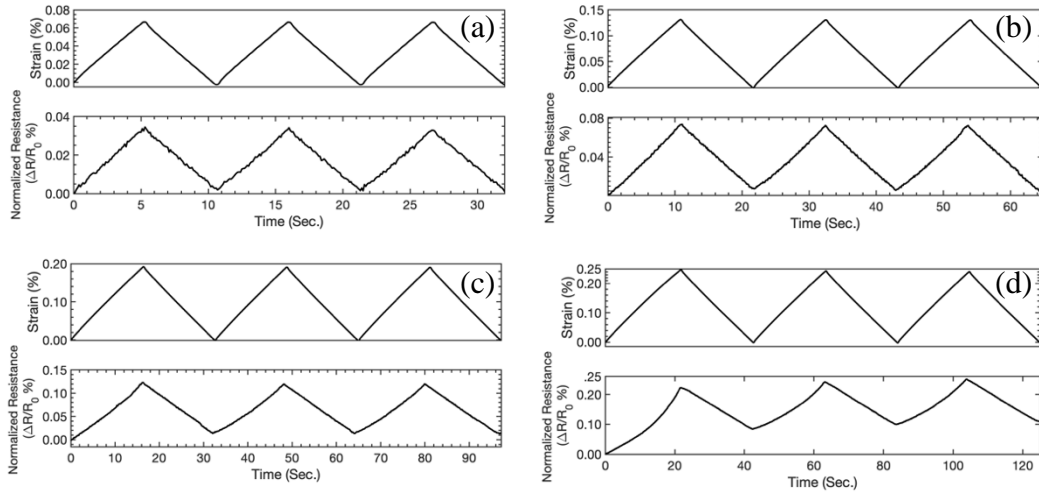


Figure 33: Strain monitoring of GFRCP composite under constant amplitude cyclic tensile loading. (a) NRC, Strain vs time for 0.07 % strain, (b) NRC, Strain vs time for 0.13 % strain, (c) NRC, Strain vs time for 0.19 % strain, (d) NRC, Strain vs time for 0.25 % strain.

It is observed that the values of the NRC steadily increased with the increasing strains and then gradually decreased during unloading. It has been confirmed from Figure 33 that, after 0.2 % of strain, the NRC was nonlinear and unable to regain its initial resistance after unloading. These nonlinear responses can be attributed to a permanent change in the conductive network in the specimens and micro-damages in matrix and fiber-matrix interferences [81]. Whereas linear strain self-sensing responses are based on the piezoresistive principle.

It can be summarized from the above study that the working range of self-sensing CFRCP composite can be approximate up to 0.2 % strain.

2.4.2.3 Creep Study

For the design of the composite components, creep is one of the crucial studies [89]. Such analysis becomes difficult when introduced with plain-woven laminates as they have considerably complex internal structures comprised of fiber bundles and matrix materials, and these materials have entirely different creep properties [90]. The degree of creep depends on several factors, such as type of polymers, the magnitude of load, temperature, and time [91].

In this study, a creep test was performed by using the same experimental setup and specimens. The specimens were ramped to 500 N (17 MPa) at a rate of 1 mm/min and held for 120 sec. To confirm the complete recoverability, specimens were kept another 120 sec after unloading. Figure 34 shows the creep response curve at room temperature. It can be observed from the result that there is no such creep effect notice under the test conditions. The complete recovery of the resistance upon unloading also confirmed that no damages initiation happened during a creep test. However, specimens took a much longer time to recover its initial resistance after

unloading. This response attributed to resistance creep of the material. The molecular motions of the matrix bring about the local rearrangement of the conductive networks, leading to the resistance creep [92]. This study confirmed the self-sensing ability of GFRCP composite even after short creep loading.

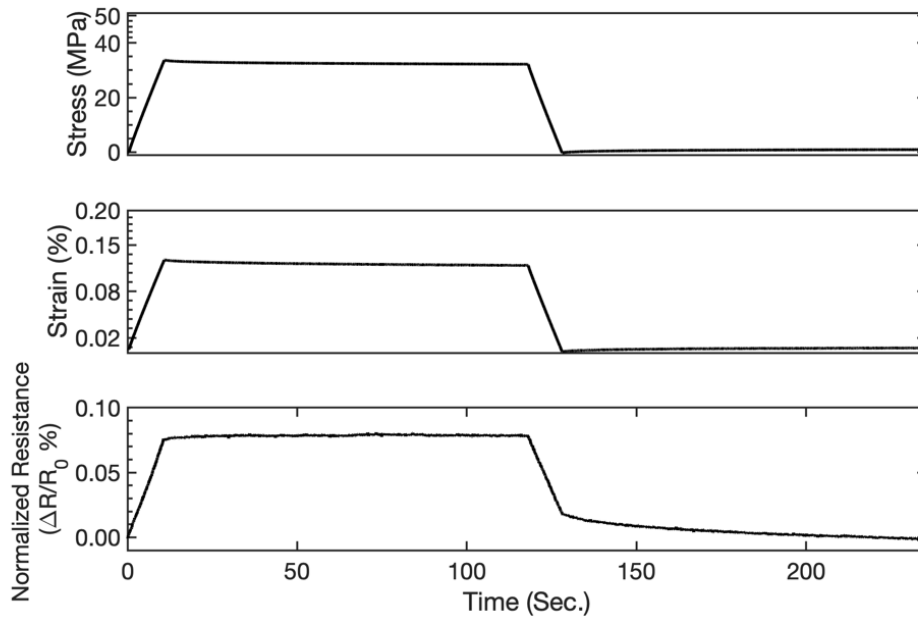


Figure 34: The creep response curve of GFRCP composite at room temperature, which includes the strain and normalized resistance change.

2.4.2.4 Thermal Stability

In this study, volumetric resistance (longitudinal) change of GFRCP laminates was measured around 25 - 70 °C. The temperature of the specimen was measured using two thermocouples attached to both the top and bottom surfaces of the specimens. The specimen was kept in hot-press under zero pressure, and heated at a rate of 10 °C/min then cooled down to initial temperature.

The electrical resistance measurement with elevated temperature is shown in Figure 35. A strong correlation between the volumetric resistance and temperature was observed. It is found that the longitudinal resistance increases as temperature increases. This characteristic could be due to thermal expansion, the architecture of plain-woven glass fabric, fiber-matrix interference, micro matrix crack opening, and high fiber volume fractions [81]. The thermal expansion of plain-woven glass fibers in longitudinal and lateral direction could reduce the available conductive networks; as a result, the resistance increases with thermal expansion [93]. Other possible reasons would be, the micro matrix cracks and fiber-matrix interference cracks' breathing with the temperature variations.

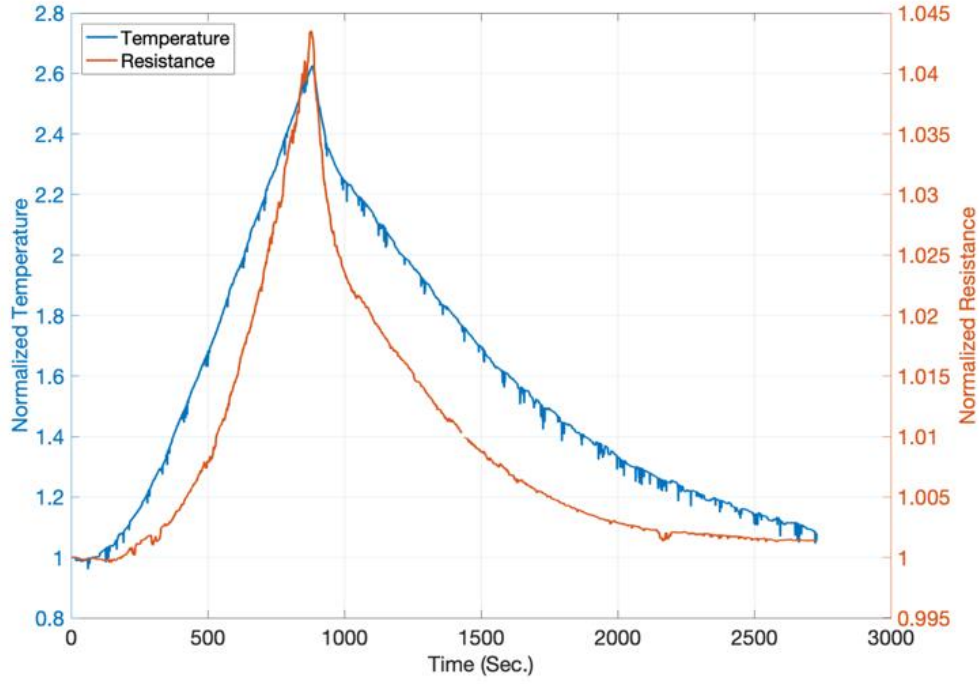


Figure 35: Normalized Electrical resistance change and temperature with time plotted when specimens were heated at a rate of 10 °C /min from 30 °C to 70 °C and cooled back to its initial temperature.

To understand the effect of thermal deformation on NRC, the longitudinal thermal strain is estimated with the help of the coefficient of thermal expansion ($0.6 \times 10^{-4} K^{-1}$ for thermosets). From **Eq. (2)** [94], the thermal strain is calculated as 0.26 % for the given temperature rise. For comparison, NRC corresponds to 0.26 % mechanical strain was also measured from Figure 32.

$$\varepsilon_{thermal} = \alpha \Delta T \quad (3)$$

Comparing the two NRC values, i.e., 0.04 and 0.004, due to thermal strain and equivalent mechanical strain respectively, it is understood that the thermal strain contributes only 10 % of total NRC in the thermal study. This confirmed that the influence of thermal expansion on resistance change due to elevated temperature is less.

Further, the temperature coefficient of resistance for GFRCP is estimated from the slope of Figure 36. This can also be calculated from **Eq. (3)**.

$$\alpha \Delta T = \frac{\Delta \rho}{\rho_0} = \frac{\Delta R}{R_0} \quad (4)$$

Two significant slope changes occurred, first at 30 ~ 50 °C and second of 50 ~ 71 °C. The values of these slopes are given in Table 3. The positive value of the temperature coefficient of the

resistance represents the rise in resistance with temperature. Even though pure PANI based conductive resin showed a negative coefficient of resistance [82], but in the presence of glass fiber reinforcement, and its architecture, the laminates become a negative coefficient of resistance.

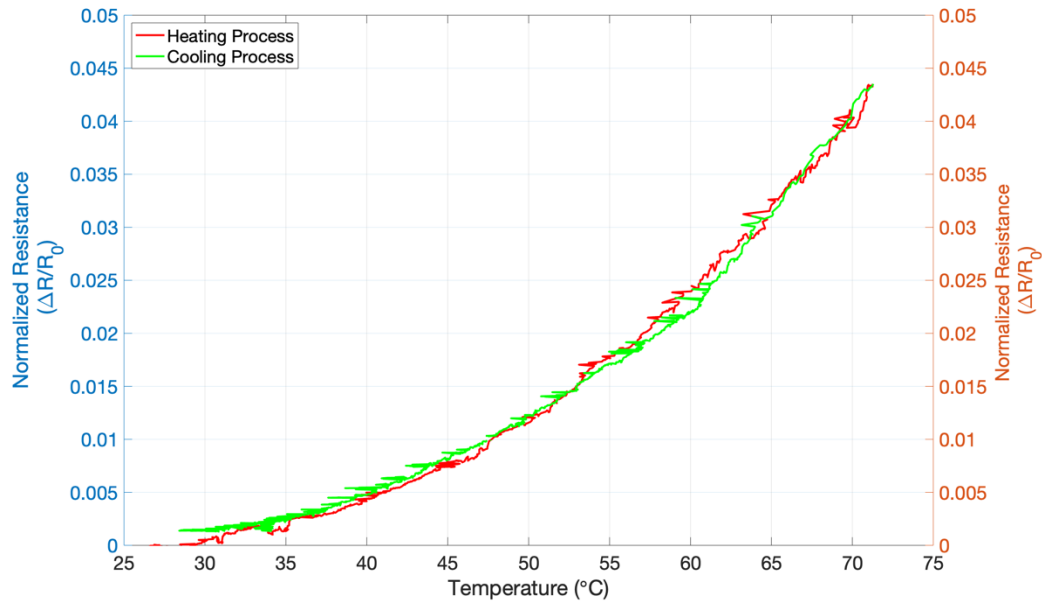


Figure 36: Normalized resistance change w.r.t. temperature change plotted to evaluate the temperature coefficient of resistance of GFRCP composite.

Table 3: Measured temperature coefficient of resistance

<i>Temperature Range</i>	<i>30 ~ 50 °C</i>	<i>50 ~ 70 °C</i>
Temperature coefficient of resistance($10^{-3} K^{-1}$)	0.55	1.48

2.4.2.5 Nonlinearity Error, Repeatability, and Hysteresis Study

For more understanding of the in-situ strain monitoring of GFRCP composite, the relevant parameter, including nonlinearity error, repeatability, and hysteresis, was investigated. A comparison summary with reference equations and calculated values are presented in Table 4. For all these analyses, specimens were loaded under constant amplitude cyclic tensile loading [95]. The nonlinearity error indicates the error percentage of the linearity, i.e., how much the linear fit regression line deviated from the strain-NRC curve. To estimate the nonlinearity error, the maximum deviation between the strain-NRC curve and linear regression line (Δ_{max}) and max NRC range ($f_{F,S}$) was evaluated from Figure 37, i.e., 0.01 and 0.07 respectively. To estimate the repeatability in quantitatively, the maximum repeat difference of NRC for the

same strain level and process during loading or unloading (ΔR_{max}) was evaluated from Figure 38 i.e., 0.00163. Further, using the equation in Table 4, repeatability was evaluated as 2.33 %. Lastly, hysteresis, i.e., how much resistivity of the laminates do not recover its initial values after unloading, was estimated. The maximum difference of NRC in all processes during loading-unloading cyclic (Δf_{max}) was calculated from Figure 38 to estimate the hysteresis. Compare with a similar study done by wang et al., for the GFRP/CNT composites, almost the same result found [52] also confirmed the excellent linearity and repeatability with low hysteresis.

Table 4: Parameters of the in-situ monitoring of GFRCP composite.

<i>Parameters</i>	<i>Ref. Equations</i>	<i>GFRPC</i>	<i>CNT/GFRP</i>	<i>References</i>
<i>Nonlinearity error (%)</i>	$E = \frac{\Delta_{max}}{f_{F.S}} \times 100$	14.29	14.2	
<i>Repeatability (%)</i>	$R = \frac{\Delta R_{max}}{f_{F.S}} \times 100$	2.33	7.9	[95]
<i>Hysteresis (%)</i>	$H = \frac{\Delta f_{max}}{f_{F.S}} \times 100$	9.70	18.5	

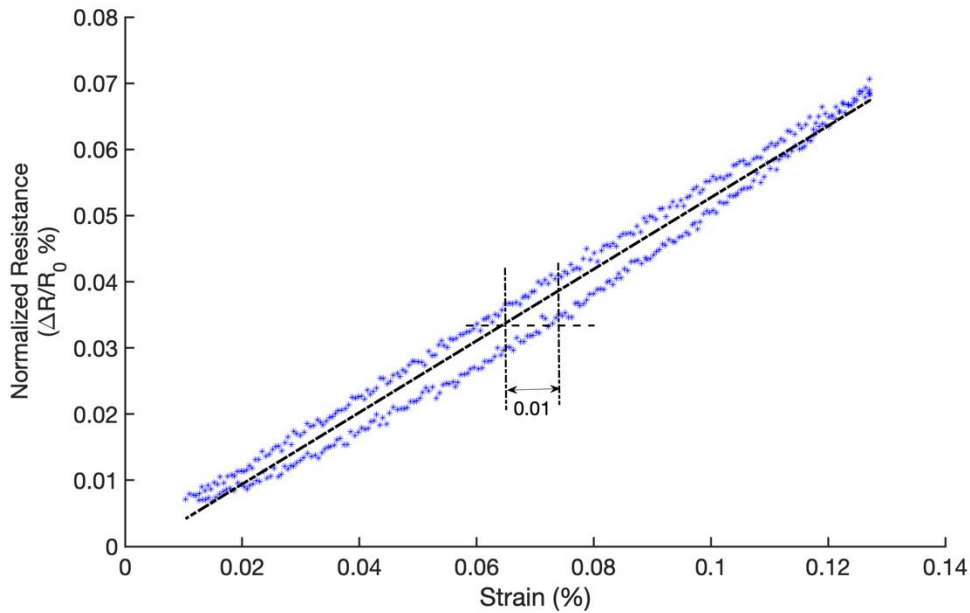


Figure 37: Strain versus NRC of GFRCP composite under constant amplitude (0.13 % strain) cyclic tensile loading. A single cycle represents to evaluate the hysteresis (%).

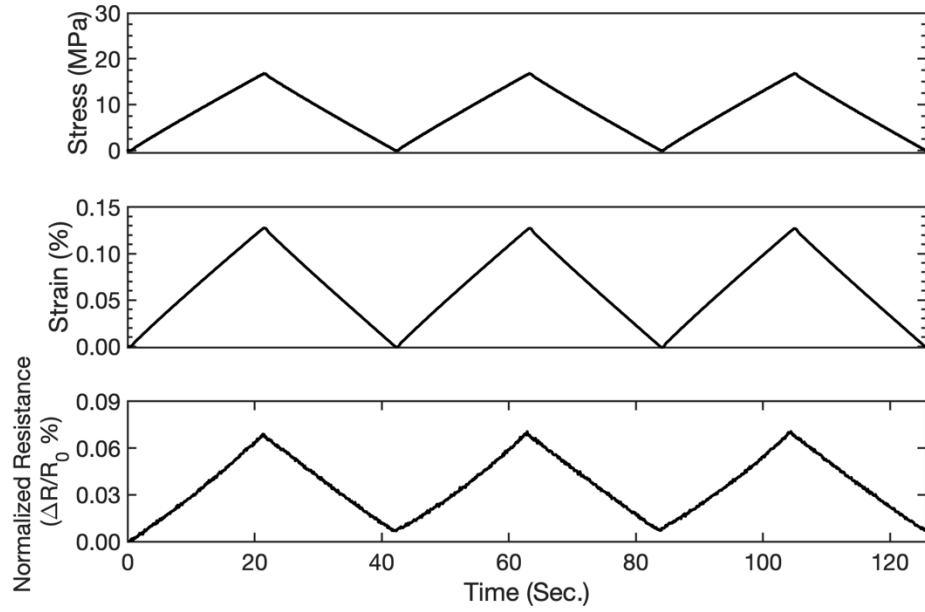


Figure 38: Stress, Strain, and NRC monitoring of GFRCP composite under constant amplitude (0.13 % strain) cyclic tensile loading.

2.4.2.6 Incremental Amplitude Cyclic Tensile Loading

A systematic, incremental amplitude cyclic tensile loading test was performed on the specimens to simulate the actual loading conditions and verify the reproducibility of the self-sensing ability of the GFRCP composite. The amplitude started with 200 N and then increased by 200 N after each cycle up to 1000 N.

It can be observed from Figure 39 that the NRC varied with applied stress. However, residual resistance of the specimens becomes severe after the third cycle. This residual resistance can be correlated with strain energy loss. On the other hand, a reverse (decreasing) way study (Figure 40) has been conducted for comparison. Figure 41 (b) clearly shows that after the first cycle (1000 N amplitude), all other cycles have negligible residual resistance, whereas. Figure 41 (a) highlights much more residual resistance in almost every cycle.

Therefore, to reduce the residual resistance and stability of the conductive networks inside the GFRCP composite, pre-stretch/stress treatment is recommended. Further, this GFRCP composite has the potential to sense the damage initiation in the composite; however, further study may require to claim its ability.

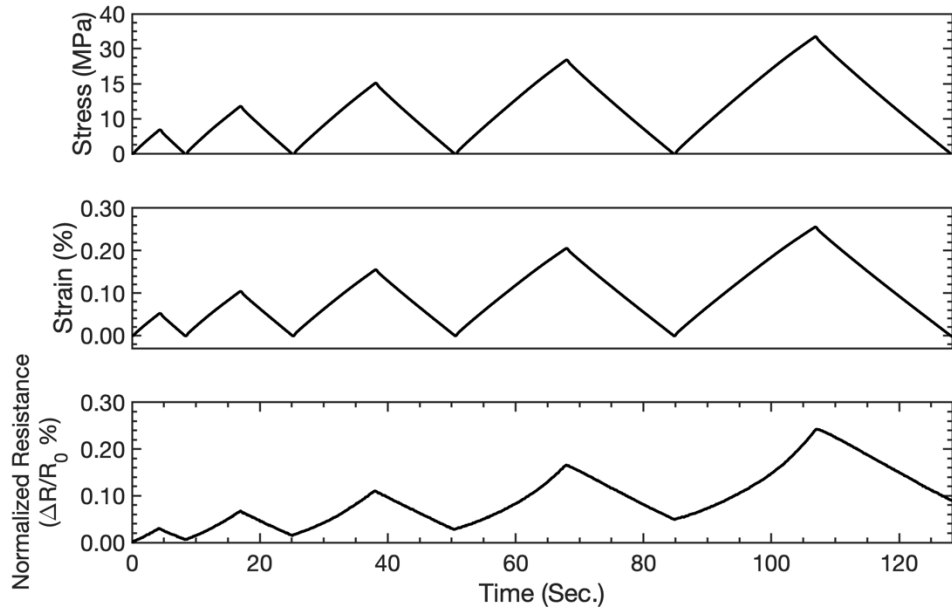


Figure 39: Stress, Strain, and normalized resistance change response of the GFRCP composite under incremental amplitude cyclic tensile loading. The load ranges from 200 N to 1000 N incremented by 200 N after each cycle.

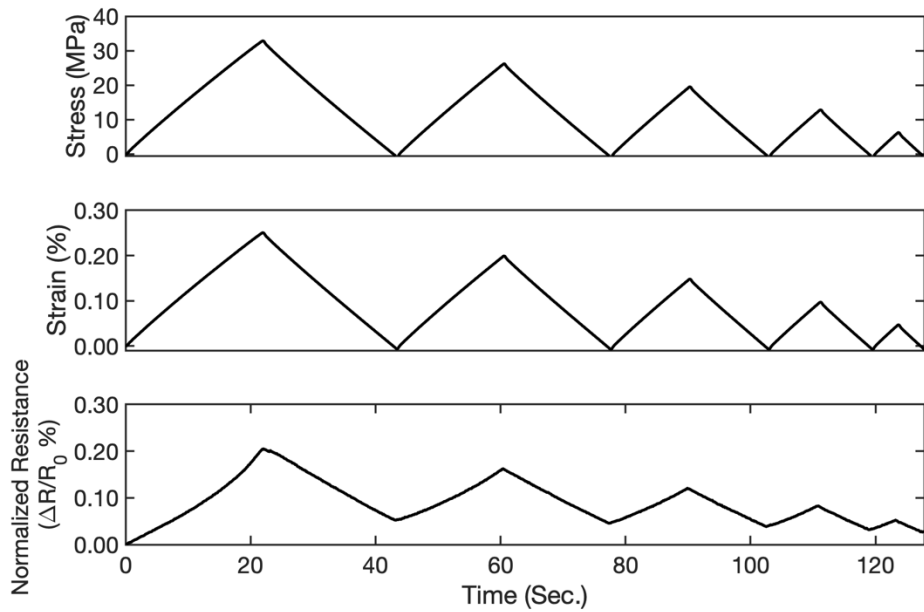


Figure 40: Stress, Strain, and normalized resistance change response of the GFRCP composite under decremental amplitude cyclic tensile loading. The load ranges from 1000 N to 200 N decremented by 200 N after each cycle.

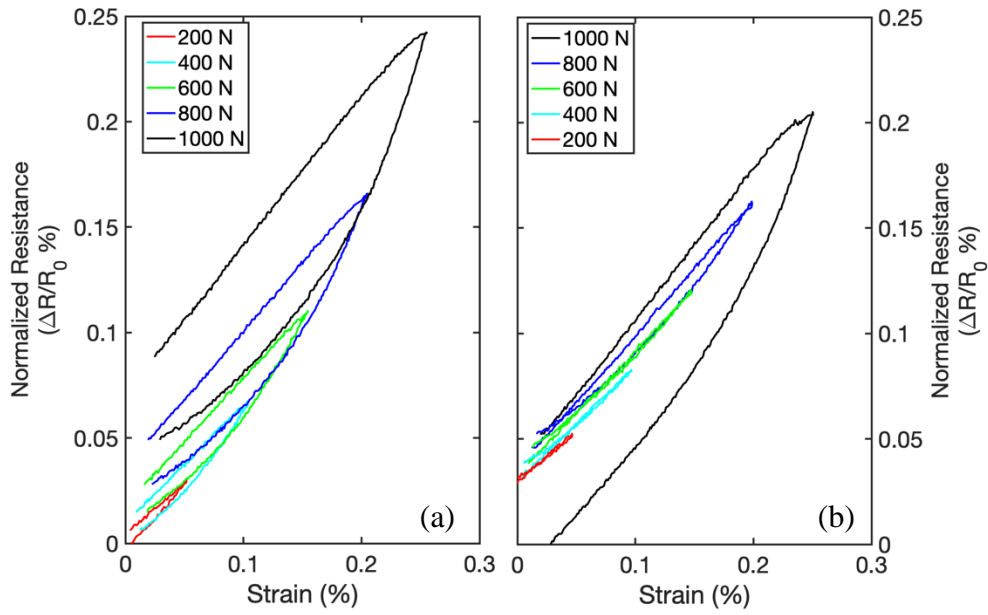


Figure 41: Comparison plot to analyze the residual resistance both in incremental and decremental amplitude cyclic tensile loading.

2.4.3 PDD Conductive Layer on GFRP Composites

2.4.3.1 Monotonic Tensile Test

The calculated gauge factor, i.e., $GF \sim 0.81$ (Figure 42) the same as our previous published result. Even though this value of GF is lesser than metallic strain gauges but significant enough while comparing with various nanofillers CPCs, moreover, this value makes it significant to use this material as an advance multifunctional martial.

2.4.3.2 Increasing – Decreasing load level

Figure 43 and Figure 44 represent the electrical and mechanical responses of the PDD layer on GFRP when loaded at different load levels and sequences, i.e., increase and decrease order, respectively. It is observed that there is no drift in resistance baseline even though loaded up to 1000 N. This was achieved by following the recommendation suggested from the previous work to pre-stretch the specimens before testing.

Unlike the PDD layer on GFRP composite, a non-reversible phenomenon was reported for nano-filler CPCs due to creep, and the electrical response changed accordingly, resulting from the accumulation of chains relaxation and slipping with an increase in deformation amplitude from a cycle to another by keeping strain memory of previous cycles. This phenomenon did not notice in our study. This is because it has already been confirmed in our previous study that the creep error is negligible within the sensor's working range. In other words, the recovery of

the initial resistance of the sensor upon unloading confirmed that there were no damages that occurred in the conductive network. These results also confirmed the reversibility of the sensor.

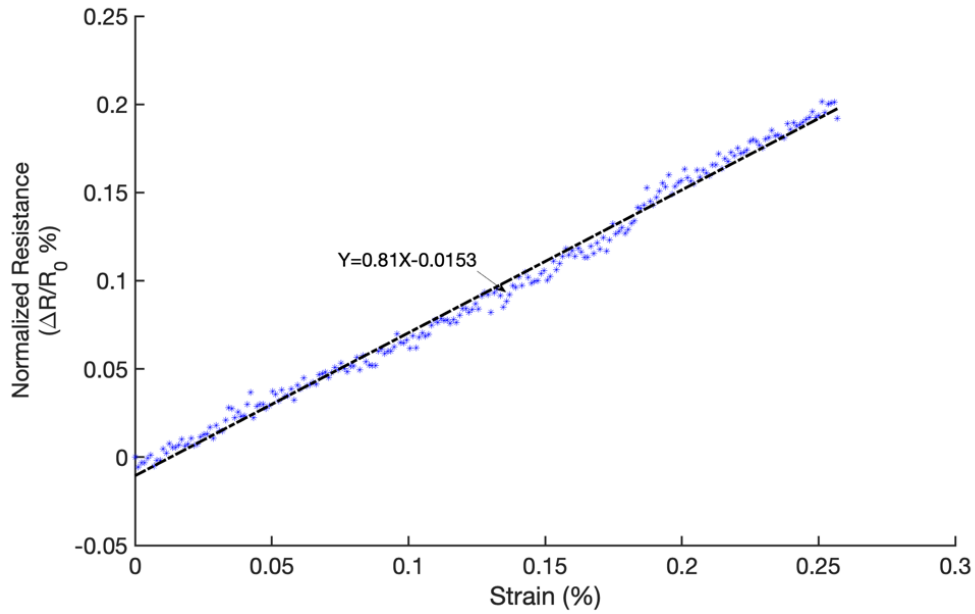


Figure 42: Piezoresistive response of the sensor within the working range under monotonic tensile loading. A linear fit line used to estimate the gauge factor of the sensor, i.e., 0.81.

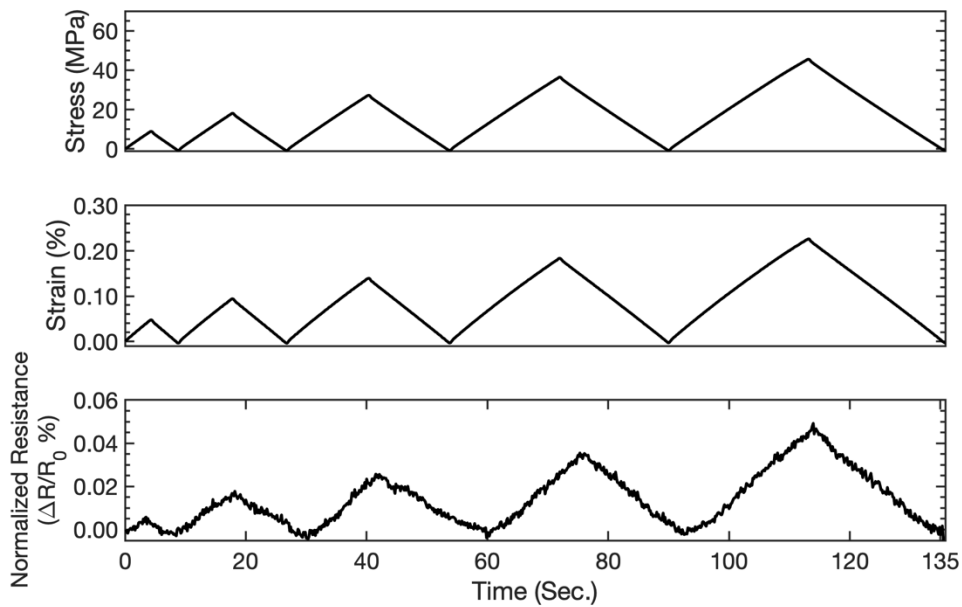


Figure 43: Increasing strain study: PDD layer on GFRP composite subjected to load sweep from 0 to 1000 N by increments of 200N. (a) Stress (b) Strain (c) Resistance sensitivity

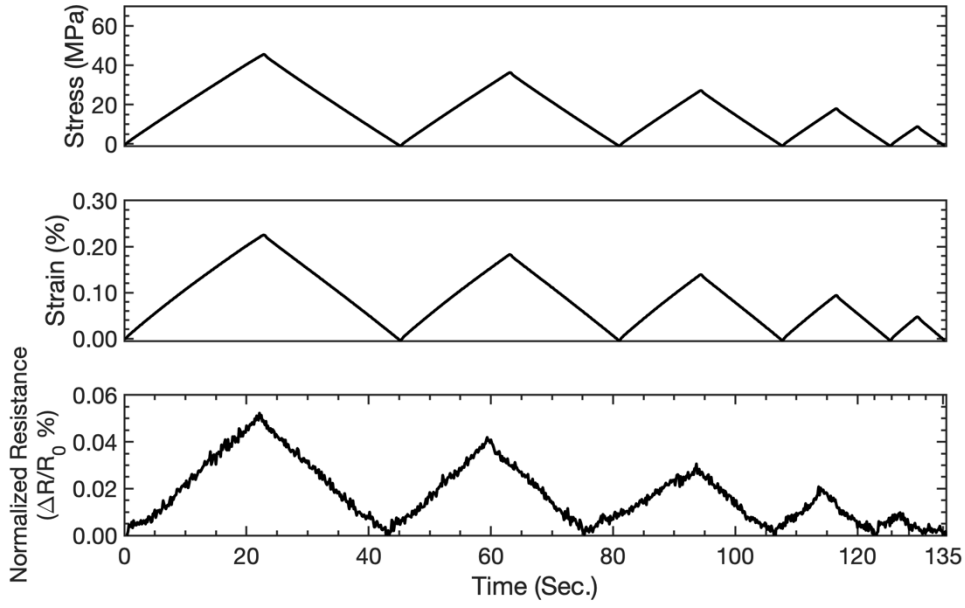


Figure 44: Decreasing strain study: PDD layer on GFRP composite subjected to load sweep from 1000 N by increments of 200N. (a) Stress (b) Strain (c) Resistance sensitivity

Polymers are viscoelastic and exhibit time-dependent relaxations behavior under constant stress or strain. Whereas creep phenomena are the increase in strain with time when it is under constant strain. Therefore, it is important to estimate these errors for the PDD layer sensor. At very high stress/strain or temperature, creep/stress relaxation development is too fast to be qualified. Therefore, the load should be suitably chosen for their studies so that measurements can be made over a significant period. In this study, the specimen was elongated to 0.1 % strain at a rate of 1 mm/min then hold for 120 sec, followed by unloading. This study was done for three subsequent cycles.

Figure 45 represents the creep/relaxation response of the PDD layer sensor on the GFRP composite. It is evident from the figure that, within the working range of the sensor, no significant influence of the creep/relaxation phenomena is noticeable in the mechanical and electrical response. A detailed study of the individual cycle present in Figure 46, which confirms no influence of the creep/relaxation effect on sensor response. This result shows better response compared to previous because the current study fabricated the sensor on the GFRP composite as a layer, whereas the previous study characterized the PDD sensor itself.

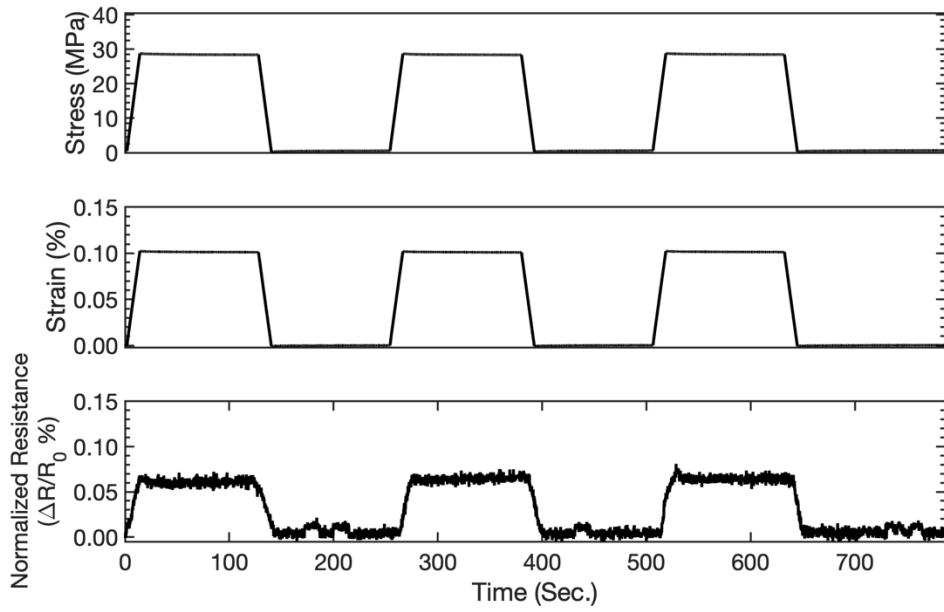


Figure 45: PDD sensor response under creep/stress relaxation study. The specimen was elongated to 0.1 % strain at a rate of 1 mm/min then hold 120 sec. This study was done for three cycles.

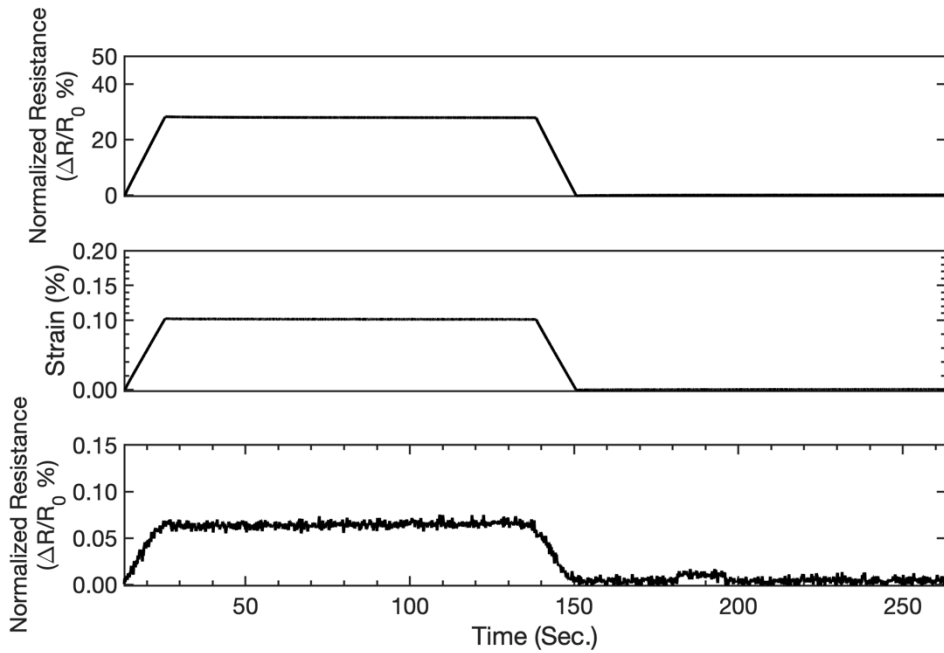


Figure 46: Single cycle representation of Creep/Relaxation study.

2.5 Summary

Introduced a structural strain sensor using a multifunctional PANI based conductive polymer system and thoroughly characterized. The responses of the sensor are promising for low strain measurement applications in a range of 0.025 % to 0.3 % of strain. However, it also can be used for damage detection at the higher strain level. The PANI based strain sensor

characterization can be summarized as follows; Firstly, a monotonic tensile test was conducted to estimate the gauge factor of the sensor as 0.9. Secondly, to estimate the working range of the sensor based on the various strain level study was done. Next, in the increasing – decreasing load study, it was concluded that preloading is necessary to mitigate the residual resistance in the sensor.

Further, a load-hold-unload study was done to characterize the creep error of the sensor, which was estimated to be below. Further, the different strain rate study was done and confirmed that the strain rate does not affect the sensor output in a significant way. However, with the hysteresis study, the accuracy of the working range was verified.

Additionally, the thermal stability study confirmed the temperature dependence of the electrical conductivity up to 70 °C. It is confirmed that resistance decreases with the increase in temperature and increases with a decrease in temperature. Finally, long term cyclic load is applied for studying the cyclic load stability test. It has found that the baseline was decreased with an increase in the number of cycles. This behavior is prevalent for polymer materials. This behavior can be attributed to the viscoelastic properties of the material. Initial work confirms the strain sensing application of the PANI based resin system. Furthermore, two more investigation results were discussed based upon different implementation processes, i.e., impregnated into glass fiber and layer on GFRP composites.

Both the study confirmed the sensitivity of the strain sensor around 1.5 and 0.8 for GFRCP and PDD layer GFRP composites, respectively. Constant amplitude cyclic tests confirmed linearity, repeatability, and low hysteresis error. Incremental and decremental amplitude study confirmed the importance of pre-stretching for stability. Additionally, a close investigation was done to establish the relationship between volumetric resistance and temperature change. GFRCP composites. The electric resistance change increase with the increase in temperature. Creep effect was also confirmed and found its effects negligible under tested conditions.

These promising results demonstrate that PANI-based composites could be an advanced structural material for self-sensing strain sensor. It is also important to highlight that, even though material has been demonstrated for structural strain sensor, however the isotropic behaviors of material limits its application in direction based, i.e. under bi-directional loading conditions strain can only be measured in a particular direction.

Chapter 3

Electromagnetic Interference Shielding

3.1 Introduction

In today's advanced aircraft, digital automated control systems replacing the use of analogue control systems of older aircraft. Modern aircrafts are more sophisticated and upgraded with advanced cockpit, automatic and digital navigation systems. With the increase number of sophisticated on-board digital equipment, concern the prevention it from electromagnetic disturbances [96]. On-board control systems, passenger carry-on devices, and externally generated EMI are three categories for aircraft . Other than on-board systems interfere and passenger carry-on devices, aircraft also can experience during flight from external sources like lightning strike, high-intensity radiated fields (HIRF) and electromagnetic pulses (EMPs) [96]. An EMI shield is often essential in most of the electronic devices to shield from unwanted interference. At large, metallic sheets are commonly used as EMI shield [97]. However, these metal sheet shield encloser facing challenges, too, as it increases the overall weight of the system [98]. Furthermore, allowing further interference caused by a reflected wave, which is the primary shielding mechanism of the metal sheet [99]. Therefore, lightweight conductive composite material development one of the fundamental researches for the aerospace industry to address EMI pollution. In the process of conductive composites development, researcher commonly uses metal and or nanofillers likes, carbon black, carbon nanotubes (CNTs) into the polymeric matrix to achieve high conductive composite materials [100]. However, to succeed in high conductivity, a high percentage of metal fillers are required, which not only increases the material's weight but also difficult to process. Even though CNT filled polymer composites can achieve high conductivity, but agglomeration issue and cost of fillers are the key factors which make these materials limited for commercialization.

On the contrary, intrinsically conducting polymers (ICPs) have a definite advantage because of tunable conductivity, corrosion resistance, lower density, cost-effectiveness, and ease of processing techniques [101]. Among different ICP, polyaniline (PANI), one of the most studies EMI shielding materials because of its excellent environmental stability with comfortably high conductivity. However, recent years researchers introduced nanofillers like CNTs, carbon

black, metal fillers into polyaniline to further improve the electrical conductivity [37–39,102,103].

3.2 EMI Shielding Theory

3.2.1 EMI Shielding Mechanisms

Electromagnetic (EM) radiation consists of two orthogonal waves, i.e., electric and magnetic. They travel together in the third orthogonal direction. The EM radiation further classified based on distance from source compare to $(\lambda/2\pi)$, where λ is the free space wavelength of the EM radiation. If the distance between EM source and shield is higher than the $(\lambda/2\pi)$ then the radiation considers as far-field (plane wave) radiation [104]. It is essential to mention here that the magnitude of both the field in EM radiation becomes equal when it is in the far-field (plane wave). The characteristic impedance, or intrinsic impedance(η) is the ratio of electric and magnetic field's amplitude.

When an EM plane wave strikes a conductive material's outer surface, two waves will be created, i.e., reflection(E_R) and transmitted (E_{I-R}) wave as shown in Figure 47. The amplitude of bifurcated waves depends on the intrinsic impedance of the EM shield material (η_s) and incident wave propagating domain (η_0) [105]. The transmitted wave further propagating through the shield material. However, its amplitude decreases along with its travel through the material. This is happened because of absorption done by the shield material. Once the propagating wave reaches the other end of the specimen's surface, it is again bifurcated into two waves; one will be reflected in the initial surface of the specimen, and the other will be transmitted [104]. The propagating EM wave within the conductive materials losses it's amplitude exponentially. Over a distance of one skin depth, the amplitude has decreased by $1/e$ or 37 %. This distance is known as the skin depth (δ) [106]. The third shielding mechanism, i.e., multiple-reflection, mostly depends on skin depth. If the thickness of the EMI shield is greater than the skin depth, multiple-reflection within the material will be absorbed by the material, hence it can be ignored [104]. However, If the thickness of the EMI shield is less than the skin depth, multiple-reflection will be significant in decreasing the Total EMI shielding effectiveness (SE_T).

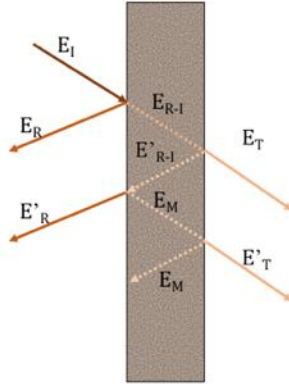


Figure 47: Schematic represent different shielding mechanisms.

3.2.2 Shielding Effectiveness

This section is the summary of the theoretical evaluation works on EMI SE_T in refs [107–110]. The SE is the quantitative measurement of electromagnetic shielding. It is defined as the logarithmic ratio of incident power (P_I) to transmitted (P_T) power of radiation (subscript I and T are used to represent the incident and transmitted wave). However, it can be rewritten to electric (E_T , E_I) and or magnetic (H_T , H_I) fields, considering the incident field is a uniform plane wave, and the media on each side of the shield are identical and free space. It is also noted that the power carried by an electromagnetic wave is proportional to the square of the RMS electrical/magnetic field.

$$SE_T \text{ (dB)} = 10 \log_{10} (P_I/P_T) = 20 \log_{10} (E_I/E_T) = 20 \log_{10} (H_I/H_T) \quad (5)$$

Nevertheless, the EMI SE also can evaluate by the adding of three shielding mechanism as discussed in the previous section, i.e. reflection loss, absorption loss and multiple reflections.

$$SE_T \text{ (dB)} = SE_R + SE_A + SE_{MR} \quad (6)$$

Where, SE_R , SE_A , and SE_{MR} are shielding by reflection, absorption, and multiple reflections, respectively. **Eq. (6)** were developed to determine the exact solution for SE. It is assumed that the incident field is a steady-state uniform plan EM wave. The shield material's properties are, thickness t , electrical conductivity σ , magnetic permeability μ ($\mu = \mu_0 \mu_r$) and permittivity ϵ ($\epsilon = \epsilon_0 \epsilon_r$). μ_r and ϵ_r are the relative permeability and permittivity, respectively.

$$\frac{E_I}{E_T} = \frac{(\eta_0 + \eta_s)^2}{4\eta_0\eta_s} \left[1 - \left(\frac{\eta_0 - \eta_s}{\eta_0 + \eta_s} \right)^2 e^{-\frac{2t}{\delta}} e^{-j2\beta_s t} \right] e^{\frac{t}{\delta}} e^{j\beta_s t} e^{-j\beta_0 t} \quad (7)$$

Where, η_0 ($\eta_0 = \sqrt{\mu_0/\epsilon_0}$) and η_s ($\eta_s = \sqrt{j\omega\mu/\sigma + j\omega\epsilon}$) are the intrinsic impedance in free space and shield material respectively. Similarly, β_s ($\beta_s = \omega\sqrt{\epsilon_0\mu_0}$) and β_0 ($\beta_0 = \omega\sqrt{\epsilon_0\mu_0}$) are the phase constant of shield material and free space respectively. Also, propagation constant γ ($\gamma = \sqrt{j\omega\mu(\sigma + j\omega\epsilon)} = (1+j)\sqrt{\frac{\sigma\mu\omega}{2}}$ in $\alpha_s + j\beta_s$ form) of the shield. The quantity δ is known as the skin depth of the material. Mathematically δ can be express as,

$$\delta = \frac{1}{\sqrt{\pi f \mu \sigma}} \quad (8)$$

Where, f is the frequency of the EM wave.

Eq. (6), further can be simplified with the assumptions, i.e. (i) shield material is “good conductor”, so that $\eta_s \ll \eta_0$, (ii) skin depth is much less than the EM shield thickness.

$$\frac{E_I}{E_T} \cong \frac{\eta_0}{4\eta_s} \left[1 - e^{-\frac{2t}{\delta}} e^{-j2t\beta_s} \right] e^{\frac{t}{\delta}} \quad (9)$$

Taking the logarithm to express the SE_T in the definition form **Eq. (4)**

$$\begin{aligned} SE_T(\text{dB}) &= 20 \log_{10} \frac{E_I}{E_T} \\ &\cong 20 \log_{10} \frac{\eta_0}{4\eta_s} + 20 \log_{10} e^{\frac{t}{\delta}} + 20 \log_{10} [1 - e^{-2\gamma t}] \end{aligned} \quad (10)$$

Eq. (9), represent the total SE of the good conductive shield materials. This equation represents three mechanisms of the shielding, which are reflection loss (1st term), absorption loss (2nd term), and multiple reflection loss (3rd term).

Further simplification of the **Eq. (6)**; assuming $\sigma \gg \omega\epsilon$ (conductive shield material) and neglecting multiple reflections ($t > \delta$),

$$SE_T(\text{dB}) \cong -39.5 - 10 \log_{10} \frac{\sigma}{2\pi f \mu_0} - 8.7 t \sqrt{\pi f \mu_0 \sigma} \quad (11)$$

Where,

$$\text{Reflection loss} = -39.5 - 10 \log_{10} \frac{\sigma}{2\pi f \mu_0} \quad (12)$$

And

$$\text{Absorption loss} = -8.7 t \sqrt{\pi f \mu_0 \sigma} \quad (13)$$

3.3 Sample Preparation

3.3.1 Preparation of Conductive Layer

To prepare the PDD conductive layer on FRPs, both CFRP and GFRP composites were fabricated separately with the help of a vacuum-assisted resin transfer molding (VaRTM) technique. Each set of GFRP and CFRP composites was made of ten and eight plies (100 x 100 mm), respectively. The cured composites were later cut into rectangular coupons (27 × 13.5 mm). The average thickness of the GFRP and CFRP panel was 1.96 and 1.93 mm, respectively. The geometry of the composite coupons is shown in Figure 48. The sandpaper was used for surface preparation before the attached PDD layer on top of the composite coupons. A polymer-based adhesive was used to attached the PDD conductive layer on composites.

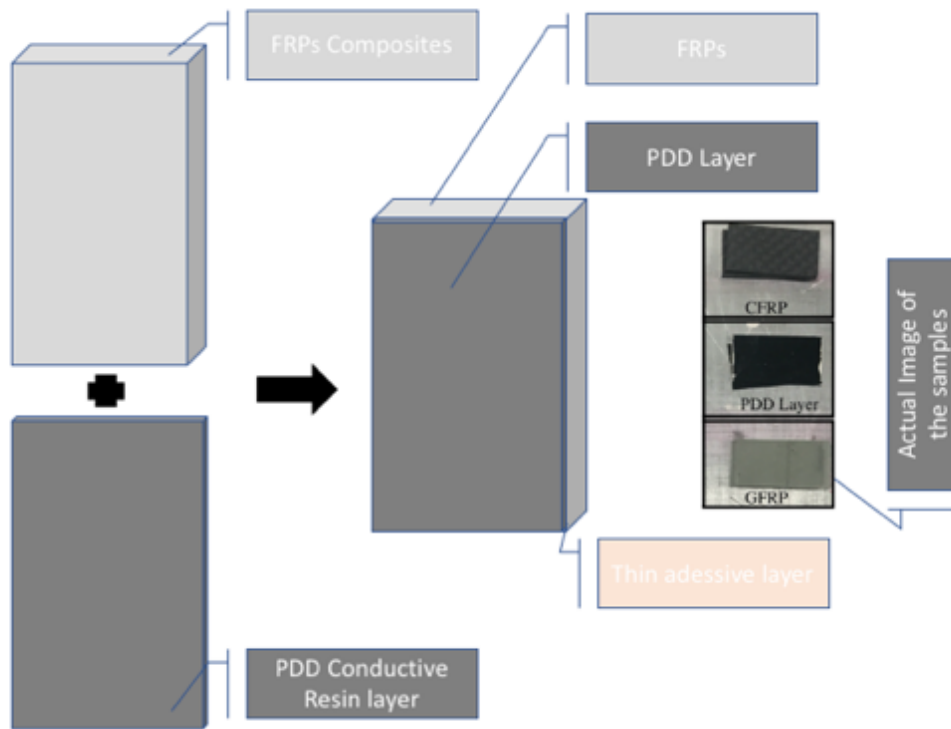


Figure 48: Steps involved to implement a conductive layer on FRPs

3.4 Characterizations

Electrical conductivity measurement was done with a digital multimeter (Keithley 2110-100, USA). Four prods resistance measurement techniques were adopted to eliminate contact resistance. To measure the through-thickness conductivity of the coupons', a silver paste was used to bind the copper electrodes and composite surfaces.

EMI SE in X-band (8.2-12.4 GHz) was measured by a waveguide using vector network analyzer (VNA, E8263B Agilent Technologies). Different thickness of samples was placed inside the cavity of the sample holder, which kept in between waveguide flanges and further connected to two ports of VNA. A full two-port calibration was performed before taking the measurements, and the S-parameters were determined [111]. The transmission coefficient (T), and reflection coefficient (R) were obtained from the measured S-parameters, using the following relations

$$R = |S_{11}|^2 = |S_{22}|^2 \quad (14)$$

$$T = |S_{21}|^2 = |S_{12}|^2 \quad (15)$$

Further, the following equations were used to calculate the total EMI SE (neglecting SE_{MR}).

$$SE_R = -10 \log_{10}(1 - R) \quad (16)$$

$$SE_A = -10 \log_{10}(T/(1 - R)) \quad (17)$$

$$SE_T (dB) = SE_R + SE_A \quad (18)$$

The Nicolson-Ross-Weir (NRW) algorithm was used to estimate the complex permeability and permittivity parameter of the material [112,113].

3.5 Results and Discussions

3.5.1 Effect of Shielding Components

The S-parameter obtain from VNA help to calculate the EMI SE directly with the help of **Eq. (13 -17)**. The SE_T versus frequency in X-band for all thickness PDD conductive layer is depicted in Figure 49. The conductivity of the samples with a thickness of 1.0, 0.8, 0.6, and 0.5 mm are 97, 73, 71, and 75 S/m, respectively. The useful EMI SE_T of ~ 19 dB was obtained with a minimum thickness of 1.0 mm shield thickness. In Figure 49, the sample with the highest thickness shows the superior SE_T compare to other thicknesses. This behavior can be explained with the theoretical expression in **Eq. (12)** that the shielding by absorption will increase with its conductivity and thickness. Similar evidence can be a notice in the experimental result in Figure 50. It can also be inferred that the shielding by absorption will increase with the increase of the product of $(f\mu)$. However, this change doesn't notice in the experimental result. Interestingly it can be noticed that the shielding by absorption doesn't influence with frequency in the X-band. Whereas, in the case of shielding by reflection will increase with increased conductivity and decrease with the increase of the product of $(f\mu)$ in **Eq. (11)**.

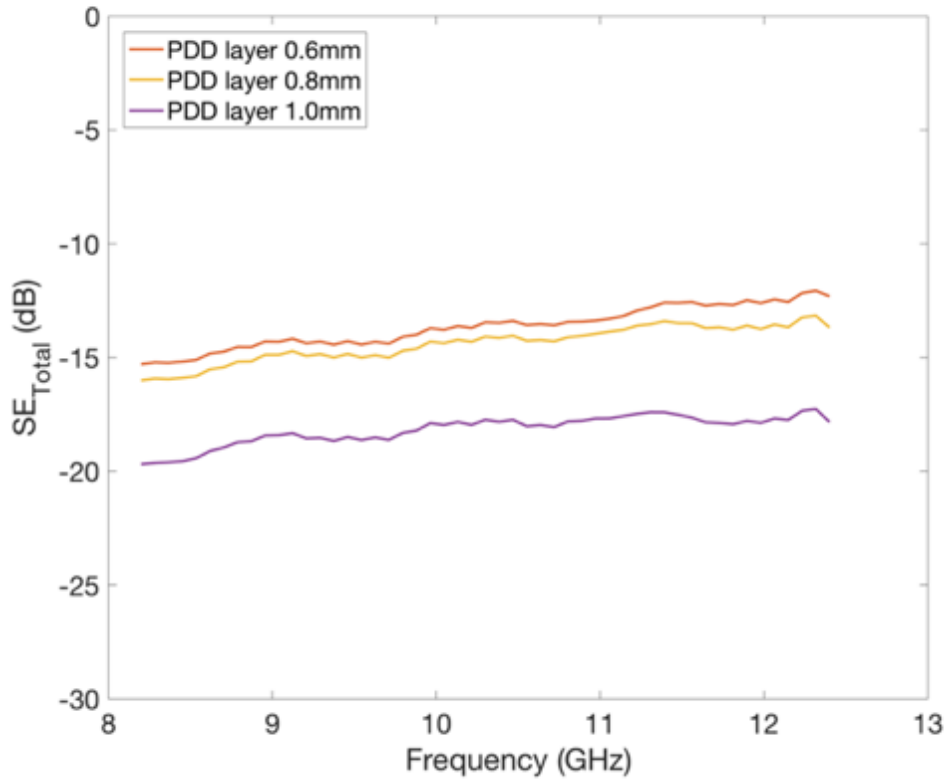


Figure 49: Total EMI ($SE_{Total} (dB) = SE_R + SE_A$) shielding of different thickness polyaniline based conductive layer in the frequency range 8.2–12.4 GHz (X-band).

Experimental results in Figure 51 showed a similar response. However, the conductivity change effect is not significant. This is because the surface conductivity of the PDD layer is not sufficient for high reflection loss as a metal shield does. However, low reflection and high absorption loss are preferable, as it will minimize the chance of EMI pollution to other devices. For most of the real-life applications, ~ 20 dB EMI SE is considered as an optimum level [114]. However, high EMI SE preferred for aircraft to protect receiving antennas from undesired signals generated within the aircraft. There is a need to shield the signal generating equipment to protect other equipment [109]. Current PDD conductive shielding material ideal for this type of requirement, however further study needs to improve the conductivity. The dominating absorption loss shielding mechanism of the PDD layer will help the other devices from EMI noise generated by signal generating equipment. Compare with the metal sheet for EMI shielding, the PDD layer not only light in weight, but also its high absorption shielding mechanism helps to minimize the re-reflection EM waves from one device to another. This re-reflection and corrosion are the common issues of the metal shield.

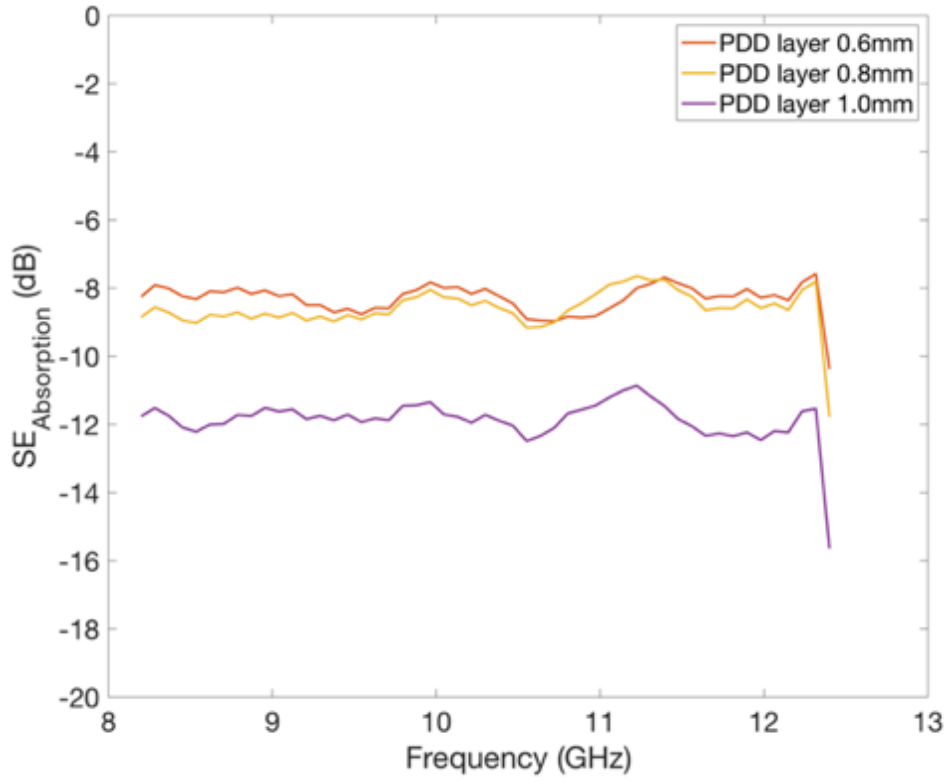


Figure 50: EMI shielding by absorption (SE_A) of different thickness polyaniline based conductive layer in the frequency range 8.2–12.4 GHz (X-band).

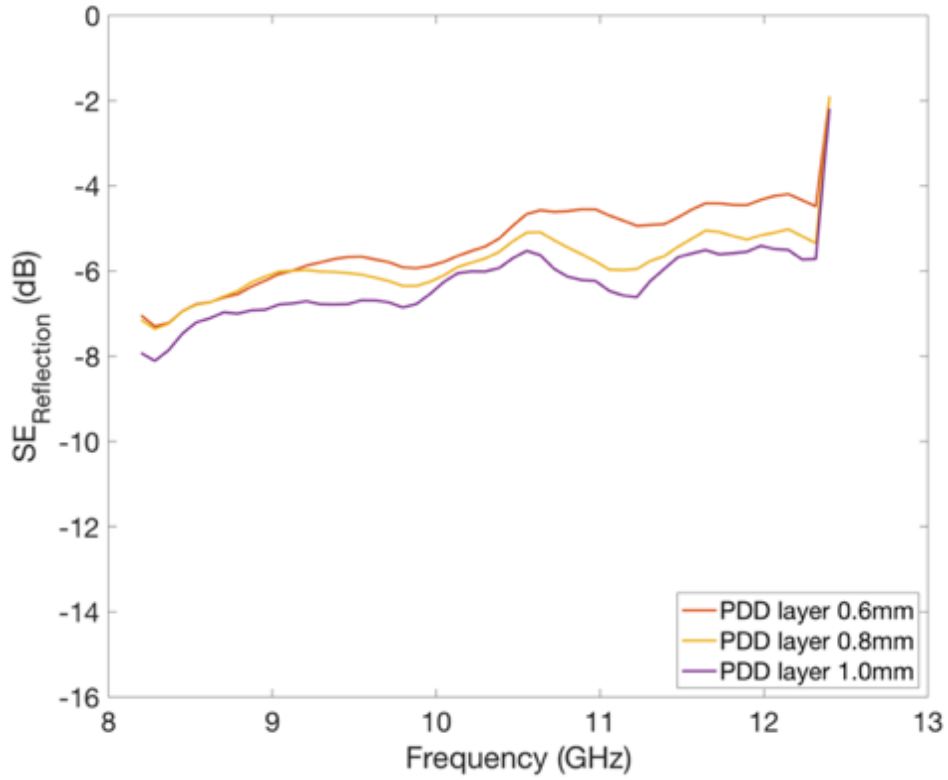


Figure 51: EMI shielding by absorption (SE_R) of different thickness polyaniline based conductive layer in the frequency range 8.2–12.4 GHz (X-band).

Table 5: EMI SE comparison summary with various materials.

Materials	Frequency (GHz)	SE _T (dB)	SE _A (dB)	SE _R (dB)	Thickness (mm)	Reference
Paraffin-PANI-Co	1-18	-	~ 10	-	10	[115]
PU-Cu-Ni		~ 18	~ 15	~ 3	1.5	[116]
PU-PANI	8-12	~ 10	-	-	1.9	[117]
Polyetherimide/Graphene@Fe ₃ O ₄		~ 16	-	-	1.9	[118]
Polystyrene (PS)-CNT		~ 15	-	-	2.0	[119]
PVB-PANI		~ 13	~ 8	~ 5	0.268	
PVB-PANI-FAC		~ 15	~ 12	~ 3	0.265	[37]
PVB-PANI-Co-FAC		~ 19	~ 16	~ 3	0.261	
PVB-PANI-Ni-FAC	8.2-12.4	~ 23	~ 20	~ 3	0.259	
PVC/Graphene/ Fe ₃ O ₄		~ 13	-	-	1.8	[120]
PANI-DBSA-DVB		~ 17	~ 10	~ 7	0.5	Present Work
		~ 20	~ 12	~ 8	1.0	

A comparison summary table of EMI SE with various reported materials shown in Table 5. The PANI-based conductive layer material (current study) able to showcase comparatively high SE values with a minimum thickness of 1 mm. Similar to all other materials, PANI based conductive layer to having absorption dominated shielding mechanism, which I desirable in most of the aerospace structures.

3.5.2 Effect of Multiple-Reflections and Skin Depth

It is essential to distinguish between reflection and multiple reflection mechanism to understand the shielding mechanism and its effects on SE_T. Figure 48 represents the difference between reflectional and multiple reflections. Once incident radiation (E_I) strikes on the 1st surface (external) of the shield, then it will be bifurcated into two waves. One will be reflecting, i.e., reflection wave (E_R), and another will be transmitted through the shield, i.e., transmitted wave (E_{I-R}). Further, the transmitted wave travels through the material, and its magnitude decreases exponentially due to absorption. Once the wave reaches to the other end of the shield's 2nd surface (internal), it will be further bifurcated into two waves, once again one will be reflecting the initial 1st surface, and another will be transmitted through the shield, i.e., transmitted wave (E_T). Once the wave reflected from the internal surface, its magnitude will again decrease due to absorption [104]. However, if the shield thickness is less the skin depth for the working frequency, then reflected wave would be re-reflect at the 1st surface and so on, which will reduce the overall SE_T of the shielding material. The contribution of multiple reflections can be neglected if the SE_T magnitude is more than 10 dB and or shield thickness

is more than skin depth [104]. Figure 52 shows the skin depth of the PDD layer for the X-band frequency range. It's clear from Figure 52 that the shield thickness variation range is higher than the estimated skin depth, which safely allows us to neglect the multiple reflections loss.

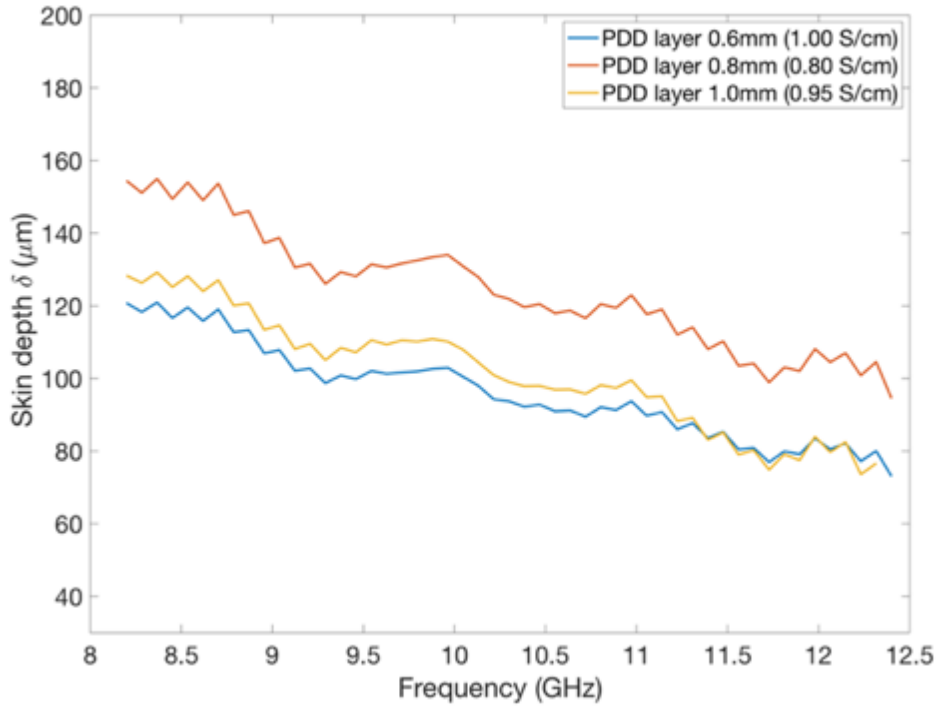


Figure 52: Variation in skin depth for different thickness of polyaniline based conductive layer in the frequency range 8.2–12.4 GHz (X-band).

3.5.3 Effect of Permittivity, Permeability, and Dielectric Loss

To understand and correlation shielding mechanism and EM attributes, complex permeability ($\mu = \mu' + j\mu''$) and permittivity ($\epsilon = \epsilon' + j\epsilon''$) values of the PDD conductive layer was calculated from experimental S-parameters and using the Nicolson-Ross-Weir (NRW) algorithm [112,113,121]. Figure 53 shows the real and imaginary part of the complex permeability and permittivity values of the PDD conductive layer in the X-band frequency range. The real and imaginary parts are representing the degree of polarization and the dissipation of the magnetic and electric energy, respectively. It is a desire to have a high value of ϵ'' and μ' for high EMI SE_T. Figure 53c and Figure 53d show both real(ϵ') and imaginary (ϵ'') permittivity values decreasing with increasing frequency and shield thickness. According to the EM theory, the dielectric loss may be contributed by the processes like natural resonance, debye dipolar relaxation, and electron polarization relaxation, etc. [122]. However, debye dipolar relaxation is a widespread phenomenon when conductive polymer mixed with conductive filler. For non-filler conductive polymers (like PDD layer), this phenomenon

doesn't notice (Figure 54), similar phenomena also reported by Kumar et al. [78]. The decreasing trend can be attributed to the decreasing ability of the dipoles, which failed to maintain the in-phase movement with incident EM wave [123]. The magnetic properties of the PDD layer also investigated with the help of complex permeability values. Figure 53a and Figure 53b both show the increasing trend of the permeability with increasing frequency.

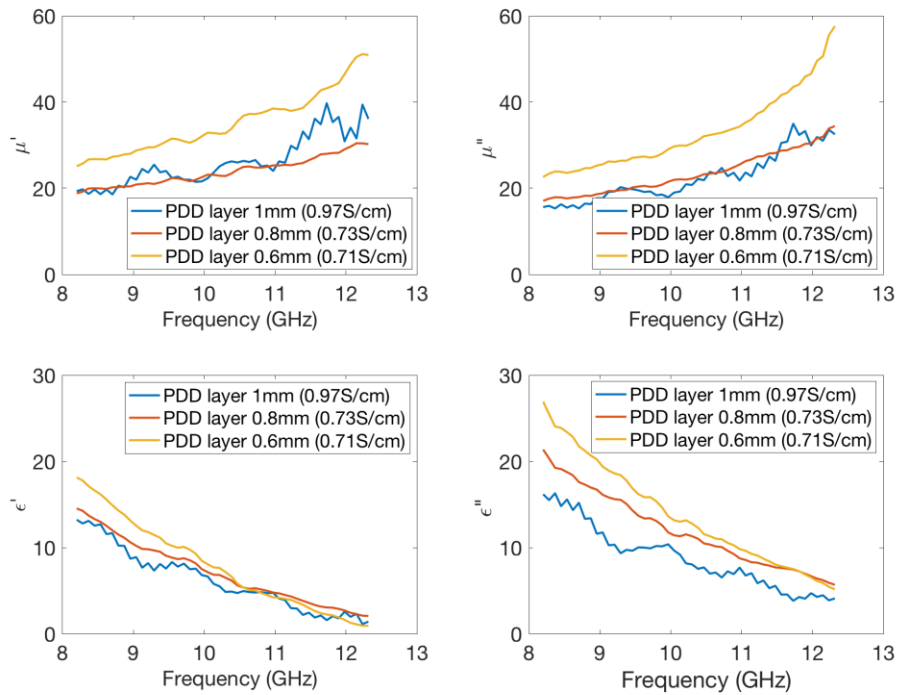


Figure 53: Complex permeability ($\mu = \mu' + j\mu''$) and permittivity ($\epsilon = \epsilon' + j\epsilon''$) of different thickness of polyaniline based conductive layer in the frequency range 8.2–12.4 GHz (X-band).

Variation of over frequency change (a) real part of permeability (b) (a) imaginary part of permeability (a) real part of permittivity (b) (a) imaginary part of permittivity

3.5.4 Experimental vs. Theoretical Results

Eq. (11), (12) and (17) were used to estimate the theoretical EMI SE_R , SE_A , and SE_T , of PDD conductive layer. Multiple reflections were ignored when the SE_A is more than 10 dB. It should be emphasized here that the above equations were developed for homogeneous materials; however, their application for a conductive polymer may need more investigation. The current study adopted these equations to estimate the EMI SE of the 1.0 mm PDD conductive layer with conductivity (DC) of 97 S/m, taking $\mu_r = 1$. Table 6 shows the comparison summary between theoretical and experimental EMI SE values of 1 mm PDD conductive layer, and Figure 55 represents the comparison for all cases which having more than $SE_A \sim 10$ dB.

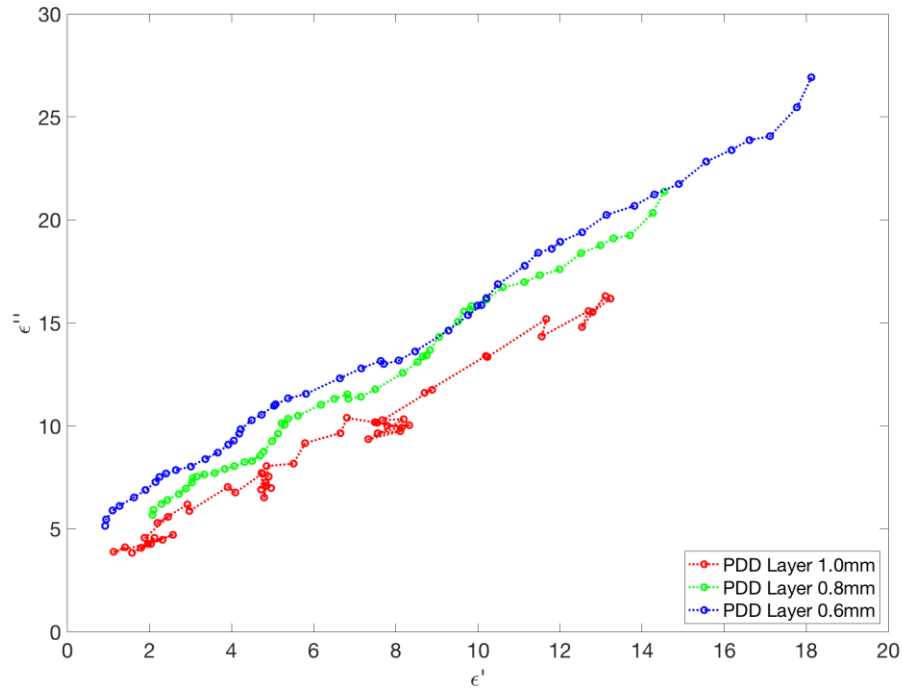


Figure 54: Cole-Cole plot (imaginary vs. real part of complex permittivity) of different thickness of polyaniline based conductive layer in the frequency range 8.2–12.4 GHz (X-band).

Table 6: Comparison between EMI SE results with experimental and theoretically calculation for 1 mm thick sample made of PANI-DBSA-DVB conductive resin.

Frequency (GHz)	Total EMI SE (dB)		Reflection (dB)		Absorption (dB)	
	Experimental	Theoretical	Experimental	Theoretical	Experimental	Theoretical
8.58	-14.89	-26.83	-6.78	-11.06	-8.12	-15.77
9.50	-14.23	-27.21	-5.84	-10.62	-8.39	-16.59
10.51	-13.53	-27.63	-5.01	-10.18	-8.52	-17.45
11.52	-12.76	-28.05	-4.64	-9.78	-8.12	-18.27
12.19	-12.31	-28.33	-4.31	-9.53	-7.99	-18.80

It's clear from Table 6 and Figure 55 that the theoretical model overestimates both the reflection and absorption loss. Several factors could be influencing the difference, the influence of the PANI chain dispersion into the crosslinking polymer, the dependency of the PDD layer on frequency [108]. High-frequency EM wave may reduce conductivity. In addition to that, inhomogeneity of the material also influenced the variation. The Jonscher universal power law for ac conductivity ($\sigma_{AC} = A \omega^s$) was further used to estimate the AC conductivity [124]. Figure 56 shows better agreement between the theoretical and experimental results considering σ_{AC} values, considering constant 'A=1' and 's' ~ 0.15.

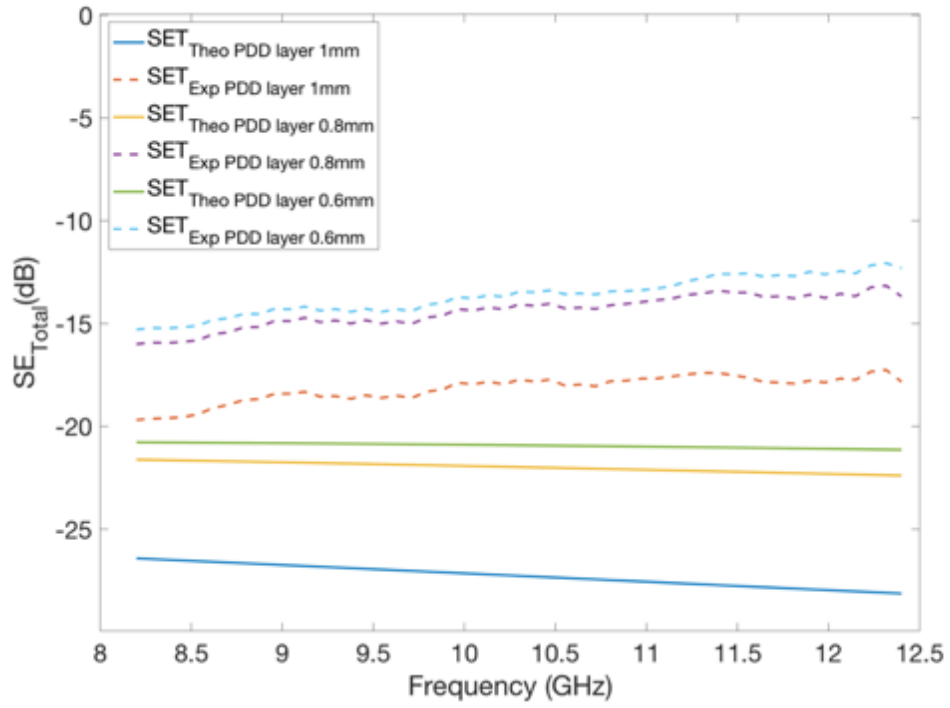


Figure 55: Experimental and theoretical EMI SE comparison for 1 mm, 0.8 mm, and 0.6 mm thick samples, considering DC conductivity.

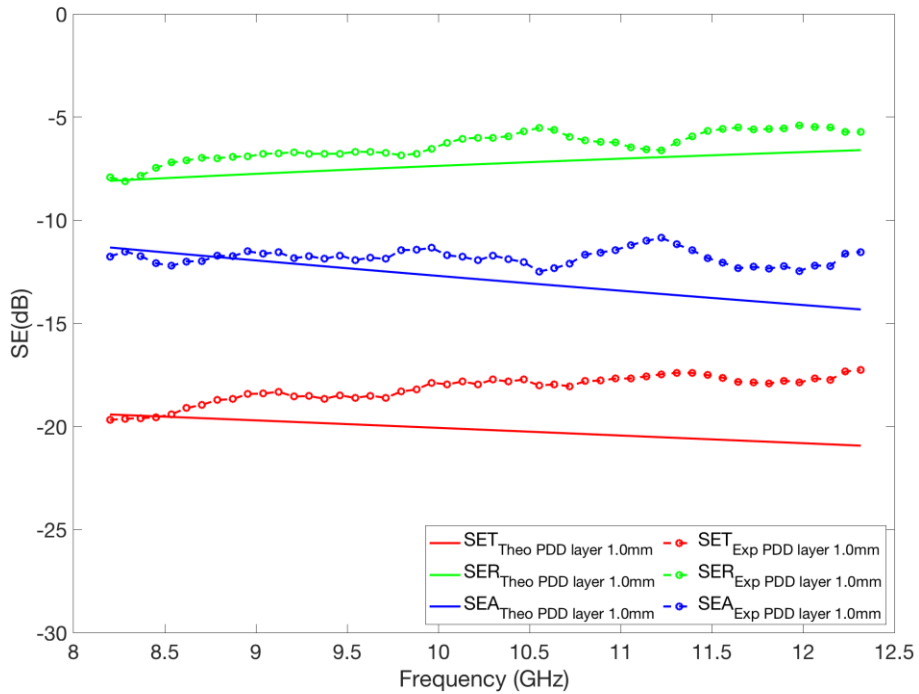


Figure 56: Experimental and theoretical EMI SE comparison for 1 mm, 0.8 mm, and 0.6 mm thick samples, considering frequency-dependent conductivity.

3.5.5 Composites with Conductive Layer

Figure 57 and Figure 58 show the EMI SE of GFRP and CFRP composites with PANI based conductive layer, respectively. Two different thickness (0.6 mm and 1.0 mm) of the conductive layer were studied for comparison. Similar to pure resin layer, PANI based conductive layer on both GFRP and CFRP composites able to shield the EMI radiation with maximum SE of 17 dB and 45 dB keeping layer thickness and conductivity of 1 mm respectively. In the case of GFRP composites, only PANI conductive layer contributed to shielding, whereas in the case of CFRP composites PANI and also carbon fibers in CFRP also contributed to high SE_A , which further improves almost more than double.

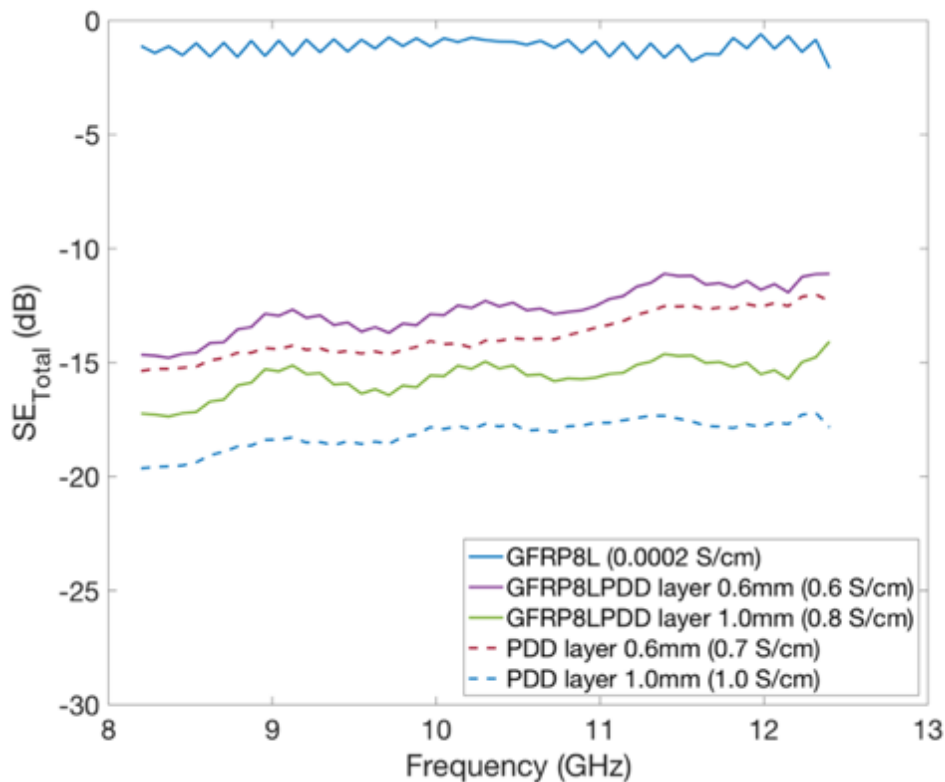
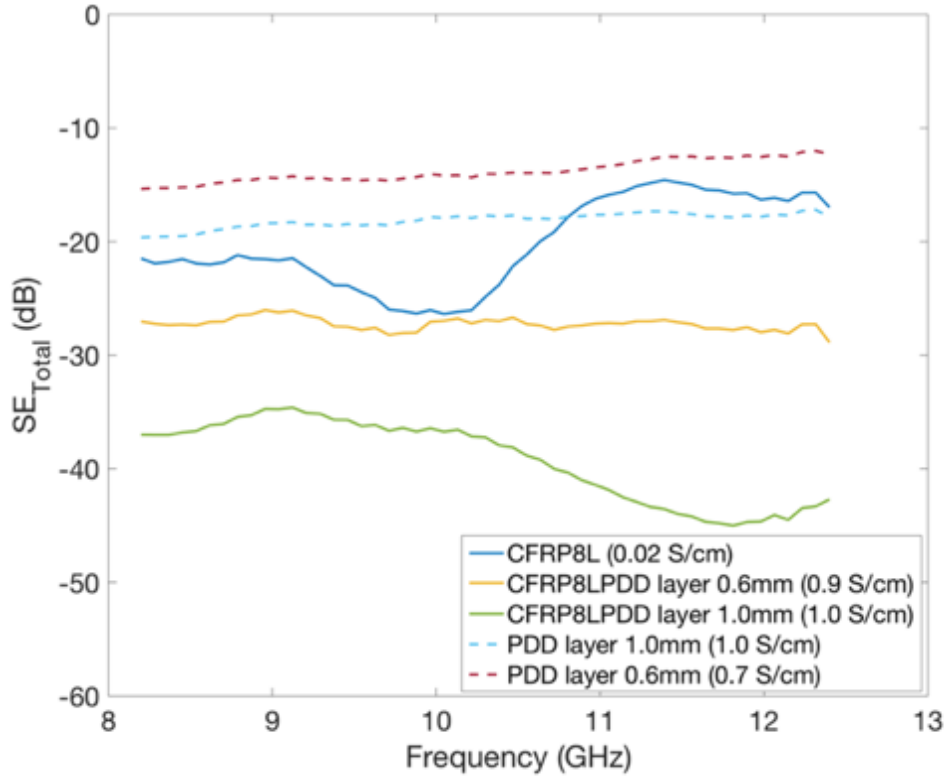


Figure 57: Total EMI shielding of GFRP composite with different thickness of polyaniline based conductive layer in the frequency range 8.2–12.4 GHz (X-band).



0

Figure 58: Total EMI shielding of CFRP composite with different thickness of polyaniline based conductive layer in the frequency range 8.2–12.4 GHz (X-band).

3.6 Design Analysis

Replacement of metal from aircraft is well known for its high specific strength. However, for the EMI shielding high electrically conductive metal sheet are covered on CFRP composites to improve the EMI shielding effectiveness. These metal sheets contribute significant additional weight to the aircraft structures. Therefore, high EMI shielding materials are needed with minimum weight. The density of conductive PDD resin is only 1.4 ~ 1.5g/cc, compared to copper at 8.9g/cc, which make this material promising for EMI shielding. This study reveals the shielding effectiveness can be achieve approximately 20 dB with a PDD thickness of 1 mm. Further, the high bulk electrical conductivity helps to absorb the EM wave compare to reflection, which is dominating for copper shield. This material shows that 99.999 % shielding can be achieve even at high microwave frequency range.

3.7 Summary

Doped polyaniline mixed with crosslinking thermoset polymer DVB was used as a conductive layer and characterized for structural EMI shielding materials. Single-step process, easy to fabrication, low density, tunable conductivity, and cost-effectiveness makes this material

promising for various engineering applications. The maximum SE was obtained ~ 20 dB in X-band (8.2 – 12.4 GHz) with an optimum thickness of 1 mm and conductivity of ~ 100 S/m. The EMI shielding mechanisms were studied both in theoretical and experimentally. It can be concluded from both experimental and theoretical results that the material is absorption dominated, followed by reflection. Both complex permeability and permittivity of the material were estimated using the NRW algorithm. It is found the SE by absorption is almost constant for all thickness; however, its magnitude change with thickness and conductivity change. This is because that the EM attenuation constant is almost independent of frequency. Lastly, it is essential to highlight that this novel PANI-based thermoset polymer matrix has been intensively studied in our previous work. Various functions like structural strain sensing, LSP and EMI shielding protection ability makes this material promising for multifunctional application in various industries like aerospace, wind turbine, electric vehicles.

Chapter 4

Lightning Strike Protection

4.1 Introduction

Lightning strikes one of the major concerns for aircraft safety. Due to the heavy current flow (100 A ~ 200 kA) during the strike, severe consequences may occur to the critical aircraft components [125]. In conventional aircraft, an LSP system is installed with the help of high conductive exterior skin and structures of the aircraft to protect from the lightning strike. This LSP system provides a safe conductive path on the exterior skin of the aircraft [126]. However, this system doesn't work with advanced polymer matrix composites aircraft. Advanced polymer matrix composite aircraft failed to provide a conductive path to flow the extreme electric current and electromagnetic forces generated by a lightning strike. Polymer matrix evaporation, burnout through lamina, are the common direct effect of the composite structure without LSP [49]. The most common LSP technologies for the advanced composite are the metal mesh/foil, Hybrid LSP (Mesh + adhesives), metalized fibers for LSP (Ni/Cu coating on CF), and conductive surfacing film. Metal mesh having resistance against lightning strikes is due to its high conductivity. Out of these technologies, metal mesh/foil is very popular. However, this technology is also facing problems like corrosion, weight, integration cost, and high repairing cost [125]. The additional metal mesh increases the overall weight which directly affect the fuel efficiency of the aircraft. Hence, there is a need to develop a high conductive composite structure with minimum weight to withstand not only high electric lightning current flow but also the acoustic shock and electromagnetic force.

4.1.1 Background of LSP

4.1.1.1 LSP Principal

Generally lightning occur various combination ways between cloud and ground, however cloud to cloud lightning are most common for aircraft. Lightning strikes on aircraft are commonly attach to the nose and an exit from tailing edge [126]. The attached lightning current took the shortest route with high conductive path to flow from nose to tail of the aircraft. However, the

lightning attached point move backwards as the aircraft move forwards, which commonly known as ‘swept stroke’ [126]. The energy density is concentrated at the root of the arc, nevertheless high conductivity helps to diffuse the energy quickly. This high energy density caused severer damages like material vaporization, fiber breakages. The objective of the LSP system is to provide a safe path for the lightning current to exit quickly through the exterior of the aircraft. This protection method based of Faraday Cage principal. However, the secondary objective of the LSP is to protect the EM interference devices from EM waves.

4.1.1.2 LSP Regulation and Standards

There are several government regulation and standards to test and qualify the LSP. The standard guidelines provided by Society of Automotive Engineers (SAE) aerospace recommended practices (ARP) are the current industrial practice. The SAE ARP 5412 and 5414, are two standards which illustrate the lightning phenomena via the simulated lightning waveforms (Figure 59) and the zones (Figure 60) on aircraft. The SAE ARP 5412 define the lightning current waveform in four components named A-D, to evaluate the direct effect. The component A represents the first return stroke, a current up to 200,000 A, components B and C represent the lightning environment caused by intermediate and long duration currents following return strokes or re-strikes while D represents the subsequent stroke [126].

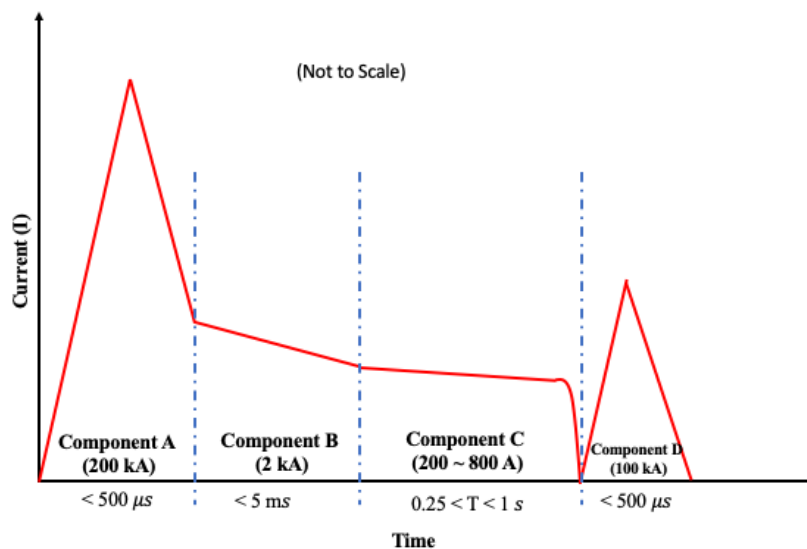


Figure 59: Lightning waveform defined by SAE ARP-5412B [127]

The SAE ARP 5414 divided the aircraft into three zones, namely Zone 1, 2, and 3; based on different type of lightning current. Zone 1, where lightning current attached to the aircraft; Zone

2, where swept stroke take place; and Zone 3 is the area which separate the Zone 1 and 2 and support larger area for lightning current [126].

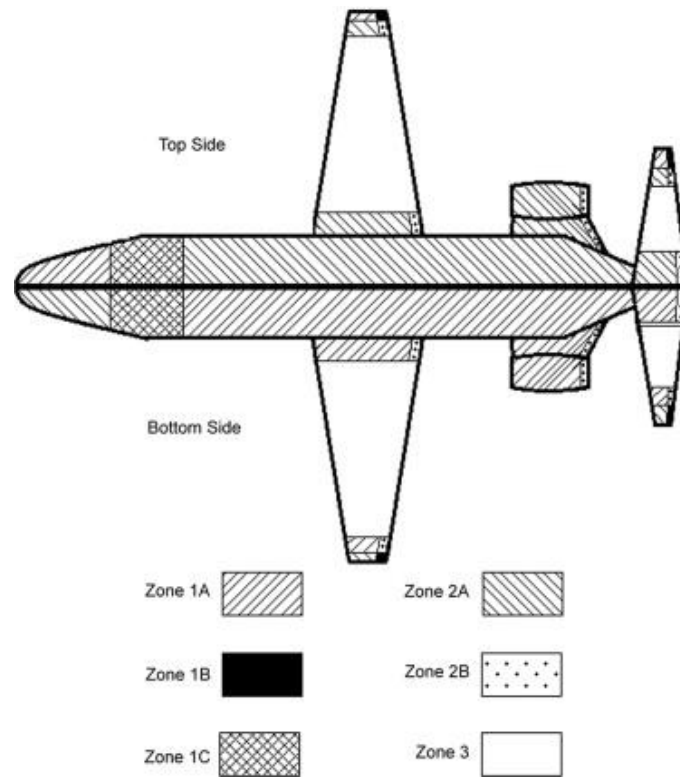


Figure 60: Different lightning zones of an aircraft [126]

4.2 Sample Preparation

4.2.1 CFRP Composites with PDD layer

For the lightning strike test, a polyaniline-based resin system, (as mention in section 2.2) was used to fabricate the LSP conductive layer for CFRP composites. Before fabricating the conductive layer, the top surface of the CFRP composites (as mention in section 2.3) were prepared with the help of sandpaper for proper bonding between CFRP and the conductive layer. The gravitational force was only used to layup the conductive layer on top of CFRP composites. For curing of the conductive layer, complete set of the specimen was kept into the oven and heated up from 23 °C to 130 °C at a rate of 10 °C/min, followed by 10 mins of dwell period at 85 °C and 130 °C. The summary of the specimen's properties mentioned in Table 7. The average thickness of the PDD layer was 0.24 and 0.41 mm for sample CPL-1 and 2.

Table 7: Summary of applied simulated lightning currents on CFRP composites.

ID	Materials	Peak Current [kA]	T ₁ [μs]	T ₂ [μs]	Charge (Q) [C]	Action Integral (I) [A ² s]
CPL-1	CFRP/PDD Layer	- 39.4	30.5	93.0	3.31	90714
CPL-2		- 40.2	31.6	92.6	3.37	93241

4.2.2 GFRP Composites with PDD layer

Similar to the CFRP composites preparation, four more GFRP composites also prepared with PDD layer. Similar technique and curing profile were used to fabricate the conductive layer on GFRP composites. The summary of the specimen's properties mentioned in Table 8. The average thickness of the PDD layer was 0.6 for sample GPL-1, 2; and 0.4 mm for GPL-3,4.

Table 8: Summary of applied simulated lightning currents on GFRP composites.

ID	Materials	Peak Current [kA]	T ₁ [μs]	T ₂ [μs]	Charge (Q) [C]	Action Integral (I) [A ² s]
GPL-1	GFRP/PDD Layer	- 41.6	31.8	90.9	3.40	96319
GPL-2		- 41.0	29.6	90.7	3.39	95537
GPL-3		- 59.6	31.1	91.2	4.83	197860
GPL-4		- 94.0	30.3	90.6	7.72	498132

4.3 Experimental

4.3.1 Simulated Lightning Current Test

For the simulated lightning strike test, SAE ARP-5412 standard was followed. The modified A component of the SAE ARP-5412 was applied to specimens. A current impulse generator (developed by Otowa Electric Co. Ltd., Japan) at the National Composite Center, Nagoya University, Japan, was used for simulated lightning current testing (Figure 61). This test setup capable of simulating a standard combination waveform defined by SAE ARP-5412. In this study peak current of -40 kA was applied CFRP and GFRP composites, in addition GFRP composites were tested with -60 kA and -100 kA. Figure 62 shows the closer view of the test

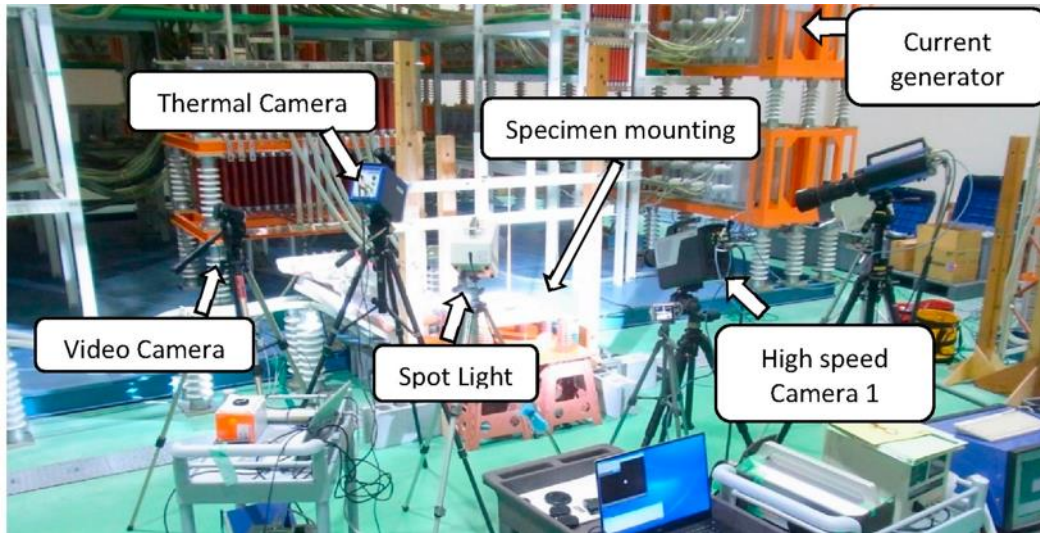


Figure 61: Simulated lightning strike test setup [128].

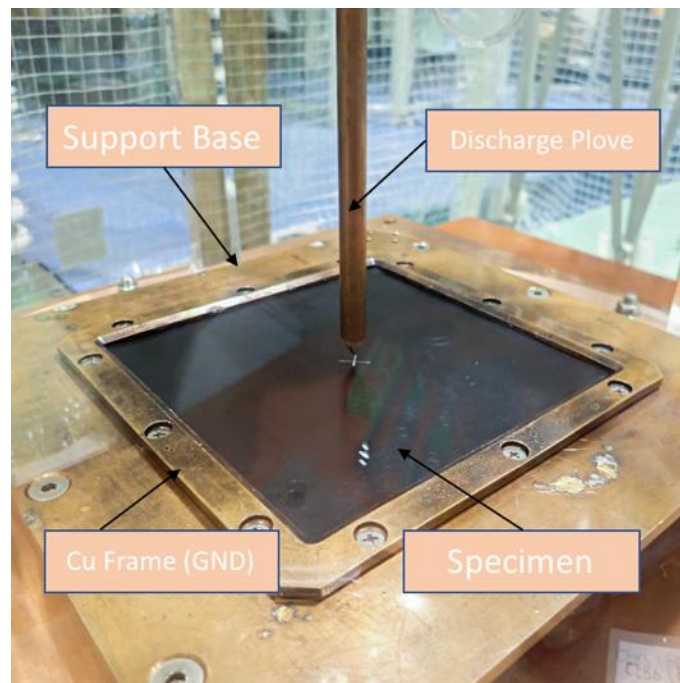


Figure 62: Closer view of sample with fixture with discharge plove

setup consists of a support fixture and electrode. As shown in Figure 62, the specimen was attached to copper base support with the help of a square copper frame jig, and the support was connected further to the ground of the current impulse generator. Later, the support frame was screwed to keep the specimen in place (fixed support) during lightning. Figure 63 and Figure 64 represent the current waveform for CFRP and GFRP composites. The current waveform can be characterized by its time-to-peak current (T1) and the time to decay to fifty percent of its maximum amplitude (T2). A current transducer (Model 1423, Pearson Electronics, Inc.) and a digital oscilloscope (DPO 3034, Tektronix, Inc.) were connected to the ground line to measure

the impulse current. Approximately 2 mm air gap between the discharge electrode tip and the specimen's top surface was maintained, along with the strike location at the center point of each specimen.

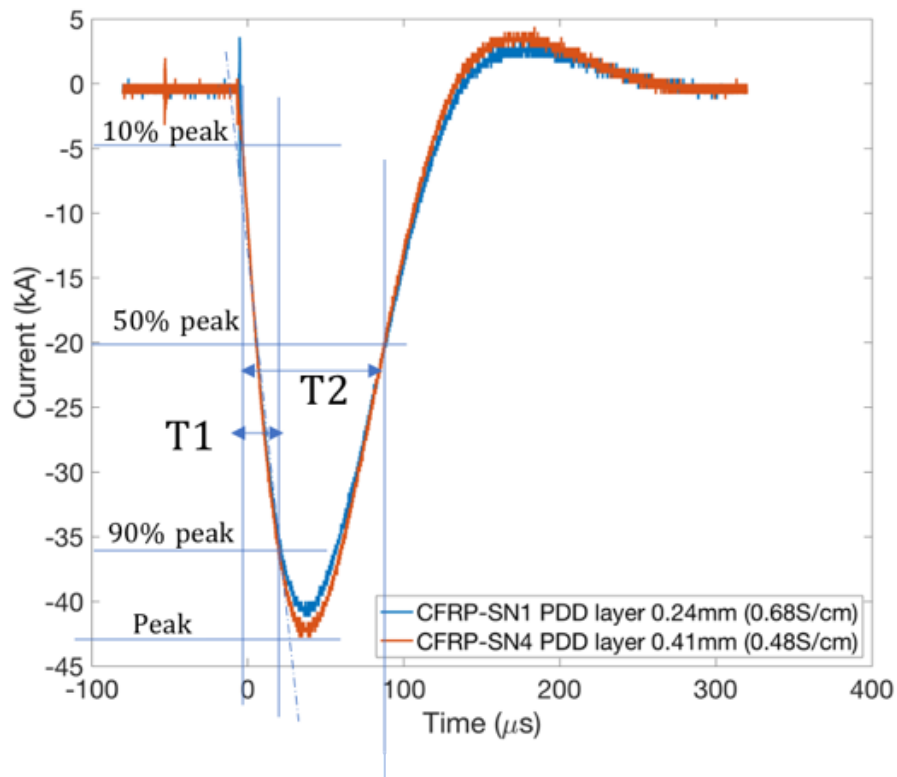


Figure 63: Details of the lightning current wave form for CFRP composites.

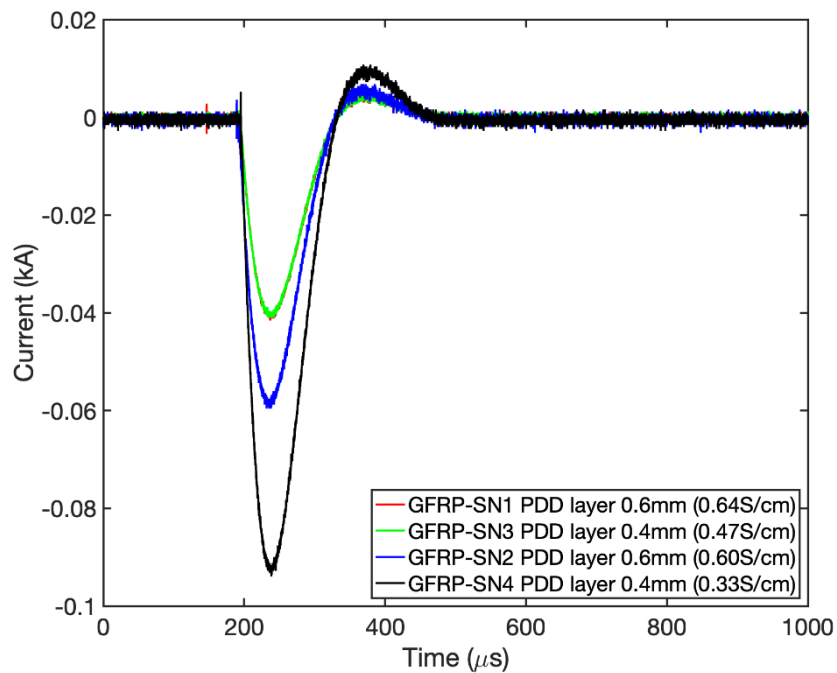


Figure 64: Details of the lightning current wave form for GFRP composites.

4.3.2 Residual Strength Test

To evaluate the strength of the lightning damaged samples, residual strength measurement was performed after the simulated lightning current test, a three-point flexural test was carried out. The specimens were cutout from sample panel for comparison. However, before test samples were cutout from edge of the panel and after lightning strike samples were chosen from the lightning attached point. The crosshead speed was 1 mm/min. To compare the flexural strength of the specimens before and after lightning damage, both specimens were cut from the tested specimens. The loading span was 73 mm. During bending test, the unlayered (back side) side were under compression whereas layered side was under tension.

4.4 Result and Discussion

4.4.1 CFRP Composites with PDD layers.

4.4.1.1 Lightning Damage Assessment with Visual Inspections

Figure 65 (a) and (b) show the top view photographs of the lightning damage on CFRP composites coated with two different thicknesses of the PDD layer of 0.24 and 0.41 mm, respectively. The specimen with a smaller thickness of the PDD layer is damaged more compare to others, where both were subjected to - 40 kA simulated lightning current. It is visible from the Figure 65 (a) (CFRP composite with 0.24 mm thickness PDD layer) that the PDD layer was utterly wiped off at the lightning strike point. As a result, the CFRP surface directly exposed to the high current and heat, which causes carbon fiber damages and epoxy decomposition (Figure 66). Whereas, Figure 65 (b) (CFRP composite with 0.41 mm thickness PDD layer) shows barely visible damage on CFRP composite even though the wipe off of the PDD layer. This is happened because of the wipe-off time delay between the two kinds of PDD layers. This time delay can be noticed from the high-speed camera data. Figure 67 represent the different time steps action on both the specimens. The comparison time steps (i.e., - 5, -3, 3.5, 9.5, 14, 24.5, 54, and 58 μs) were chosen carefully in between the period so that specimens were experiencing the peak lightning current. For an instant, it can be noticed in sample 2 that the PDD layer was able to guide the lightning current towards the ground path at $\sim 25 \mu s$ time step, whereas sample 1 struggled for the ground path at the same time step. This is because the initial shock wave able to damage the PDD layer and discontinued the conductive networks. As a result, high current concentrated at the lightning strike point and produced high-temperature cases fiber breakages, and epoxy decomposition.

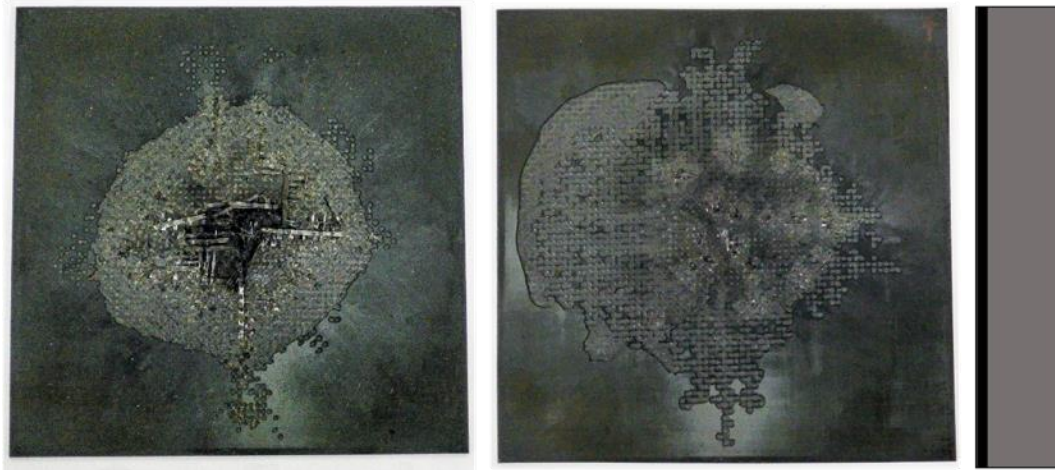


Figure 65: Top view photographs of lightning damages in CFRP composites with PDD layer (a) 0.24 mm thickness (b) 0.41 mm thickness

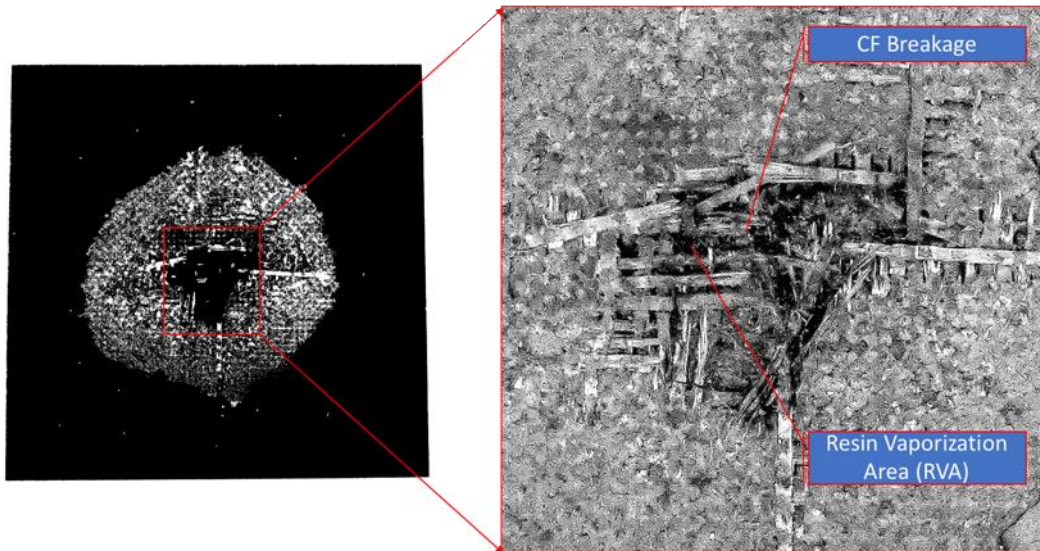


Figure 66: Different failure damages like carbon fiber (CF) brakeage, resin evaporation in CFRP composite with 0.24mm thick PDD layer.

Further, a close inspection was done at PDD wipe off the region to understand the PDD layer's failure mechanism. Figure 68 and Figure 69 represent the inside of the PDD layer failure mechanism of samples 1 and 2. It is seen from the figures that sample 1's carbon fiber bundles were not exposed sufficiently while preparing the surface (with the help of sandpaper) for the PDD layer, whereas it is well exposed in sample 2. This causes the weaker bonding between the CFRP and PDD surfaces, i.e., early failure of the PDD layer. It can be summarized for the above discussion that the CFRP composites with PDD layer needed a minimum thickness, which withstands the acoustic shock wave and high bonding strength between the PDD layer and CFRP composites' surfaces.

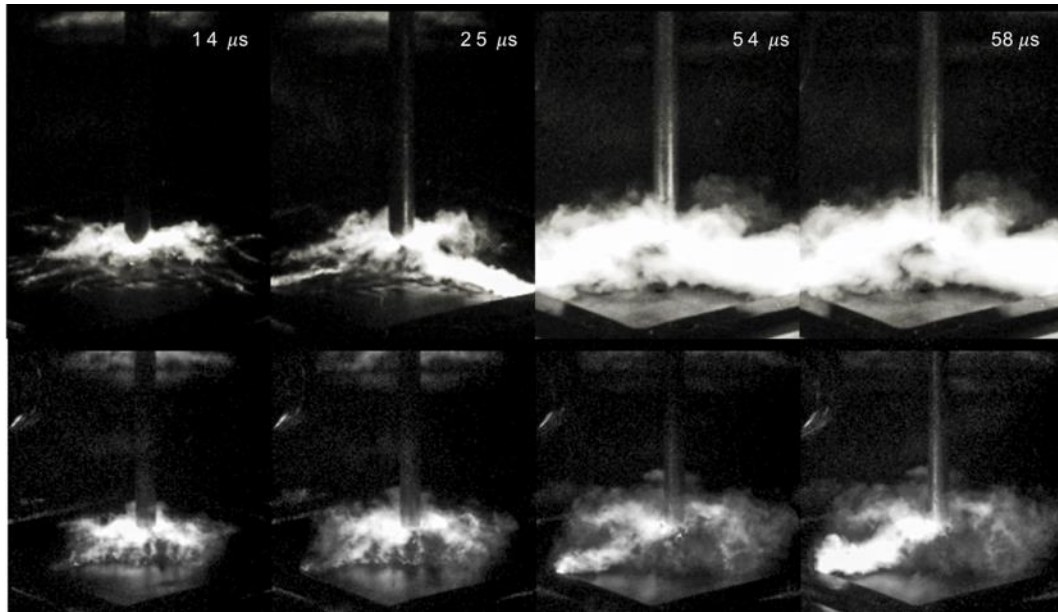


Figure 67: Comparison of current flow progress in CFRP composites with PDD layer (a) 0.41 mm thickness [1st row] (b) 0.24 mm thickness [2nd row] at different time steps recorded by high speed camera.

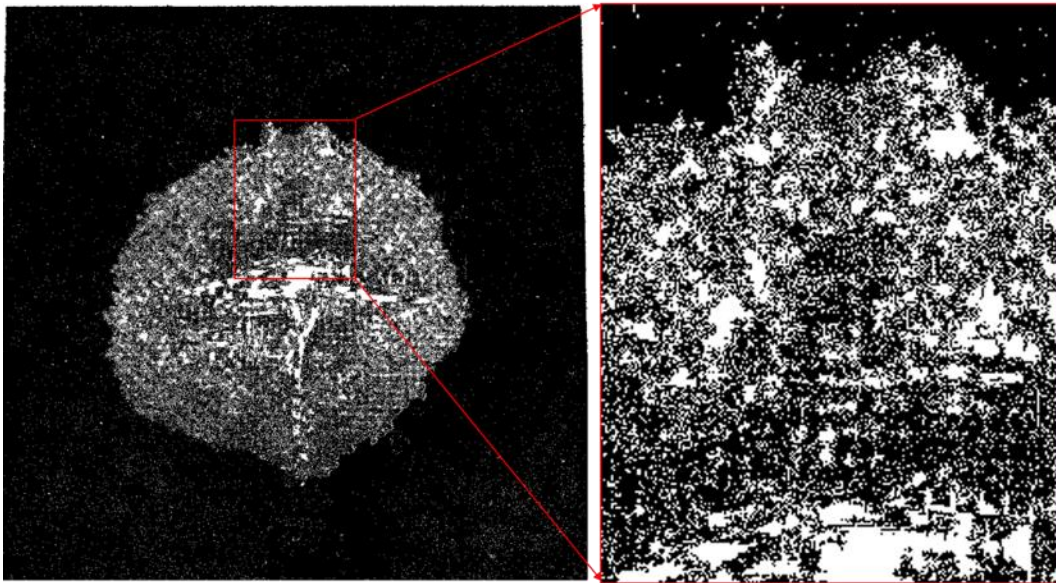


Figure 68: Failure mechanism analysis of 0.24 mm thick PDD layer on CFRP composite.

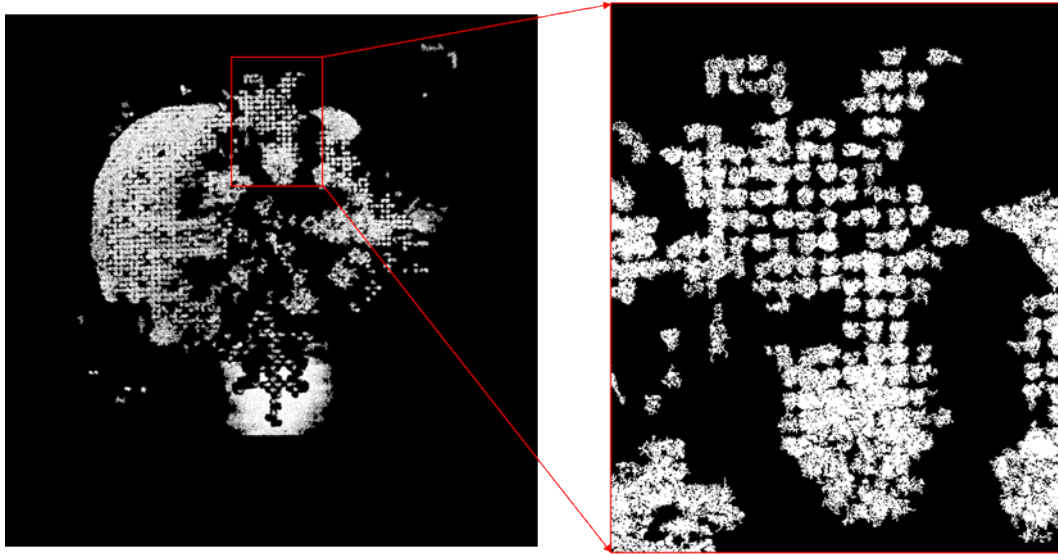


Figure 69: Failure mechanism analysis of 0.41 mm thick PDD layer on CFRP composite.

4.4.1.2 Lightning Damage Assessment with Ultrasonic Test

Ultrasonic tests were carried out to examine the internal damages of the specimens due to lightning current. An ultrasonic flaw detector (HIS3 HF, Krautkramer GmbH) with a 3.5 MHz transducer was used for the testing. Figure 70 (a) and (b) represent the tested C-scan and B-scan results of samples 1 and 2, respectively. Both the scan was taken from the backside (Bottom surface) of the specimens as the front side's PDD layer was wiped off from both the specimen. A circle shape damage can be identified in both the specimen from the C-scan, whereas its location can be noticed in B-scan. Comparing both the damages from B scan, it can be seen that, for sample 1, the damage has been penetrated through the 1st ply of the CFRP composites however, only surface damage occurred in sample 2. Further to quantify the damages, images are the further process to highlight the damages.

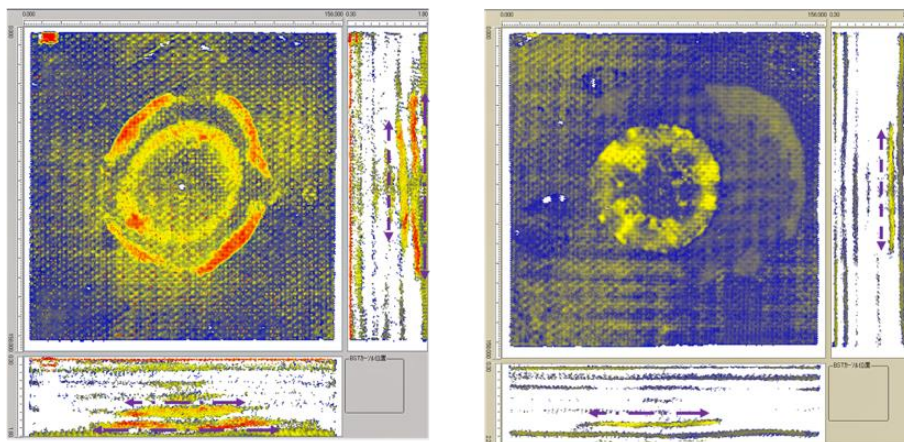


Figure 70: Ultrasonic results to assess inside damages of CFRP composites with (a) 0.24 mm and (b) 0.41 mm thick PDD layer.

4.4.1.3 Qualitative Damage Analysis Using Image Processing

Further, ultrasonic results are processed with the MATLAB image processing toolbox. Figure 71 (a) and (b) shows the processed ultrasonic scan results, highlighting the damages both PDD layer and CFRP lamina. It is estimated from the scan results that the damage is located approximately 1.4 and 1.76 mm from the backside of specimens 1 and 2, respectively. The equivalent distance from the top surface of the CFRP composite will be approximately 0.31 and 0.21 mm for specimens 1 (ply thickness 0.24 mm) and 2 (ply thickness 0.26 mm), respectively. In terms of CFRP plies, sample 1's damages were able to reach 2nd ply, whereas sample 2's damage was not able to penetrate the 1st ply. Further to verify the damages, a sectional microscopic analysis was also done and discussed in the next section.

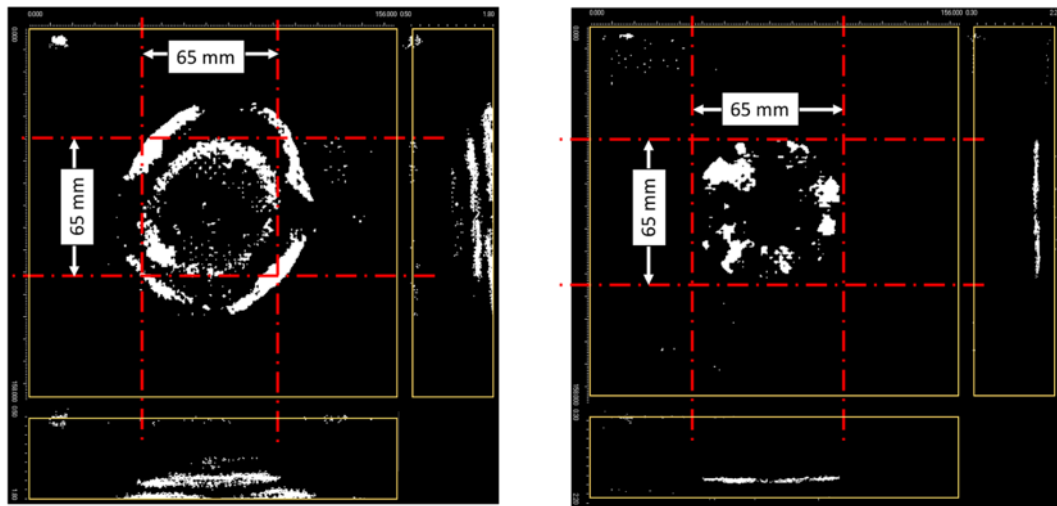


Figure 71: Qualitative damage evaluation of CFRP composites with (a) 0.24 mm and (b) 0.41 mm thick PDD layer.

4.4.1.4 Damage Analysis with Microscope

A microscopic analysis was done to understand the inside of the LS damages and cross verify the ultrasound test results. Because of severe damage of the sample 1, only sample 2 was chosen to study under microscope. Figure 72 (a), and (b) show the sectional observation of at the lightning point (center point of the sample) and 3 cm far away from the lightning point, whereas Figure 72 (c), represent the cross section of sample before lightning.

These results highlight that the 1st layer of CFRP was damaged, same as observed in the UT B-scope result. Furthermore, only delamination was noticed and occurred in between 1st and 2nd layers; no further delamination and matrix cracks were noticed in the thickness direction. This is because the PDD layer was able to guide the lightning current flow to ground. However, the mechanical strength maybe was not sufficient to withstand the shock wave. As a results

CFRP composite partially exposed to direct lightning current, which able to penetrate through matrix evaporation and leads to delamination at the 1st level. It is also observed that the delamination initiated from the lightning attached point, and gradually shifts in the longitudinal direction. Specimen was intact in all other layers and as a result it can retain more than 90 % residual strength. Further detail of the residual strength was discussed in next section.

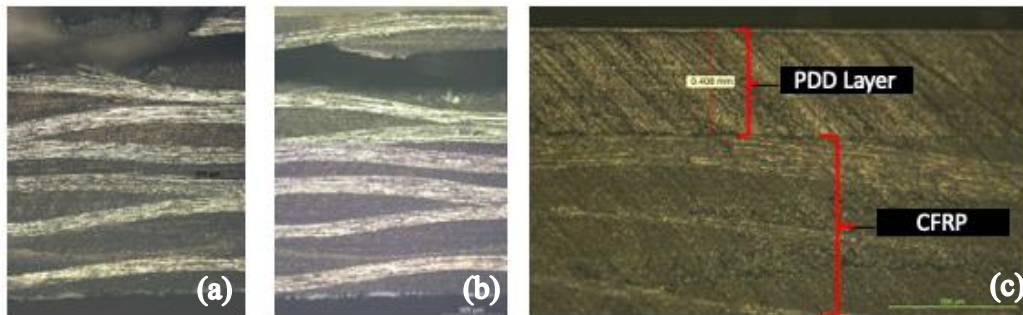


Figure 72 : Cross section observation of CFRP composites under optical microscope, (a) at the lightning point, (b) 3 cm far away from the lightning point, (c) before lightning test.

4.4.1.5 Residual Strength Analysis

To measure effectiveness of the PDD layer's for LSP, residual strength of the damaged samples was estimated. For that, 3-point flexural test was conducted to each sample before and after lightning strike. Flexural and Residual strength of the specimens before and after lightning test are shown in . It can be observed that the damage of CFRP protected with PANI-LSP showed more than 90% residual strength. This confirm that the PDD-layer with 0.4 mm thick with 50 S/m of conductivity is an effective LSP for CFRP composites.

Table 9: Summary of residual mechanical strength analysis

Specimens	Layer Thickness (mm)	Peak Current (kA)	Flexural Strength (MPa)		Residual Strength (%)
			Before LS	After LS	
CFRP [129]	---	- 40	610	147	24
CFRP/PDD Layer	~ 0.4		482	402	93

4.4.2 GFRP Composites with PDD layers

4.4.2.1 Lightning Strike Mechanism for Insulating GFRP Structures

The LS damage mechanisms of GFRP composites are different from CFRP composites. The ‘swept stroke’ is a well-known phenomenon in aviation industry. When an aircraft experience LS, there will be two lightning attach points, one at leading edge and another tailing edge and that’s how they become part of discharge path [130]. However, the lighting attached point at leading edge will move backwards along the fuselage as aircraft moved forward, whereas the lighting point at tailing edge will remain fixed. When the sweeping arc encounter an insulating structure part, then the arc will be stay attached to the last conductive point until the arc root reached to the another conducting point. As a result, the last conducting point will experience expensive heat energy and material deterioration compare to continuous arc sweeps. On the other hand, conductive structural parts under the insulating part may get influenced by the very high potential arc channel and start emit streaming. Hence, the insulating structures will be experience high electrical stress and may failed, which commonly known as electrical breakdown [130]. Similar situation can also find in case of long GFRP based wind turbine’s blades. There for, a lightning strike protection also needed for this kind of structural configuration. Other than above cases, the insulating GFRP surfaces also get polluted with partially conductive contaminants, and become prone to lightning strike attachment.

4.4.2.2 Lightning Damage Assessment with Visual Inspect

Two different thickness of PDD layer on GFRP composites were studied at different peak currents. Figure 73 shows the specimens after LS tests, where (a) – (d) represent the specimens with PDD layer thickness of 0.6, 0.6, 0.4 and 0.4 mm subjected to peak current of – 40 kA, – 60 kA, – 40 kA and – 100 kA respectively. It was clearly visible from the naked eyes that, all GFRP composites with PDD layer were safe under various peak currents. However, PDD layer on sample 4 (GFRP/PDD Layer/ SN-4) was completely failed without damaging the base GFRP composites at a peak current of - 100 kA. A clear impression of current flow direction can also be noticed on the PDD surfaces, which indicated the high conductive and shorted path for the peak current to ground.

Further high-speed camera frames were evaluated to calculate the time delay to ground lightning current. Table 10 represent the detail summary of the highspped camera analysis along with material properties. It is noticed that, the time period between lightning attachment

to the specimen's surface and connect to the ground, i.e. calling as ground time, decreases as increase the lightning peak current, irrespective to the conductivity change. For instant, it can be notice that, GFRP specimens, SN-3, 2 and 4; the peak current increased from - 40kA, - 60kA and - 100kA, whereas ground time decreases from 3.5 ms, 2 ms and 1.5 ms. Comparing with CFRP composites specimens, it is clear that CFRP took much longer time and its approximately 58 ms and 24 ms for sample 1 and 2 respectively. The CFRP composites were taken much longer time compare to GFRP composites, as because the available conductive paths are different in both the cases. In case of CFRP composites, current can flow in all three orthogonal direction, whereas GFRP composites only in PDD layers. As a result, in case of GFRP composites PDD thickness, mechanical properties and conductivity was sufficient to guide the current to ground quickly. Further, compare the CFRP samples, i.e. SN-1 and 2, its noticed that sample 1 took almost double of sample 2, and as a result concentrated lightning current damaged both PDD and CFRP in case of sample 1, whereas only 1st layer damage has been noticed in sample 2. This is because the longer period of current flow into the samples damaged the PDD layer and penetrated into CFRP composite, and damaged fiber and epoxy matrix.

Table 10 : Summary of the highspeed camera analysis

Parameters	CFRP/PDD layer		GFRP/PDD layer			
	SN-1	SN-2	SN-1	SN-2	SN-3	SN-4
PDD layer Thickness (mm)	0.24	0.41	0.6	0.6	0.4	0.4
Longitudinal Conductivity (S/m)	68	48	85	75	40	126
Ground Time (ms)	58	24	3	2	3.5	1.5
Through Thickness Conductivity (S/m)	0.006	0.003	---	---	---	---

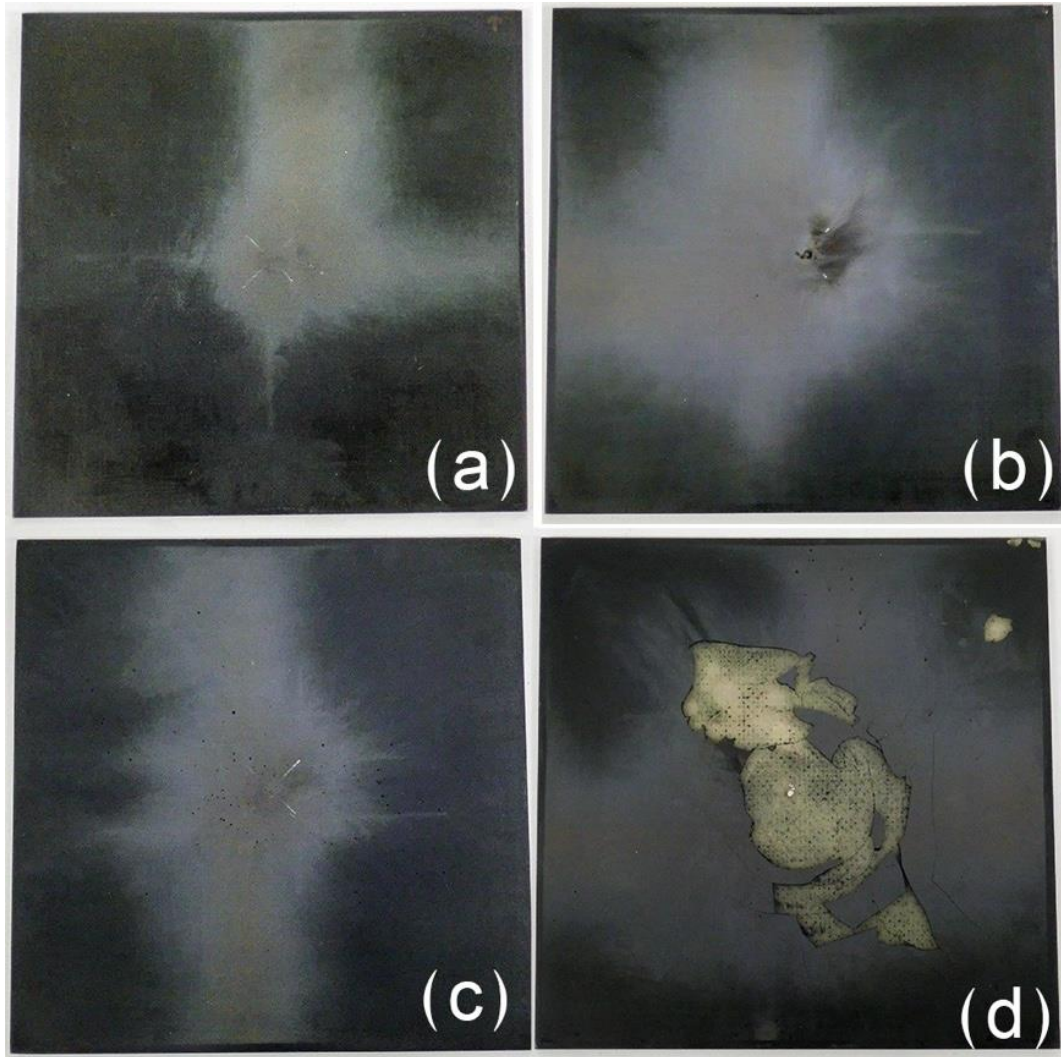
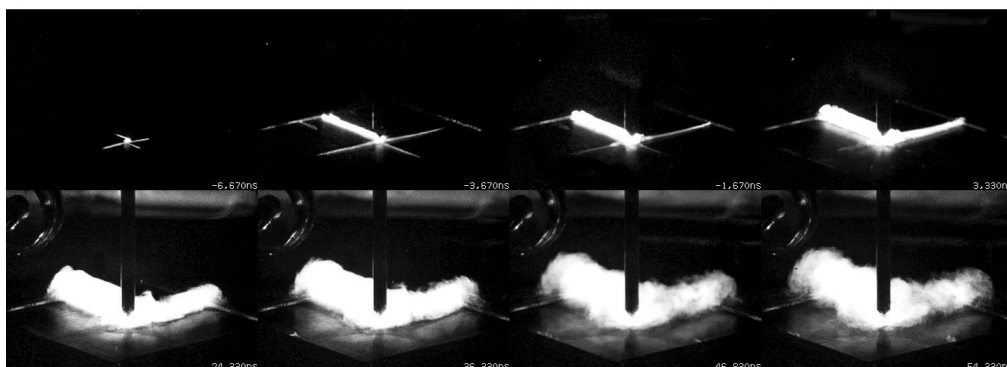


Figure 73: Lightning tested GFRP samples with PDD layer (a) thickness of 0.6 mm and -40kA peak current, (b) thickness of 0.6 mm and -60kA peak current, (c) thickness of 0.4 mm and -40kA peak current, (d) thickness of 0.4 mm and -100kA peak current.



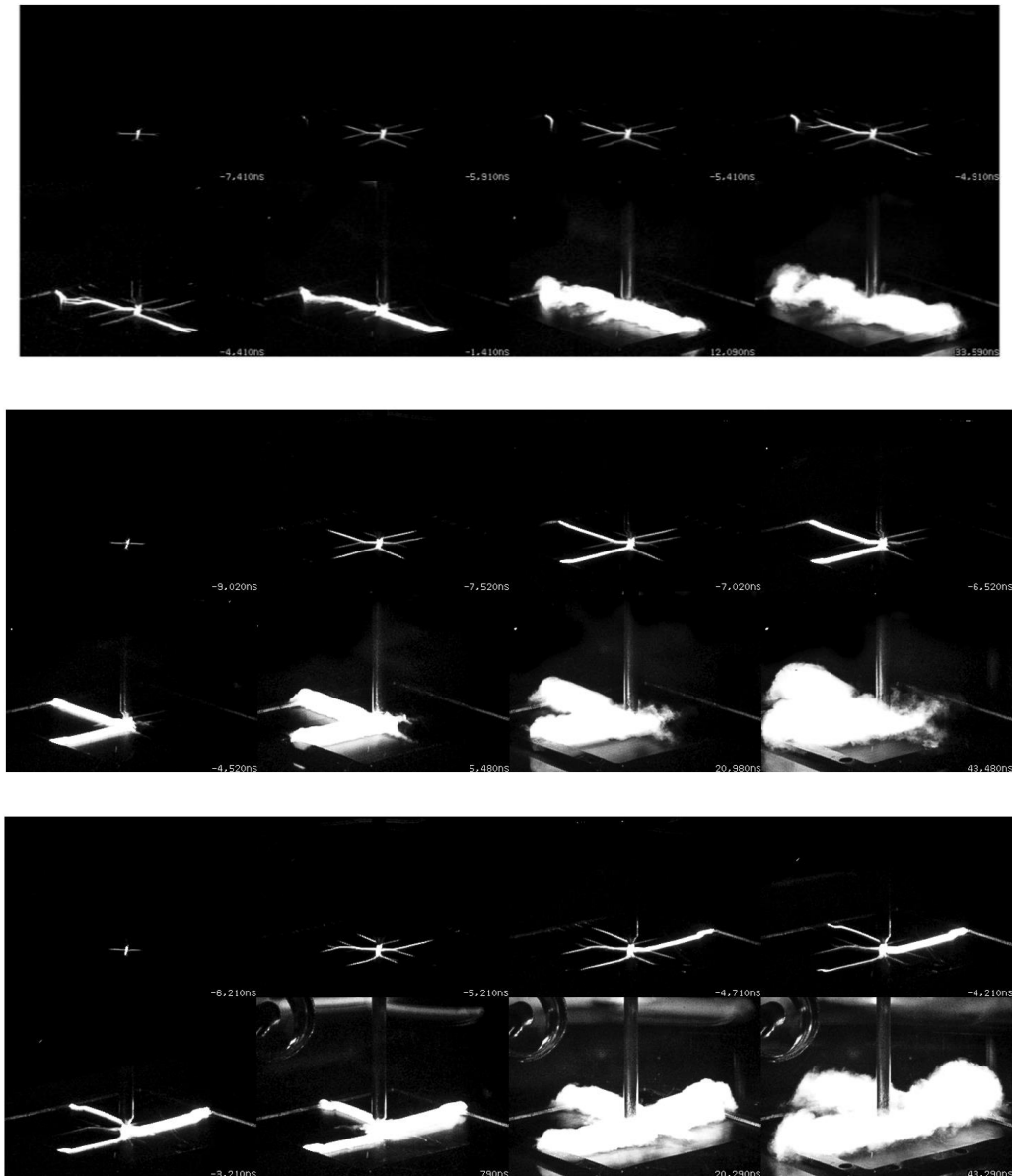


Figure 74 : Current flow development for GFRP composites with PDD layer

4.4.2.3 Lightning Damage Assessment with Ultrasonic Test

Similar to CFRP composites, internal damage analysis of the composites was performed with ultrasonic setup. However, no damage noticed in any of the GFRP composites either in B-scan or C-scan. Which confirmed the PDD layer thickness was sufficient to guide the current to flow without damaging the GFRP composites.

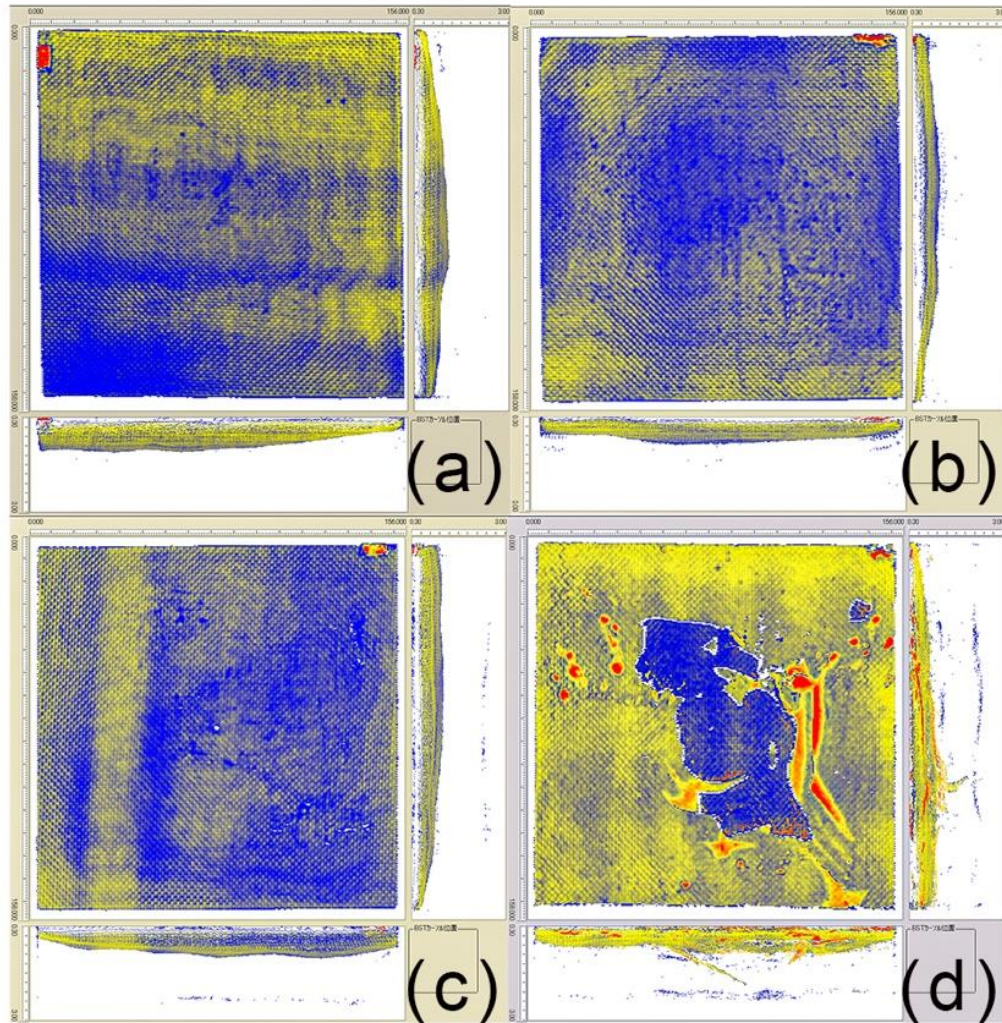


Figure 75 : Ultrasonic results to assess the inside damages of GFRP composites with PDD layer subjected to (a) -40kA (b) -40kA (c) -60kA and (d) -100kA.

4.4.2.4 Damage Analysis with Microscope

Further, damage analysis also done under microscope and no damages noticed in any of the GFRP samples, which confirmed the no internal damages occurred in the specimens even after -100 kA peak current.

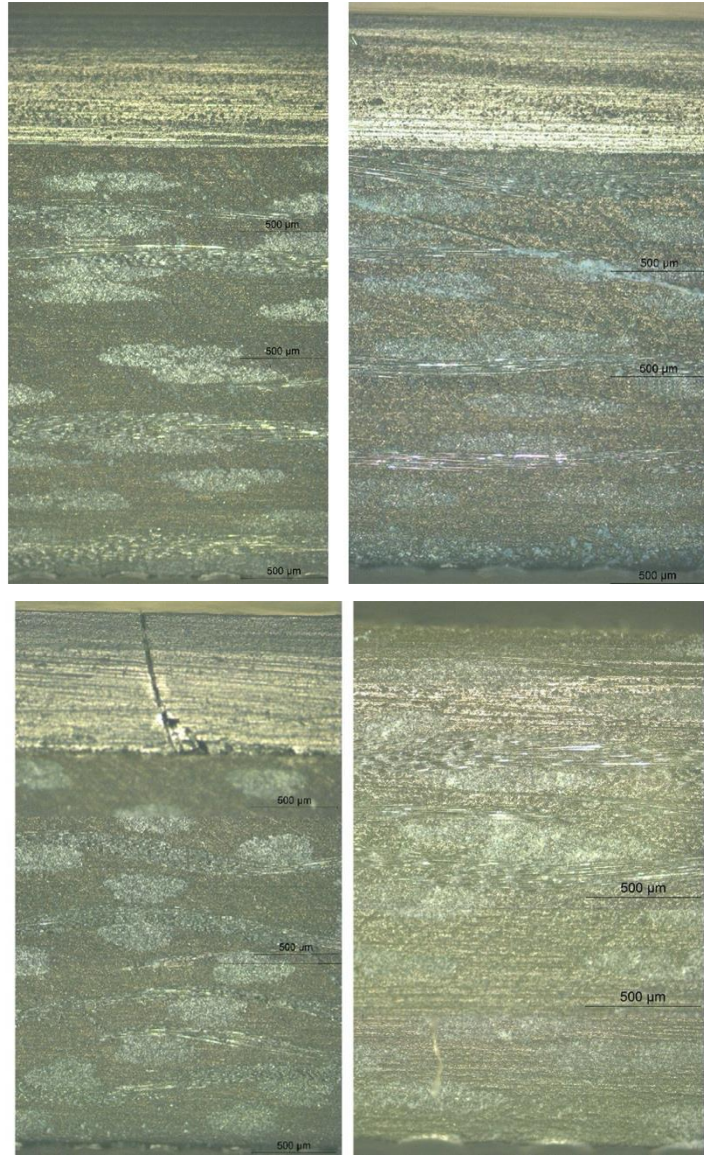


Figure 76 : Cross section observation of GFRP composites under optical microscope at the lightning point (a) -40kA (b) -40kA (c) -60kA and (d) -100kA.

4.5 Design Analysis

For aircraft LSP system design, low weight on of the basic design criteria to improve the overall efficiency of the aircraft. However, existing LSP system contributed significant additional weight to the aircraft. The density of the PDD layer is as low as $1.4 - 1.5 \text{ g/cm}^3$, compared to the 8.9 g/cm^3 of Cu and 2.7 g/cm^3 of Al [131]. Therefore, the PDD could be used in LSP application. A residual strength analysis also confirmed it ability to retain the strength more than 90 %. Above study also confirmed the 0.4 mm thick PDD layer will be sufficient to achieve this residual strength. In additions, PDD LSP system having additional other advantages like, its corrosion resistive, easy and cost-effective repairing, compare to existing Cu/Al foil system. Moreover, the PDD LSP system much more cost effective.

4.6 Summary

In this study two different thickness of polyaniline based conductive layer on CFRP composites were evaluated for lightning strike. A simulated peak current of – 40 kA were subjected to both the specimens. For post damage assessment, high speed camera, ultrasonic test results were analyzed. A circular damage was noticed in both the samples with a diameter of 6.5 cm, however its penetration limited to 1st and 2nd ply for the specimens with 0.41 mm and 0.24 mm thickness of PDD layer respectively. High speed camera study also helps to understand the both current flow and damage of PDD layer. Further, similar techniques were used for GFRP composites and tested additionally for - 60 kA and – 100 kA peak current. It can be summarized from the above section that, both CFRP and GFRP composite with minimum PDD layer thickness of 0.4 mm can save the FRPs from LS current up to – 40 kA. However, 0.4 mm thick PDD layer on GFRP composites further save the GFRP composite even at -100 kA peak current. CFRP with 0.21 mm thick PDD layer under – 40 kA peak current tests indicate that, the interface between CFRP and PDD layer play a major role to reduce the damage in CFRP. Good bonding at the interference will reduce the contact resistance and could save both PDD layer and CFRP. However, further study requires to investigate and improve the PDD and CFRP interference properties both mechanical and electrical. In addition, GFRP LSP study further reveal that lightning current flow can be control and flow only through the PDD layer. An insulating layer between PDD and CFRP could help to do that, however further study needed to optimize the thickness of insulating layer and the PDD layer. A similar study also reported by Han et al.[131]. It is also significant to highlight that the PDD coating technology having several advantages, namely easy to repair, economical and light weight compare to all existing LSP technologies.

Chapter 5

Conclusion

In this thesis, the design and development of multifunctional material for aircraft have been introduced. The novel conductive material addressed as a PDD system was characterized as a multifunctional resin material for its application as a strain sensor, EMI shielding, and LSP. Initially, the resin was characterized to qualify as a structural strain sensor by evaluating its various aspects like stain sensitivity, reliability, reversibility. A linear working range of 0.03 ~ 0.3 % strain was estimated with a sensitivity value of 0.9. However, the tunability nature of the material gives us opportunities to design the sensitivity of the sensor.

Further, a long cyclic load up to 500 cycles were also studies for stability and reliability. Once the material was characterized for strain sensor, its application on composite structures were confirmed with two different fabrication process; fiber reinforced conductive composites and a conductive layer on composites. Both the study confirmed the linearity zone, reliability, and sensitivity of the sensor. This study not only limited to structural strain sensors but also suitable to detect the damage at high strain.

After successfully characterized and implemented, the material was evaluated for EMI shielding. Different thicknesses of the PDD system were examined for EMI SE to optimize the shielding thickness. It is found that the absorption loss is the primary shielding mechanism, followed by reflection. Maximum depth of 1 mm with an electrical conductivity of 100 S/m able to generate SE value of ~ 20 dB in X-band frequency. Different aspects of SE were evaluated with the help of dielectric properties. The comparison between experimental and theoretical SE results was made to understand the effects of the multiple reflection, conductivity, and shield thickness. The skin depth study of the shielding material also done to address the multiple reflection mechanism and its effects on total EMI SE values. Lastly, successfully implemented on CFRP and GFRP composites in the form of a conductive layer on it. It is found that a considerable improvement in SE value notices mostly due to an increase in absorption loss.

Further, optimization of PDD layer was study to qualify the optimized PDD layer for LSP. Two different thickness of PDD layer was studies to optimized the layer thickness for LSP with a peak current of - 40 kA. For the damage evaluation and study the failure mechanism both CFRP and PDD layer, highspeed camera was used to record the lighting event and further

ultrasonic and image processing technique were used to evaluate the damage both qualitative and quantitative way. It is notice that, PDD layer with ~ 0.4 mm thickness and conductivity ~ 50 S/m can able to save the CFRP composite up to - 40 kA lightning current.

This thesis successfully introduced a novel multifunctional structural material which not only act a self-sensing structural strain sensor, but also can be used to detect damages at high strain, shield from EMI radiation and protect from lightning strike.

5.1 Impact

5.1.1 Aircraft

Lightning strike, electromagnetic interferer etc. are the savior threats for aircraft safety. To improve the aircraft safety by installing additional equipment not only increase the overall weight of the aircraft but their maintenance is expensive too. Current research outcome address all of these safety threats with one solution, a multifunctional structural material. This material not only reduce the overall weight but also less expensive, easy to process, corrosion resistive. An appropriate fabrication may further improve the efficiency of the materials.

5.1.2 Electric Car

Another immerging field of engineering is the futures' smart electric vehicles (EV). They are promising for the future markets because they are driven by electric power and produce zero emission. To optimize the weight of the EV cars, this industry may also introduce advanced composite in their various components. In parallel, the advanced electronics devices and Wi-Fi communication technology are the foundation technology of the future smart electrical cars. Similar to aircraft, there advanced electrical cars will face the safety threats due EMI pollution. Current research out not only address the EMI pollution but also can act as a structural strain sensor for the composite components.

5.1.3 Wind Turbine

Wind turbine has been already introducing GFRP composites for their long blades. Due to its giant size, these structures are often experience lightning strikes. A sophisticated protection system is needed to protect electrical installations, the control electronics and the blades. Current research outcome can suppress the lightning damages of these structures but also can helps to monitor their deformation throughout the service.

5.2 Future Scope

The popularity of the composite structures is emerging in various industries from aerospace to automotive, wide turbine, civil, naval industries because of their superior properties. However, multifunctionality of these material value added to the structures. There still room to improve the material properties and other functionality as mention below.

- The mechanical properties of the current material are imitated compare to conventional epoxy base composite materials. Further study may require to improve its mechanical properties by upgrading the suitable polymer system.
- Initial study shows the opportunities of the material in other applications/functions, however need to be verify and characterize.
 - Vibration Sensor
 - Temperature sensor
- Further study needed to improve the bond between CFRP composites and PDD layer for LSP application.

Reference

- [1] Böger L, Wichmann MHG, Meyer LO, Schulte K. Load and health monitoring in glass fibre reinforced composites with an electrically conductive nanocomposite epoxy matrix. *Compos Sci Technol* 2008;68:1886–94. <https://doi.org/10.1016/j.compscitech.2008.01.001>.
- [2] Yang R, He Y, Zhang H. Progress and trends in nondestructive testing and evaluation for wind turbine composite blade. *Renew Sustain Energy Rev* 2016;60:1225–50. <https://doi.org/10.1016/j.rser.2016.02.026>.
- [3] Muflikhun MA, Yokozeki T, Aoki T. The strain performance of thin CFRP-SPCC hybrid laminates for automobile structures. *Compos Struct* 2019;220:11–8. <https://doi.org/10.1016/j.compstruct.2019.03.094>.
- [4] Goldston M, Remennikov A, Sheikh MN. Experimental investigation of the behaviour of concrete beams reinforced with GFRP bars under static and impact loading. *Eng Struct* 2016;113:220–32. <https://doi.org/10.1016/j.engstruct.2016.01.044>.
- [5] Hirano Y, Yokozeki T, Ishida Y, Goto T, Takahashi T, Qian D, et al. Lightning damage suppression in a carbon fiber-reinforced polymer with a polyaniline-based conductive thermoset matrix. *Compos Sci Technol* 2016;127:1–7. <https://doi.org/10.1016/j.compscitech.2016.02.022>.
- [6] Yang S, Lozano K, Lomeli A, Foltz HD, Jones R. Electromagnetic interference shielding effectiveness of carbon nanofiber/LCP composites. *Compos Part A Appl Sci Manuf* 2005;36:691–7. <https://doi.org/10.1016/j.compositesa.2004.07.009>.
- [7] Penris R; What Happens When Lightning Strikes An Airplane? Is It Safe? n.d. <https://blog.klm.com/what-happens-when-lightning-strikes-an-aircraft/> (accessed May 23, 2020).
- [8] AERO. Lightning Strikes: Protection, Inspection, and Repair. Boeing Co 2012. https://www.boeing.com/commercial/aeromagazine/articles/2012_q4/4/ (accessed May 22, 2020).
- [9] Wenk L, Bockenheimer C. Airbus technical magazine FAST 54. 2014.
- [10] Jones RM (Robert M. Mechanics of composite materials. Taylor & Francis; 1999.
- [11] Quilter A. Composites in Aerospace Applications. n.d.
- [12] Boeing 787 By Design: Advanced Composite Use. Boeing n.d. <https://www.boeing.com/commercial/787/by-design/#/advanced-composite-use>

- (accessed May 23, 2020).
- [13] Chung DDL. A review of multifunctional polymer-matrix structural composites. *Compos Part B Eng* 2019;160:644–60. <https://doi.org/10.1016/j.compositesb.2018.12.117>.
 - [14] Ates M, Karazehir T, Istanbul ASS. Conducting Polymers and their Applications. *Curr Physicst Chem* 2012;2:224–40. <https://doi.org/10.4028/www.scientific.net/MSF.42.207>.
 - [15] Li Y, Lu D, Wong CP, Li Y, Lu D, Wong CP. Intrinsically Conducting Polymers (ICPs). *Electr. Conduct. Adhes. with Nanotechnologies*, Springer US; 2010, p. 361–424. https://doi.org/10.1007/978-0-387-88783-8_8.
 - [16] Singh P, Shukla SK. Advances in polyaniline-based nanocomposites. *J Mater Sci* 2020;55:1331–65. <https://doi.org/10.1007/s10853-019-04141-z>.
 - [17] Le T-H, Kim Y, Yoon H. Electrical and Electrochemical Properties of Conducting Polymers. *Polymers (Basel)* 2017;9:150. <https://doi.org/10.3390/polym9040150>.
 - [18] Khalid M, Maria A, Honorato B. Polyaniline : Synthesis Methods , Doping and Conduction Mechanism. *Polyaniline - From Synth to Pract Appl* 2018.
 - [19] Han MG, Cho SK, Oh SG, Im SS. Preparation and characterization of polyaniline nanoparticles synthesized from DBSA micellar solution. *Synth Met* 2002;126:53–60. [https://doi.org/10.1016/S0379-6779\(01\)00494-5](https://doi.org/10.1016/S0379-6779(01)00494-5).
 - [20] Lakshmidevi V, Yelamaggad C V., Venkataraman A. Studies on Fluorescence Quenching of DBSA-PANI-Employing Nitroaromatics. *ChemistrySelect* 2018;3:2655–64. <https://doi.org/10.1002/slct.201702992>.
 - [21] Moreira VX, Garcia FG, Soares BG. Conductive epoxy/amine system containing polyaniline doped with dodecylbenzenesulfonic acid. *J Appl Polym Sci* 2006;100:4059–65. <https://doi.org/10.1002/app.23238>.
 - [22] Babazadeh M. Aqueous dispersions of DBSA-doped polyaniline: One-pot preparation, characterization, and properties study. *J Appl Polym Sci* 2009;113:3980–4. <https://doi.org/10.1002/app.30460>.
 - [23] Kumar V, Yokozeki T, Goto T, Takahashi T. Synthesis and Characterization of Conductive CFRP & GFRP Using Pani-Based Electrically Conductive Thermoset Polymer Matrix. 20th Int Conf Compos Mater Copenhagen, 19-24th July 2015 n.d.
 - [24] Kumar V, Yokozeki T, Goto T, Takahashi T. Scavenging phenomenon and improved electrical and mechanical properties of polyaniline – divinylbenzene composite in presence of MWCNT. *Int J Mech Mater Des* 2017. <https://doi.org/10.1007/s10999-017->

9397-y.

- [25] Kumar V, Yokozeki T, Goto T, Takahashi T, Dhakate SR, Singh BP. Irreversible tunability of through-thickness electrical conductivity of polyaniline-based CFRP by de-doping. *Compos Sci Technol* 2017;152:20–6. <https://doi.org/10.1016/j.compscitech.2017.09.005>.
- [26] Kumar V, Yokozeki T, Goto T, Takahashi T. Mechanical and electrical properties of PANI-based conductive thermosetting composites. *J Reinf Plast Compos* 2015;34:1298–305. <https://doi.org/10.1177/0731684415588551>.
- [27] Wang G, Wang Y, Zhang P, Zhai Y, Luo Y, Li L, et al. Structure dependent properties of carbon nanomaterials enabled fiber sensors for in situ monitoring of composites. *Compos Struct* 2018;195:36–44. <https://doi.org/10.1016/j.compstruct.2018.04.052>.
- [28] Lu S, Tian C, Wang X, Zhang L, Du K, Ma K, et al. Strain sensing behaviors of GnP/epoxy sensor and health monitoring for composite materials under monotonic tensile and cyclic deformation. *Compos Sci Technol* 2018;158:94–100. <https://doi.org/10.1016/j.compscitech.2018.02.017>.
- [29] Cao X, Wei X, Li G, Hu C, Dai K, Guo J. Strain sensing behaviors of epoxy nanocomposites with carbon nanotubes under cyclic deformation. *Polymer (Guildf)* 2017;112:1–9. <https://doi.org/10.1016/j.polymer.2017.01.068>.
- [30] Georgousis G, Pandis C, Kalamiotis A, Georgiopoulos P, Kyritsis A, Kontou E, et al. Composites : Part B Strain sensing in polymer / carbon nanotube composites by electrical resistance measurement. *Compos PART B* 2015;68:162–9. <https://doi.org/10.1016/j.compositesb.2014.08.027>.
- [31] Georgousis G, Roumpos K, Kontou E, Kyritsis A, Pissis P, Koutsoumpis S, et al. Strain and damage monitoring in SBR nanocomposites under cyclic loading cu. *Compos Part B Eng* 2017;131:50–61. <https://doi.org/10.1016/j.compositesb.2017.08.006>.
- [32] Wang X, Lu S, Ma K, Xiong X, Zhang H, Xu M. Tensile strain sensing of buckypaper and buckypaper composites 2015;88:414–9. <https://doi.org/10.1016/j.matdes.2015.09.035>.
- [33] Yazdani H, Hatami K, Grady BP, Khosravi E, Harper K, Grady BP. Strain-sensitive conductivity of carbon black-filled PVC composites subjected to cyclic loading. *Carbon N Y* 2014;79:393–405. <https://doi.org/10.1016/j.carbon.2014.07.082>.
- [34] Chiang CJ, Tsai KT, Lee YH, Lin HW, Yang YL, Shih CC, et al. In situ fabrication of conducting polymer composite film as a chemical resistive CO₂ gas sensor. *Microelectron Eng* 2013;111:409–15. <https://doi.org/10.1016/j.mee.2013.04.014>.

- [35] Liu C, Tai H, Zhang P, Yuan Z, Du X, Xie G. Sensors and Actuators B : Chemical A high-performance flexible gas sensor based on self-assembled PANI-CeO₂ nanocomposite thin film for trace-level NH₃ detection at room temperature. *Sensors Actuators B Chem* 2018;261:587–97. <https://doi.org/10.1016/j.snb.2017.12.022>.
- [36] Zhang C, Govindaraju S, Giribabu K, Suk Y, Yun K. Sensors and Actuators B : Chemical AgNWs-PANI nanocomposite based electrochemical sensor for detection of 4-nitrophenol. *Sensors Actuators B Chem* 2017;252:616–23. <https://doi.org/10.1016/j.snb.2017.06.039>.
- [37] Bora PJ, Mallik N, Ramamurthy PC, Kishore, Madras G. Poly(vinyl butyral) - polyaniline-magnetically functionalized fly ash cenosphere composite film for electromagnetic interference shielding. *Compos Part B Eng* 2016;106:224–33. <https://doi.org/10.1016/j.compositesb.2016.09.035>.
- [38] Gopakumar DA, Pai AR, Pottathara YB, Pasquini D, Carlos De Morais L, Luke M, et al. Cellulose Nanofiber-Based Polyaniline Flexible Papers as Sustainable Microwave Absorbers in the X-Band. *ACS Appl Mater Interfaces* 2018;10:20032–43. <https://doi.org/10.1021/acsami.8b04549>.
- [39] Zhang Y, Wang L, Zhang J, Song P, Xiao Z, Liang C, et al. Fabrication and investigation on the ultra-thin and flexible Ti₃C₂Tx/co-doped polyaniline electromagnetic interference shielding composite films. *Compos Sci Technol* 2019;183:107833. <https://doi.org/10.1016/j.compscitech.2019.107833>.
- [40] Pande S, Singh BP, Mathur RB, Dhami TL, Saini P, Dhawan SK. Improved electromagnetic interference shielding properties of MWCNT-PMMA composites using layered structures. *Nanoscale Res Lett* 2009;4:327–34. <https://doi.org/10.1007/s11671-008-9246-x>.
- [41] Chung DDL. Carbon materials for structural self-sensing, electromagnetic shielding and thermal interfacing. *Carbon N Y* 2012;50:3342–53. <https://doi.org/10.1016/j.carbon.2012.01.031>.
- [42] Hirano Y, Katsumata S, Iwahori Y, Todoroki A. Artificial lightning testing on graphite/epoxy composite laminate. *Compos Part A Appl Sci Manuf* 2010;41:1461–70. <https://doi.org/10.1016/j.compositesa.2010.06.008>.
- [43] Chakravarthi DK, Khabashesku VN, Vaidyanathan R, Blaine J, Yarlagadda S, Roseman D, et al. Carbon fiber-bismaleimide composites filled with nickel-coated single-walled carbon nanotubes for lightning-strike protection. *Adv Funct Mater* 2011;21:2527–33. <https://doi.org/10.1002/adfm.201002442>.

- [44] Gou J, Tang Y, Liang F, Zhao Z, Firsich D, Fielding J. Carbon nanofiber paper for lightning strike protection of composite materials. *Compos Part B Eng* 2010;41:192–8. <https://doi.org/10.1016/j.compositesb.2009.06.009>.
- [45] Raimondo M, Guadagno L, Speranza V, Bonnaud L, Dubois P, Lafdi K. Multifunctional graphene/POSS epoxy resin tailored for aircraft lightning strike protection. *Compos Part B Eng* 2018;140:44–56. <https://doi.org/10.1016/j.compositesb.2017.12.015>.
- [46] Rajesh PSM, Sirois F, Therriault D. Damage response of composites coated with conducting materials subjected to emulated lightning strikes. *Mater Des* 2018;139:45–55. <https://doi.org/10.1016/j.matdes.2017.10.017>.
- [47] Wang FS, Ji YY, Yu XS, Chen H, Yue ZF. Ablation damage assessment of aircraft carbon fiber/epoxy composite and its protection structures suffered from lightning strike. *Compos Struct* 2016;145:226–41. <https://doi.org/10.1016/j.compstruct.2016.03.005>.
- [48] Guo Y, Xu Y, Wang Q, Dong Q, Yi X, Jia Y. Eliminating lightning strike damage to carbon fiber composite structures in Zone 2 of aircraft by Ni-coated carbon fiber nonwoven veils. *Compos Sci Technol* 2019;169:95–102. <https://doi.org/10.1016/j.compscitech.2018.11.011>.
- [49] Kumar V, Yokozeki T, Okada T, Hirano Y, Goto T, Takahashi T, et al. Polyaniline-based all-polymeric adhesive layer: An effective lightning strike protection technology for high residual mechanical strength of CFRPs. *Compos Sci Technol* 2019;172:49–57. <https://doi.org/10.1016/j.compscitech.2019.01.006>.
- [50] Kumar V, Yokozeki T, Okada T, Hirano Y, Goto T, Takahashi T, et al. Effect of through-thickness electrical conductivity of CFRPs on lightning strike damages. *Compos Part A Appl Sci Manuf* 2018;114:429–38. <https://doi.org/10.1016/j.compositesa.2018.09.007>.
- [51] Katunin A, Krukiewicz K, Turczyn R, Sul P, Dragan K. Lightning strike resistance of an electrically conductive CFRP with a CSA-doped PANI/epoxy matrix. *Compos Struct* 2017;181:203–13. <https://doi.org/10.1016/j.compstruct.2017.08.091>.
- [52] Yokozeki T, Goto T, Takahashi T, Qian D, Itou S, Hirano Y, et al. Development and characterization of CFRP using a polyaniline-based conductive thermoset matrix. *Compos Sci Technol* 2015;117:277–81. <https://doi.org/10.1016/j.compscitech.2015.06.016>.
- [53] Vilatela JJ, Eder D. Nanocarbon Composites and Hybrids in Sustainability: A Review. *ChemSusChem* 2012;5:456–78. <https://doi.org/10.1002/cssc.201100536>.

- [54] SUMITA, M; SAKATA, K; ASAI, S; MIYASAKA KN. Dispersion of fillers and the electrical conductivity of polymer blends filled with carbon black. *Polym Bull* 1991;25:265–71. <https://doi.org/10.1017/S0165070X00001546>.
- [55] Sandler, JKW; Kirk, JE; Kinloch, IA; Shaffer, MSP; Windle A. Ultra-low electrical percolation threshold in carbon-nanotube-epoxy composites. *Polymer (Guildf)* 2003;44:5893–9. [https://doi.org/10.1016/S0032-3861\(03\)00539-1](https://doi.org/10.1016/S0032-3861(03)00539-1).
- [56] Kumar V, Yokozeki T, Goto T, Takahashi T. Synthesis and characterization of PANI-DBSA/DVB composite using roll-milled PANI-DBSA complex. *Polym (United Kingdom)* 2016;86:129–37. <https://doi.org/10.1016/j.polymer.2016.01.054>.
- [57] Cheng X, Yokozeki T, Wu L, Koyanagi J, Wang H, Sun Q. The enhancement effect of carbon-based nano-fillers/polyaniline hybrids on the through-thickness electric conductivity of carbon fiber reinforced polymer. *Compos Part A Appl Sci Manuf* 2018;105:281–90. <https://doi.org/10.1016/j.compositesa.2017.12.002>.
- [58] Cheng X, Yokozeki T, Yamamoto M, Wang H, Wu L, Koyanagi J, et al. The decoupling electrical and thermal conductivity of fullerene/polyaniline hybrids reinforced polymer composites. *Compos Sci Technol* 2017;144:160–8. <https://doi.org/10.1016/j.compscitech.2017.03.030>.
- [59] Liu L, Niu Z, Zhang L, Zhou W, Chen X, Xie S. Nanostructured graphene composite papers for highly flexible and foldable supercapacitors. *Adv Mater* 2014;26:4855–62. <https://doi.org/10.1002/adma.201401513>.
- [60] Tang W, Peng L, Yuan C, Wang J, Mo S, Zhao C, et al. Facile synthesis of 3D reduced graphene oxide and its polyaniline composite for super capacitor application. *Synth Met* 2015;202:140–6. <https://doi.org/10.1016/j.synthmet.2015.01.031>.
- [61] Devarayan K, Lei D, Kim HY, Kim BS. Flexible transparent electrode based on PANi nanowire/nylon nanofiber reinforced cellulose acetate thin film as supercapacitor. *Chem Eng J* 2015;273:603–9. <https://doi.org/10.1016/j.cej.2015.03.115>.
- [62] Roy A, Ray A, Saha S, Das S. Investigation on energy storage and conversion properties of multifunctional PANI-MWCNT composite. *Int J Hydrogen Energy* 2018;43:7128–39. <https://doi.org/10.1016/J.IJHYDENE.2018.02.153>.
- [63] Chang X, Hu R, Sun S, Liu J, Lei Y, Liu T, et al. Sunlight-charged electrochromic battery based on hybrid film of tungsten oxide and polyaniline. *Appl Surf Sci* 2018;441:105–12. <https://doi.org/10.1016/J.APSUSC.2018.02.003>.
- [64] Zhang X, Ma L, Gan M, Fu G, Jin M, Zhai Y. Controllable constructing of hollow MoS₂/PANI core/shell microsphere for energy storage. *Appl Surf Sci* 2017.

- <https://doi.org/10.1016/J.APSUSC.2017.10.010>.
- [65] Yeh J-M, Liou S-J, Lai C-Y, Wu P-C, Tsai T-Y. Enhancement of Corrosion Protection Effect in Polyaniline via the Formation of Polyaniline–Clay Nanocomposite Materials. *Chem Mater* 2001;13:1131–6. <https://doi.org/10.1021/cm000938r>.
 - [66] Li P, Tan TC, Lee JY. Corrosion protection of mild steel by electroactive polyaniline coatings. *Synth Met* 1997;88:237–42. [https://doi.org/10.1016/S0379-6779\(97\)03860-5](https://doi.org/10.1016/S0379-6779(97)03860-5).
 - [67] Bai H, Shi G. Gas sensors based on conducting polymers. *Sensors* 2007;7:267–307. <https://doi.org/10.3390/s7030267>.
 - [68] Virji S, Huang J, Kaner RB, Weiller BH. Polyaniline nanofiber gas sensors: Examination of response mechanisms. *Nano Lett* 2004;4:491–6. <https://doi.org/10.1021/nl035122e>.
 - [69] Gerard M, Chaubey A, Malhotra BD. Application of conducting polymers to biosensors. *Biosens Bioelectron* 2002;17:345–59. [https://doi.org/10.1016/S0956-5663\(01\)00312-8](https://doi.org/10.1016/S0956-5663(01)00312-8).
 - [70] Gong XX, Fei GT, Fu WB, Fang M, Gao XD, Zhong BN, et al. Flexible strain sensor with high performance based on PANI/PDMS films. *Org Electron Physics, Mater Appl* 2017;47:51–6. <https://doi.org/10.1016/j.orgel.2017.05.001>.
 - [71] Ranka P, Sethi V, Contractor AQ. One step electrodeposition of composite of PANI-PSS tubules with TiO₂nanoparticles and application as electronic sensor device. *Sensors Actuators, B Chem* 2018;261:11–21. <https://doi.org/10.1016/j.snb.2018.01.097>.
 - [72] Deshmukh MA, Patil HK, Bodkhe GA, Yasuzawa M, Koinkar P, Ramanaviciene A, et al. EDTA-modified PANI/SWNTs nanocomposite for differential pulse voltammetry based determination of Cu(II) ions. *Sensors Actuators B Chem* 2018;260:331–8. <https://doi.org/10.1016/J.SNB.2017.12.160>.
 - [73] Luan Y, Noh J-S, Kim SH. Facile control of stretchability and electrical resistance of elastomer/polyaniline composites for stretchable conductors. *Mater Chem Phys* 2017;190:68–73. <https://doi.org/10.1016/J.MATCHEMPHYS.2017.01.006>.
 - [74] Costa P, Oliveira J, Horta-romarís L, Abad M, Moreira JA, Zapiráin I, et al. Piezoresistive polymer blends for electromechanical sensor applications. *Compos Sci Technol* 2018;168:353–62. <https://doi.org/10.1016/j.compscitech.2018.10.022>.
 - [75] Teixeira J, Horta-Romarís L, Abad MJ, Costa P, Lanceros-Méndez S. Piezoresistive response of extruded polyaniline/(styrene-butadiene-styrene) polymer blends for force and deformation sensors. *Mater Des* 2018;141:1–8. <https://doi.org/10.1016/j.matdes.2017.12.011>.
 - [76] Horta-Romarís L, Abad MJ, González-Rodríguez MV, Lasagabáster A, Costa P,

- Lanceros-Méndez S. Cyclic temperature dependence of electrical conductivity in polyanilines as a function of the dopant and synthesis method. *Mater Des* 2017;114:288–96. <https://doi.org/10.1016/j.matdes.2016.11.021>.
- [77] Mattmann C, Clemens F, Tröster G. Sensor for measuring strain in textile. *Sensors* 2008;8:3719–32. <https://doi.org/10.3390/s8063719>.
- [78] Kumar V, Das S, Yokozeki T. Frequency independent AC electrical conductivity and dielectric properties of polyaniline-based conductive thermosetting composite. *J Polym Eng* 2018;38:955–61. <https://doi.org/10.1515/polyeng-2018-0031>.
- [79] Gonçalves BF, Costa P, Oliveira J, Ribeiro S, Correia V, Botelho G, et al. Green solvent approach for printable large deformation thermoplastic elastomer based piezoresistive sensors and their suitability for biomedical applications. *J Polym Sci Part B Polym Phys* 2016;54:2092–103. <https://doi.org/10.1002/polb.24118>.
- [80] Alamusi, Hu N, Fukunaga H, Atobe S, Liu Y, Li J. Piezoresistive strain sensors made from carbon nanotubes based polymer nanocomposites. *Sensors* 2011;11:10691–723. <https://doi.org/10.3390/s111110691>.
- [81] Gao S, Zhuang R, Zhang J, Liu J, Ma E. Glass Fibers with Carbon Nanotube Networks as Multifunctional Sensors 2010:1885–93. <https://doi.org/10.1002/adfm.201000283>.
- [82] Das S, Kumar V, Yokozeki T. Strain sensing behavior of multifunctional polyaniline-based thermoset polymer under static loading conditions. *Polym Test* 2019;77:105916. <https://doi.org/10.1016/j.polymertesting.2019.105916>.
- [83] Lisle T, Bouvet C, Pastor ML, Rouault T, Marguerès P. Damage of woven composite under tensile and shear stress using infrared thermography and micrographic cuts. *J Mater Sci* 2015;50:6154–70. <https://doi.org/10.1007/s10853-015-9173-z>.
- [84] Bhadra S, Singha NK, Khastgir D. Dielectric properties and EMI shielding efficiency of polyaniline and ethylene 1-octene based semi-conducting composites. *Curr Appl Phys* 2009;9:396–403. <https://doi.org/10.1016/j.cap.2008.03.009>.
- [85] Kumar V, Muflikhun MA, Yokozeki T. Improved environmental stability, electrical and EMI shielding properties of vapor-grown carbon fiber-filled polyaniline-based nanocomposite. *Polym Eng Sci* 2018. <https://doi.org/10.1002/pen.25045>.
- [86] Khalid HR, Nam IW, Choudhry I, Zheng L, Lee HK. Piezoresistive characteristics of CNT fiber-incorporated GFRP composites prepared with diversified fabrication schemes. *Compos Struct* 2018;203:835–43. <https://doi.org/10.1016/j.compstruct.2018.08.003>.
- [87] Li W, He D, Dang Z, Bai J. In situ damage sensing in the glass fabric reinforced epoxy

- composites containing CNT-Al₂O₃ hybrids. *Compos Sci Technol* 2014;99:8–14. <https://doi.org/10.1016/j.compscitech.2014.05.005>.
- [88] Wang YYY, Wang YYY, Wan B, Han B, Cai G, Chang R. Strain and damage self-sensing of basalt fiber reinforced polymer laminates fabricated with carbon nanofibers/epoxy composites under tension. *Compos Part A Appl Sci Manuf* 2018;113:40–52. <https://doi.org/10.1016/j.compositesa.2018.07.017>.
- [89] Pedrazzoli D, Dorigato A, Pegoretti A. Monitoring the mechanical behavior under ramp and creep conditions of electrically conductive polymer composites. *Compos Part A Appl Sci Manuf* 2012;43:1285–92. <https://doi.org/10.1016/j.compositesa.2012.03.019>.
- [90] Matsuda T, Nakata K, Kawai M. Homogenization creep analysis of plain-woven GFRP laminates. *ICCM Int Conf Compos Mater* 2009.
- [91] Mulliken AD, Boyce MC. Mechanics of the rate-dependent elastic-plastic deformation of glassy polymers from low to high strain rates. *Int J Solids Struct* 2006;43:1331–56. <https://doi.org/10.1016/j.ijsolstr.2005.04.016>.
- [92] Zheng Q, Zhou JF, Song YH. Time-dependent uniaxial piezoresistive behavior of high-density polyethylene/short carbon fiber conductive composites. *J Mater Res* 2004;19:2625–34. <https://doi.org/10.1557/JMR.2004.0355>.
- [93] Jeon J, Muliana A, La Saponara V. Thermal stress and deformation analyses in fiber reinforced polymer composites undergoing heat conduction and mechanical loading. *Compos Struct* 2014;111:31–44. <https://doi.org/10.1016/j.compstruct.2013.11.027>.
- [94] Takahashi K, Hahn HT. Investigation of temperature dependency of electrical resistance changes for structural management of graphite/polymer composite. 25th Tech Conf Am Soc Compos 14th US-Japan Conf Compos Mater 2010 2010;1:185–97. <https://doi.org/10.1177/0021998311416683>.
- [95] Wang Y, Wang Y, Han B, Wan B, Cai G, Chang R. In situ strain and damage monitoring of GFRP laminates incorporating carbon nanofibers under tension. *Polymers (Basel)* 2018;10. <https://doi.org/10.3390/polym10070777>.
- [96] Klemperer CJ vo., Maharaj D. Composite electromagnetic interference shielding materials for aerospace applications. *Compos Struct* 2009;91:467–72. <https://doi.org/10.1016/j.compstruct.2009.04.013>.
- [97] Klemperer CJ vo., Maharaj D. Composite electromagnetic interference shielding materials for aerospace applications. *Compos Struct* 2009;91:467–72. <https://doi.org/10.1016/j.compstruct.2009.04.013>.
- [98] Choudhary HK, Kumar R, Pawar SP, Sundararaj U, Sahoo B. Effect of morphology and

- role of conductivity of embedded metallic nanoparticles on electromagnetic interference shielding of PVDF-carbonaceous-nanofiller composites. *Carbon N Y* 2020;164:357–68. <https://doi.org/10.1016/j.carbon.2020.04.007>.
- [99] Shahzad F, Alhabeb M, Hatter CB, Anasori B, Hong SM, Koo CM, et al. Electromagnetic interference shielding with 2D transition metal carbides (MXenes). *Science* (80-) 2016;353:1137–40. <https://doi.org/10.1126/science.aag2421>.
- [100] Coleman JN, Khan U, Gun'ko YK. Mechanical Reinforcement of Polymers Using Carbon Nanotubes. *Adv Mater* 2006;18:689–706. <https://doi.org/10.1002/adma.200501851>.
- [101] Anju VP, Manoj M, Mohanan P, Narayanankutty SK. A comparative study on electromagnetic interference shielding effectiveness of carbon nanofiber and nanofibrillated cellulose composites. *Synth Met* 2019;247:285–97. <https://doi.org/10.1016/j.synthmet.2018.12.021>.
- [102] Huangfu Y, Ruan K, Qiu H, Lu Y, Liang C, Kong J, et al. Fabrication and investigation on the PANI/MWCNT/thermally annealed graphene aerogel/epoxy electromagnetic interference shielding nanocomposites. *Compos Part A Appl Sci Manuf* 2019;121:265–72. <https://doi.org/10.1016/j.compositesa.2019.03.041>.
- [103] Movassagh-Alanagh F, Bordbar-Khiabani A, Ahangari-Asl A. Three-phase PANI@nano-Fe₃O₄@CFs heterostructure: Fabrication, characterization and investigation of microwave absorption and EMI shielding of PANI@nano-Fe₃O₄@CFs/epoxy hybrid composite. *Compos Sci Technol* 2017;150:65–78. <https://doi.org/10.1016/j.compscitech.2017.07.010>.
- [104] Al-Saleh MH, Sundararaj U. Electromagnetic interference shielding mechanisms of CNT/polymer composites. *Carbon N Y* 2009;47:1738–46. <https://doi.org/10.1016/j.carbon.2009.02.030>.
- [105] Kondawar SB, Modak PR. Theory of EMI shielding. Elsevier Inc.; 2020. <https://doi.org/10.1016/B978-0-12-817590-3.00002-6>.
- [106] Ghione G, Pirola M. Microwave electronics. 2017. <https://doi.org/10.1017/9781316756171>.
- [107] Paul, Clayton R. Introduction to Electromagnetic Compatibility {Wiley Series in Microwave and Optical Engineering; 2nd Ed.}. 2006.
- [108] Colaneri NF, Shacklette LW. EMI Shielding Measurements of Conductive Polymer Blends. *IEEE Trans Instrum Meas* 1992;41:291–7. <https://doi.org/10.1109/19.137363>.
- [109] Schulz RB, Plantz VC, Brush DR. Shielding Theory and Practice. *IEEE Trans*

- Electromagn Compat 1988;30:187–201. <https://doi.org/10.1109/15.3297>.
- [110] Neelakanta PS. Handbook of Electromagnetic Materials: Monolithic and Composite Versions and Their Applications. 1995.
- [111] Gupta TK, Singh BP, Mathur RB, Dhakate SR. Multi-walled carbon nanotube-graphene-polyaniline multiphase nanocomposite with superior electromagnetic shielding effectiveness. *Nanoscale* 2014;6:842–51. <https://doi.org/10.1039/c3nr04565j>.
- [112] Nicolson AM, Ross GF. Measurement of the Intrinsic Properties Of Materials by Time-Domain Techniques. *IEEE Trans Instrum Meas* 1970;19:377–82. <https://doi.org/10.1109/TIM.1970.4313932>.
- [113] Weir WB. Automatic Measurement of Complex Dielectric Constant and Permeability at Microwave Frequencies. *Proc IEEE* 1974;62:33–6. <https://doi.org/10.1109/PROC.1974.9382>.
- [114] Bora PJ, Vinoy KJ, Ramamurthy PC, Madras G. Electromagnetic interference shielding efficiency of MnO₂ nanorod doped polyaniline film. *Mater Res Express* 2017;4. <https://doi.org/10.1088/2053-1591/aa59e3>.
- [115] Wang H, Ma N, Yan Z, Deng L, He J, Hou Y, et al. Cobalt/polypyrrole nanocomposites with controllable electromagnetic properties. *Nanoscale* 2015;7:7189–96. <https://doi.org/10.1039/c4nr06978a>.
- [116] Ji K, Zhao H, Zhang J, Chen J, Dai Z. Fabrication and electromagnetic interference shielding performance of open-cell foam of a Cu-Ni alloy integrated with CNTs. *Appl Surf Sci* 2014;311:351–6. <https://doi.org/10.1016/j.apsusc.2014.05.067>.
- [117] Lakshmi K, John H, Mathew KT, Joseph R, George KE. Microwave absorption, reflection and EMI shielding of PU-PANI composite. *Acta Mater* 2009;57:371–5. <https://doi.org/10.1016/j.actamat.2008.09.018>.
- [118] Shen B, Zhai W, Tao M, Ling J, Zheng W. Lightweight, multifunctional polyetherimide/graphene@Fe₃O₄ composite foams for shielding of electromagnetic pollution. *ACS Appl Mater Interfaces* 2013;5:11383–91. <https://doi.org/10.1021/am4036527>.
- [119] Yang Y, Gupta MC, Dudley KL, Lawrence RW. Novel carbon nanotube - Polystyrene foam composites for electromagnetic interference shielding. *Nano Lett* 2005;5:2131–4. <https://doi.org/10.1021/nl051375r>.
- [120] Grimes CA, Grimes DM. A brief discussion of EMI shielding materials. 1993 IEEE Aerosp. Appl. Conf. Dig. AERO 1993, Institute of Electrical and Electronics Engineers Inc.; 1993, p. 217–26. <https://doi.org/10.1109/AERO.1993.255321>.

- [121] Rothwell EJ, Frasca JL, Ellison SM, Chahal P, Ouedraogo RO. Analysis of the Nicolson-Ross-Weir method for characterizing the electromagnetic properties of engineered materials. *Prog Electromagn Res* 2016;157:31–47. <https://doi.org/10.2528/PIER16071706>.
- [122] Saini P. *Fundamentals of Conjugated Polymer Blends, Copolymers and Composites*. Canada: Scrivener Publishing LLC; 2015.
- [123] Saini P, Choudhary V, Vijayan N, Kotnala RK. Improved electromagnetic interference shielding response of poly(aniline)-coated fabrics containing dielectric and magnetic nanoparticles. *J Phys Chem C* 2012;116:13403–12. <https://doi.org/10.1021/jp302131w>.
- [124] Jonscher AK. The “universal” dielectric response. *Nature* 1977;267:673–9. <https://doi.org/10.1038/267673a0>.
- [125] Kumar V, Yokozeki T, Karch C, Hassen AA, Hershey CJ, Kim S, et al. Factors affecting direct lightning strike damage to fiber reinforced composites: A review. *Compos Part B Eng* 2020;183:107688. <https://doi.org/10.1016/j.compositesb.2019.107688>.
- [126] Gagné M, Therriault D. Lightning strike protection of composites. *Prog Aerosp Sci* 2014;64:1–16. <https://doi.org/10.1016/j.paerosci.2013.07.002>.
- [127] Kamiyama S, Hirano Y, Okada T, Sawaki K, Sonehara T, Ogasawara T. Damage behavior of CFRP subjected to simulated lightning current under air, reduced-pressure air, and N₂ environments. *Compos Struct* 2019;230:111519. <https://doi.org/10.1016/j.compstruct.2019.111519>.
- [128] Hirano Y, Yokozeki T, Goto T, Takahashi T, Qian D. Pani-Based Conductive Thermosetting Composite 2015:19–24.
- [129] HIRANO Y, YOKOZEKI T, GOTO T, TAKAHASHI T, QIAN D, ITO S, et al. Effectiveness of Lightning Damage Protection of CFRP with Polyaniline-Based Conductive Thermoset Matrix. *J Japan Soc Aeronaut Sp Sci JAPAN Soc Aeronaut Sp Sci* 2016;64:223–8. <https://doi.org/10.2322/jjsass.64.223>.
- [130] Larsson A, Lalande P, Bondiou-Clergerie A, Delannoy A. The lightning swept stroke along an aircraft in flight. Part I: Thermodynamic and electric properties of lightning arc channels. *J Phys D Appl Phys* 2000;33:1866–75. <https://doi.org/10.1088/0022-3727/33/15/317>.
- [131] Han JH, Zhang H, Chen MJ, Wang D, Liu Q, Wu QL, et al. The combination of carbon nanotube buckypaper and insulating adhesive for lightning strike protection of the carbon fiber/epoxy laminates. *Carbon N Y* 2015;94:101–13. <https://doi.org/10.1016/j.carbon.2015.06.026>.

Appendix A: MATLAB Code for NRW algorithm

```
% NOTE1: Make sure the VNA out file (S parameters with frequency) in the
% following order. [f(Hz) s11r s11i s21r s21i s21r s21i s22r s22i]
% NOTE2: load the VNA file as a variable and keep the same name as line 9
% in the code
% NOTE3: Change the frq unit, this code is made for GHz
%% Conversation
%% Parameters
clc
VNA_data=inputfile; % File name of the VNA data S-parameter file [f s11r s11i s21r s21i
s21r s21i s22r s22i]
t=input('thickness of the shielding material in cm: --> '); % Thickness of the Shielding material
in cm
S11=VNA_data(:,2)+1i*VNA_data(:,3); % Reform S11 in the complex form
S21=VNA_data(:,4)+1i*VNA_data(:,5); % Reform S21 in the complex form
S12=VNA_data(:,6)+1i*VNA_data(:,7); % Reform S12 in the complex form
S22=VNA_data(:,8)+1i*VNA_data(:,9); % Reform S22 in the complex form
frq=VNA_data(:,1); % Extract the frequency data
f=frq./10^9; % X-band frequency in GHz
fc=input('Cutoff frequency in GHz:--> '); % The cutoff_freq in GHz use to calculate wavelength
lamda_0
lamda_0=29.9792458./f; % Wave lengths in cm
lamda_c=29.9792458./fc; % Cutoff Wave lengths in cm
n=fix(t.*sqrt((1./lamda_0.^2)-(1./lamda_c.^2))); % 'n' used to choose correct root of
complex log term
%% NRW Conversations
clc
```

```

K=((S22).^2)-((S12).^2)+1)/(2.*S22); % Step1 : Calculate the roots of the reflection
coefficient
GAMA1=K+sqrt(((K.^2)-1)); % Step2 : Calculate the reflection coefficients with possible
roots
GAMA2=K-sqrt(((K.^2)-1));
%% Checking 1 : |GAMA| < 1
mode_GAMA1=abs(GAMA1); % check |GAMA| <1, to select the correct root
mode_GAMA2=abs(GAMA2);
gama_final=ones(length(GAMA1),1);

for i = 1:length(mode_GAMA1)
    if mode_GAMA1(i,1)<1
        gama_final(i,1) = GAMA1(i,1);
    else
        gama_final(i,1) = GAMA2(i,1);
    end
end
clc
disp(round(abs(gama_final),2))

%% NRW Converstions
clc
T=(S22+S12-gama_final)/(1-((S22+S12).*gama_final)); %Step3 : Calcualte the
transmission coefficient
log_inv=log(abs(1./T))+1i.*(((angle(1./T)+(2.*pi.*n))));
first_term_permeability1_sqr=((1./(2.*pi.*t)).*log_inv).^2;
first_term_permeability=sqrt(-1.*first_term_permeability1_sqr);
%% NRW Converstions
clc
Second_term_permeability=(1+gama_final)/(1-gama_final);
permeabillity=(first_term_permeability.*Second_term_permeability)/(sqrt((1./lamda_0.^2)-
(1./lamda_c.^2)));
permittivity=((first_term_permeability1_sqr+(1./(lamda_c).^2)).*lamda_0.^2)/(permeabilli
ty);

```

```

%% UPdate the file name
mu_cfrp8l08mm12=permeability(1:end,1);           % change the variable
name and replace for all
epsilon_cfrp8l08mm12=permittivity(1:end,1);       % change the variable
name and replace for all
f=f(1:end);
%% Del points if needed
% f(31)=[];
% mu_GFRP8LPDD05(31)=[];
% epsilon_GFRP8LPDD05(31)=[];
%% Update the Legend name
clc; % Clear the command window.
workspace; % Make sure the workspace panel is showing.
format longg;
format compact;
fontSize = 20;
% Create axes
axes1 = axes('Parent',figure('DefaultAxesFontSize',20));
set(axes1,'FontSize',20);
subplot(2,2,1)
plot(f,real(mu_cfrp8l08mm12(1:end-1)),'LineWidth',2)
hold on
% ylim([0 60])
% plot(f,real(mu_PDD08mm),'LineWidth',2)
% % hold on
% plot(f,real(mu_PDD06mm),'LineWidth',2)
% plot(f,real(mu_PDD05mm),'LineWidth',2)

xlabel('Frequency (GHz)', 'FontSize', fontSize)
ylabel('\mu"', 'FontSize', fontSize)
legend('PDD layer 1mm (0.97S/cm)','PDD layer 0.8mm (0.73S/cm)','PDD layer 0.6mm (0.71S/cm)', 'PDD layer 0.5mm (0.75S/cm)', 'Location', 'southeast')
% legend('PDD layer 0.6mm (0.71S/cm)', 'PDD layer 0.5mm (0.75S/cm)', 'Location', 'southeast')

```

```

legend('GFRP8LPDD layer 1mm (0.82S/cm)','PDD layer 0.8mm (0.73S/cm)','PDD layer
0.6mm (0.71S/cm)','PDD layer 0.5mm (0.75S/cm)','Location','southeast')
% legend('PDD layer 1mm (0.97S/cm)','PDD layer 0.8mm (0.73S/cm)','PDD layer 0.6mm
(0.71S/cm)','PDD layer 0.5mm (0.75S/cm)','Location','southeast')

subplot(2,2,2)
plot(f,imag(mu_cfrp8l08mm12(1:end-1)),'LineWidth',2)
hold on
% ylim([0 60])
% plot(f,imag(mu_PDD08mm),'LineWidth',2)
% plot(f,imag(mu_PDD06mm),'LineWidth',2)
% plot(f,imag(mu_PDD05mm),'LineWidth',2)
xlabel('Frequency (GHz)', 'FontSize', fontSize)
ylabel('\mu" ', 'FontSize', fontSize)
% legend('PDD layer 1mm (0.97S/cm)','PDD layer 0.8mm (0.73S/cm)','PDD layer 0.6mm
(0.71S/cm)','PDD layer 0.5mm (0.75S/cm)','Location','southeast')
legend('GFRP8LPDD layer 1mm (0.82S/cm)','PDD layer 0.8mm (0.73S/cm)','PDD layer
0.6mm (0.71S/cm)','PDD layer 0.5mm (0.75S/cm)','Location','southeast')
% legend('PDD layer 1mm (0.97S/cm)','PDD layer 0.8mm (0.73S/cm)','PDD layer 0.6mm
(0.71S/cm)','PDD layer 0.5mm (0.75S/cm)','Location','southeast')

subplot(2,2,3)
plot(f,real(epsilon_cfrp8l08mm12(1:end-1)),'LineWidth',2)
hold on
% ylim([0 30])
% plot(f,real(epsilon_PDD08mm),'LineWidth',2)
% plot(f,real(epsilon_PDD06mm),'LineWidth',2)
% plot(f,real(epsilon_PDD05mm),'LineWidth',2)

xlabel('Frequency (GHz)', 'FontSize', fontSize)
ylabel('\epsilon"', 'FontSize', fontSize)
legend('GFRP10L','GFRP8L','GFRP4L','GFRP8LPDD05','Location','southeast')
% legend('PDD layer 1mm (0.97S/cm)','PDD layer 0.8mm (0.73S/cm)','PDD layer 0.6mm
(0.71S/cm)','PDD layer 0.5mm (0.75S/cm)','Location','southeast')

```

```

% legend('PDD layer 0.6mm (0.71S/cm)','PDD layer 0.5mm (0.75S/cm)','Location','southeast')
% legend('GFRP8LPDD layer 1mm (0.82S/cm)','PDD layer 0.8mm (0.73S/cm)','PDD layer
0.6mm (0.71S/cm)','PDD layer 0.5mm (0.75S/cm)','Location','southeast')
% legend('PDD layer 1mm (0.97S/cm)','PDD layer 0.8mm (0.73S/cm)','PDD layer 0.6mm
(0.71S/cm)','PDD layer 0.5mm (0.75S/cm)','Location','southeast')
subplot(2,2,4)
plot(f,imag(epsilon_cfrp8l08mm12(1:end-1)),'LineWidth',2)
hold on
% ylim([0 30])
% plot(f,imag(epsilon_PDD08mm),'LineWidth',2)
% plot(f,imag(epsilon_PDD06mm),'LineWidth',2)
% plot(f,imag(epsilon_PDD05mm),'LineWidth',2)
xlabel('Frequency (GHz)', 'FontSize', fontSize)
ylabel('\epsilon'' , 'FontSize', fontSize)
% legend('PDD layer 1mm (0.97S/cm)','PDD layer 0.8mm (0.73S/cm)','PDD layer 0.6mm
(0.71S/cm)','PDD layer 0.5mm (0.75S/cm)','Location','southeast')
legend('CFRP8LPDD layer 1mm (0.82S/cm)','PDD layer 0.8mm (0.73S/cm)','PDD layer
0.6mm (0.71S/cm)','PDD layer 0.5mm (0.75S/cm)','Location','southeast')
hold on
% % Enlarge figure to full screen.
font_size=12; % Technical paper writting font size
f_width=8.5; %the figure width (in inches)
f_hight=6.5; %the figure hight (in inches)
font_rate=10/font_size;
set(gcf, 'Position',[100 100 round(f_width*font_rate*144) round(f_hight*font_rate*144)])
set(gca, 'fontsize', 20)
clc
%% Update the file name
saveas(gcf,'/Users/sukantadas/Google Drive /MATLAB/MATLAB-UoT/Paper-III/PDD
Thickness/CFRPPDD1mmDielectricPDD1mmp2-Finalpaper.tif');
savefig(gcf,'/Users/sukantadas/Google Drive /MATLAB/MATLAB-UoT/Paper-III/PDD
Thickness/CFRPPDD1mmDielectricPDD1mmp2-Finalpaper.fig');

```